Interaction of intense VUV radiation

from a Free-Electron Laser

with rare gas atoms and clusters

DISSERTATION
zur Erlangung des Doktorgrades
des Fachbereichs Physik
der Universität Hamburg

vorgelegt von
Hubertus Wabnitz
aus Widdern

Hamburg
2003

Abstract:

At DESY, the short wavelength free-electron laser of the TESLA Test Facility (TTF1-FEL) showed in September 2001 the production of vacuum-ultraviolet radiation, whose peak power exceeded that of existing light-sources by a factor of more than thousand. Thus it opened the way to studies of matter with intense, short wavelength radiation. First experiments on the interaction of intense, short wavelength radiation with rare gas atom and cluster beams have been conducted. Atomic and cluster beams are produced by a supersonic nozzle expansion. The ionisation products are detected by time-of-flight techniques. At 98 nm wavelength the ionisation of rare gas atoms is attributed to a stepwise multiphoton ionisation. Compared to the atomic beam the absorption in the cluster beam is strongly enhanced. At a power density of $\sim 3 \times 10^{13}\,\mathrm{W/cm^2}$ each atom in a Xe_{2500} cluster absorbs on average $\sim 600\,\mathrm{eV}$, corresponding to ~ 50 VUV photons. As a result of the strong absorption multiply charged atomic ions up to Xe^{8+} are produced. Finally, the cluster completely disintegrates by Coulomb explosion, causing high kinetic energies of the ejected ions up to $3\,\mathrm{keV}$. Coulomb explosion begins at a power density approximately two orders of magnitude lower than the threshold for such processes in optical laser experiments. A comparison is made with classical models describing quantitatively the energy absorption at optical wavelengths. It appears that quantum mechanical processes have to be included, in order to explain the energy absorption in the present FEL experiment at short wavelengths.

Kurzfassung:

Im September 2001 wurde bei DESY der Freie-Elektronen-Laser (FEL) für kurzwellige Strahlung an der TESLA Test-Facility (TTF1) in Betrieb genommen. Im Bereich der vakuum-ultravioletten (VUV) Strahlung überstieg die Pulsleistung des FEL diejenige bestehender Lichtquellen um mehr als das tausendfache. Damit wurde es erstmals möglich die Wechselwirkung von intensiver, kurzwelliger Strahlung mit Materie zu untersuchen. Die ersten Experimente wurden an Atom- und Clusterstrahlen durchgeführt. Atom- und Clusterstrahlen der Edelgase werden mithilfe einer Düsenstrahlexpansion erzeugt. Zum Nachweis der Ionisationsprodukte wurden Flugzeitdetektoren eingesetzt. Bei einer Wellenlänge von 98 nm kann die Ionisierung der Edelgasatome als "stufenweise" Multiphotonen-Ionisation interpretiert werden. Verglichen mit einem Atomstrahl ist die Absorption im Clusterstrahl weitaus stärker. Bei einer Leistungsdichte von $\sim 3 \times 10^{13}\,\mathrm{W/cm^2}$ absorbiert jedes Atom in einem Xe_{2500} Cluster durchschnittlich $\sim 600\,\mathrm{eV}$. Das entspricht einer Absorption von etwa 50 VUV-Photonen. Als Resultat der starken Absorption werden bis zu achtfach geladene atomare Xenonionen nachgewiesen. Die Cluster werden durch eine Coulombexplosion zerstört und emittieren hochenergetische Ionen mit bis zu 3 keV kinetischer Energie. Im Gegensatz zu Experimenten mit optischen Lasern beginnt die Coulombexplosion bereits bei sehr viel niedrigeren, ungefähr zwei Größenordnungen geringeren Leistungsdichten. Ein Vergleich mit klassischen Modellen, die die Absorption bei optischen Wellenlängen quantitativ beschreiben, zeigt, dass wahrscheinlich quantenmechanische Prozesse berücksichtigt werden müssen, um die hohe Absorption im FEL-Experiment bei kurzen Wellenlängen zu erklären.

Contents

Chapter 1

Introduction

In 1931 Marion Göppert-Mayer predicted an optical non-linear process in which an atom absorbs two photons [1]. 30 years later the development of the laser made it possible to observe the so called two-photon absorption experimentally in 1961 [2, 3]. Since then the improvement of lasers has made it possible to study the nonlinear interaction of ever more intense radiation with matter. However, these studies have been limited to the infrared and optical range. At wavelengths in the vacuum ultraviolet (VUV) and soft X-ray regime, where the photon energy becomes large enough to ionise matter, hardly any light-sources capable of producing intense radiation have been available up to now. For quite a time accelerator based devices, called free-electron lasers (FELs), have been expected to overcome the barrier and produce intense short wavelength radiation, eventually down to the hard X-ray regime. In FELs, highly collimated, coherent radiation is produced by passing a relativistic electron beam through a periodic magnetic field. In September 2001 the FEL at the Tesla Test Facility (TTF) at DESY showed production of gigawatt radiation with 50 fs pulse duration in the VUV region from 80-120 nm and therefore opened the way to studies of matter with intense, short wavelength radiation. The peak power of this new light-source exceeded that of existing light-sources by more than a factor of 1000.

The potential impact of short wavelength FELs is tremendous. Ionising radiation such as VUV, soft and hard X-ray light gives insight into the electronic and geometric structure and chemical composition of matter. Excitation with soft X-rays allows for the determination of the chemical composition because the individual elements have characteristic binding energies. The diffraction of hard X-rays, which have a wavelength comparable to the separation of atoms in a solid, allows structure determination of complex systems with atomic resolution. Femtosecond X-ray pulses, for example, make it possible to take 'snapshot' pictures of single biomolecules in a single shot, provided the beam is sufficiently intense and short. The method relies on being able to record a diffraction pattern before radiation damage takes place. Up to now, crystallography techniques make it inevitable to crystallise biomolecules, which puts severe limitations

and is often impossible. With the new techniques using short pulse FELs it might be possible to determine the structure without crystallisation. In this context, a first experiment at the TTF-FEL will also serve as a test experiment for all future investigations.

In the present experiment, the interaction of intense VUV radiation with rare gas atoms and clusters is investigated. The main scientific interest is the study of light-cluster interaction. Clusters are systems made of a few (>2) up to many ($\sim 10^6$) atoms and bridge the gap between the molecular and the bulk solid state of matter. Rare gas clusters form the most simple clusters and can be regarded as model substances for condensed matter.

When a cluster is exposed to intense infrared laser radiation a large amount of energy is absorbed by the cluster. This transfer of energy from the laser field results in the ionisation of the cluster and the creation of a nanoplasma. Eventually this plasma expands very rapidly or in other words, it explodes. Although there are many questions yet to be answered, the physics of the mechanisms leading to the high energy absorption are quite well understood. A main task of this work is to investigate if the well-understood physics in the infrared radiation regime can also describe the interaction of short wavelength VUV radiation with clusters.

There are two substantial differences between VUV and infrared radiation which can be expected to affect the interaction with matter. First, the electrons react more sluggish to the higher-frequency VUV radiation. Second, in the infrared region the energy of single photons is considerably smaller than the ionisation potential of rare gases. On the other hand, in the VUV region the photon energy exceeds the ionisation potential of many materials and ionisation is possible by direct photon absorption.

This work is organised in the following way: In chapter 2 the experimental aspects including the VUV-FEL, the experimental set-up and the data acquisition are presented. Chapter 3 is dedicated to the experimental results after irradiation of rare gas atoms and xenon clusters with intense VUV radiation. Finally, the results of this work are summarised in chapter 4 and a brief outlook is given.

Chapter 2

Experimental aspects

2.1 Free-electron lasers for short wavelength radiation

2.1.1 Introduction

Since three decades synchrotron radiation is the most powerful source for producing short wavelength radiation such as X-rays. Scientific applications include various fields such as physics, chemistry, biology and material science. Today synchrotron radiation is routinely produced by storage ring based devices, in which relativistic electron bunches pass periodic arrays of magnets (undulators and wigglers). As a result, the electrons are accelerated by the Lorentz force of the magnetic field and they emit spontaneous radiation. The spontaneous radiation they emit is not coherent and the radiation power P is proportional to N_e, $P \propto N_e$, where N_e is the number of electrons. The key idea of the free-electron laser (FEL) is now, to force the electrons to emit coherently, which results in $P \propto N_e^2$. This can give an enormous increase in radiation power, because the number of electrons is about $N_e \sim 10^8$. Coherent emission can be realized by compressing the electron bunch to a size, which is small (i.e. 'point-like') compared to the emitted wavelength. But this is not achievable for radiation wavelengths in the nanometer regime, when the bunch contains such a large number of electrons like mentioned above. Alternatively, a large number of 'point-like' bunch-lets arranged longitudinally in a periodic array also emits coherently, provided the periodicity is given by the wavelength of the radiation.

It follows from the resonance condition of an undulator (see equation (2.1)) that the emitted wavelength λ_r can be varied continuously because $\lambda_r \propto 1/E^2$, where E is the electron energy. The tunability of the wavelength or photon energy is one main advantage of the FEL. The use of very energetic electrons up to 10 GeV or more enables the production of extremely short wavelengths.

Existing FELs can be distinguished in devices, in which the amplification of the radia-

tion is reached during several passes (low gain FEL) of the electron bunch through the undulator or just in one pass (high gain FEL). In a low gain FEL the radiation emitted by the electrons in the undulator is stored in an optical cavity and each time the electron bunch passes the undulator/cavity the radiation is amplified. In a single pass free-electron laser 'amplifier' the radiation to be amplified maybe classified into two distinct types: 1) Radiation from an external coherent source such as a laser. 2) The spontaneous emission produced in the first part of the undulator. The latter describes an FEL working after the Self-Amplified-Spontaneous-Emission (SASE) principle.

In a SASE-FEL the interaction of the spontaneous radiation with the transverse component of the electron velocity leads to the process of 'micro-bunching' and the amplification is reached within one passage of the electrons through a long undulator. For generation of FEL radiation at short wavelengths the SASE principle is necessary, because:

1. The normal-incidence reflection of mirrors decreases strongly at short wavelengths and therefore the use of an optical cavity resonator to build up high brightness radiation upon several passes of the electron beam through the undulator is not possible.

2. No widely tunable laser exists for wavelengths shorter than the visible which can produce a sufficient input power.

SASE-FELs belong to the most attractive candidates for extremely brilliant, coherent light-sources down to the Angström regime. As a proof of principle, demonstration of an exponential growth of radiation power and even saturation at a wavelength of around 100 nm was shown at TTF1 [4]. The expected peak brilliance can be more than eight orders of magnitude higher than that of state-of-the-art synchrotron radiation sources (see Figure 2.1).

At a wavelength around 100 nm, the TTF1-FEL reached such high power densities, that nonlinear processes were induced in the interaction with matter. Up to 10^{13} photons were emitted in pulses of 30-100 fs length.

As mentioned before, SASE-FELs are capable of producing much shorter wavelengths. For example, the upgrade TTF2-FEL, which will start its operation in 2004, is designed to finally reach 6 nm. Moreover, the planned X-FEL at DESY in Hamburg is designed to enter the hard X-ray regime with wavelengths as short as 3 Å. Thereby enabling the fascinating possibility to investigate, for example, biological samples in vitro at atomic resolution, owing to the very intense peak power and pulse-lengths in the fs-time range.

As an additional type of light source in the EUV and XUV radiation regime ($\lambda_r \sim 100 - 10$ nm), great progress was very recently promised by the use of higher harmonics [6]. However, the limit of this principle of generation is expected to be around 10 nm.
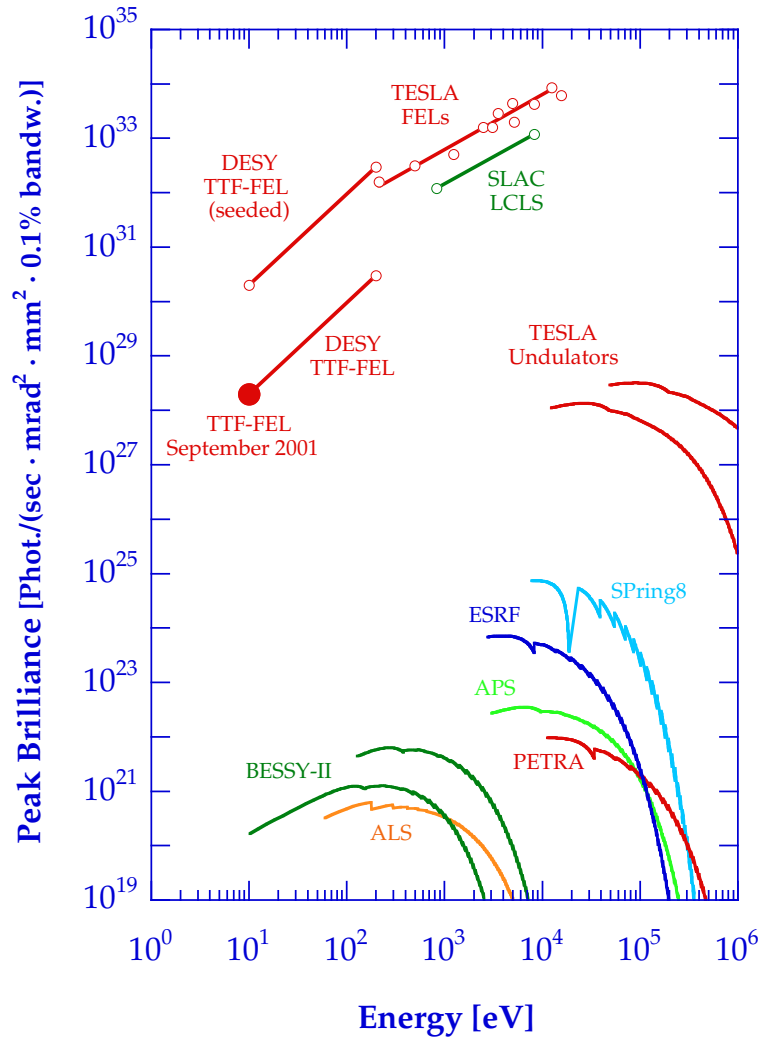
Figure 2.1: Expected peak brilliance of proposed SASE-FELs in comparison with state-of-the-art synchrotron radiation sources. The large dot marks the experimental result from the TTF1-FEL [5]

.

2.1.2 SASE principle

In a SASE-FEL an electron bunch passes a long undulator. In the magnetic field of the undulator the electrons move along a curved periodical trajectory. As a result of their acceleration they emit radiation, which is usually referred to synchrotron radiation (SR). In an undulator the radiation emitted by electrons travelling along the individual magnetic periods overlaps and interferes. The wavelength λ_r of the first harmonic of

the spontaneous, on-axis undulator emission is given by:

$$\lambda_r = \frac{\lambda_u}{2\gamma^2}(1 + \frac{K^2}{2})$$ (2.1)

Here λ_u is the length of the undulator magnet period, $K = \frac{e\lambda_u B_0}{2\pi m_e c}$ is the undulator parameter with B_0 the peak magnetic field of the undulator and $\gamma = E/m_e c^2$ is the relativistic factor. This interference condition basically means, that the electrons slip by one radiation wavelength with respect to the electromagnetic field, during one undulator period [7]. The 'slippage of the electrons' coincides with the condition for maximum energy exchange between (SR) light field and the electrons.

Energy exchange
To amplify the spontaneous emission the electrons must lose energy in favour of the radiation field, that is ΔW in the following equation has to be positive.

$$\Delta W = -e \int \vec{E}_r \cdot d\vec{s} = -e \int \vec{v} \cdot \vec{E}_r \cdot dt$$ (2.2)

It turns out [8] that this requirement is only satisfied, if the phase Ψ between the radiation field $\vec{E}_r$ and the transverse component of the electron velocity v_x stays nearly constant along the whole undulator path,

$$d\Psi = (k_r dz - \omega_r dt) + k_u dz = 0$$ (2.3)

where $k_r = 2\pi/\lambda_r$ and $\omega_r = 2\pi c/\lambda_r$ are the wave-vector and the frequency of the radiation field and $k_u = 2\pi/\lambda_u$. Using $dz = v_z dt$ the synchronisation between electron movement and electromagnetic field is more apparent.

$$\frac{\lambda_u}{v_z} = \frac{\lambda_r}{c - v_z}$$ (2.4)

Synchronisation and thus energy exchange from the electrons to the radiation field happens, when the radiation overtakes the electron beam during one undulator period by one wavelength.

 This result is qualitatively described in Figure 2.2. An electron undulates in the magnetic field $\vec{B}$ of the undulator. At a certain time the electron has a velocity component $+v_x$. Given that the electric field E_x of the light wave moving alongside the electron beam has at this position and time a maximum and acts in the same direction, then the negatively charged electron is decelerated (position z=0 in Figure 2.2). Half an undulator period later the electron crosses again the central axis of the undulator and has now a velocity component $-v_x$. If synchronization is fulfilled then the electric field
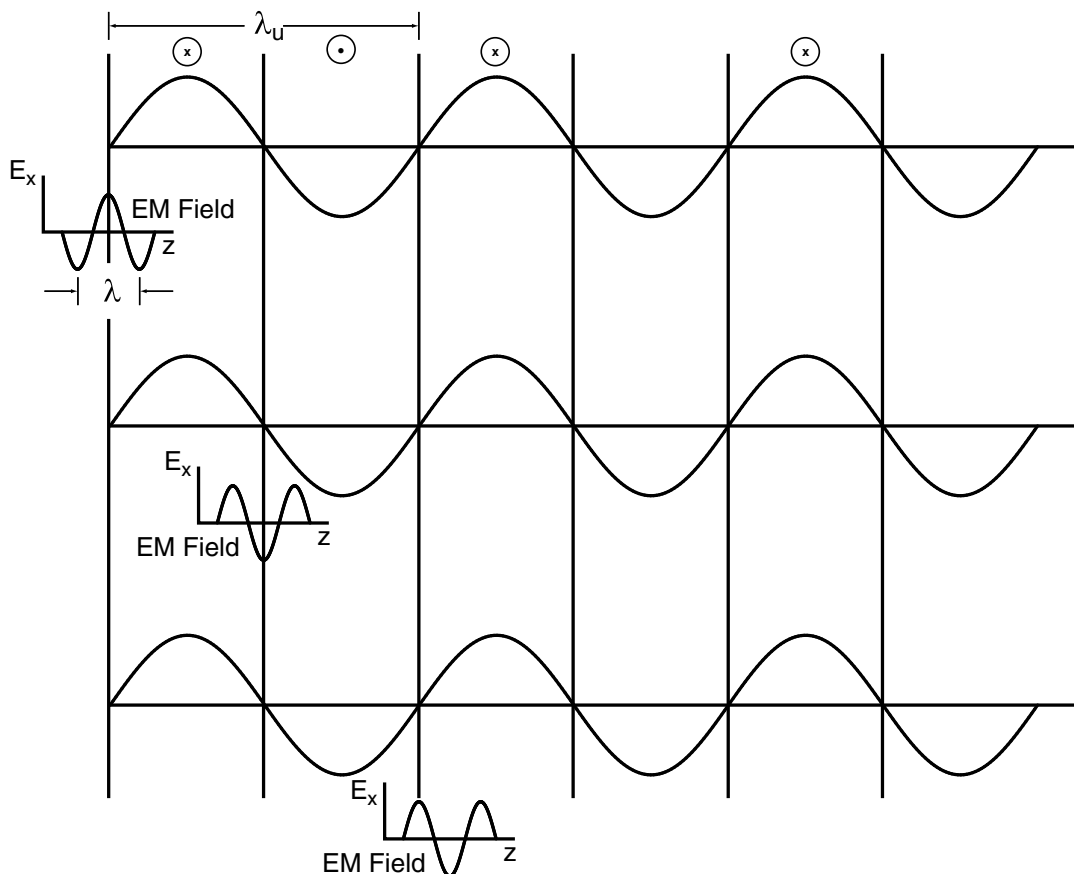
Figure 2.2: Electron orbit in a periodic undulator field (undulator period λ_u). The direction of the magnetic field B is indicated in the figure. Electron and electric field of the light wave are depicted at three distinct positions along one undulator period: a) z=0; b) z=λ_u/2; c) z=λ_u

of the light wave has advanced by $\lambda_r/2$ and now acts in the opposite direction which results in a further deceleration (z=λ_u/2). After one undulator period the light wave has outrun the electron by a full wavelength λ_r and the electron loses energy again (z=λ_u). As long as the phase between electron and light wave stays nearly constant, energy is transferred from the electron to the light wave along the whole undulator. This is essentially the same condition as follows from equation (2.1) and is one of the prerequisites for the SASE process of the FEL.

In a SASE-FEL the radiation pulse and the electron bunch overlap along the whole undulator. The coupling of the electric field $\vec{E}_r$ of the radiation to the transverse component v_x of the electron velocity $\vec{v}$ leads then also to a modulation of the electron

distribution into micro-bunches.[1]

Figure 2.3: Sketch of the self-amplification of spontaneous emission (SASE) in an undulator. In the lower part of the figure the longitudinal density modulation (micro-b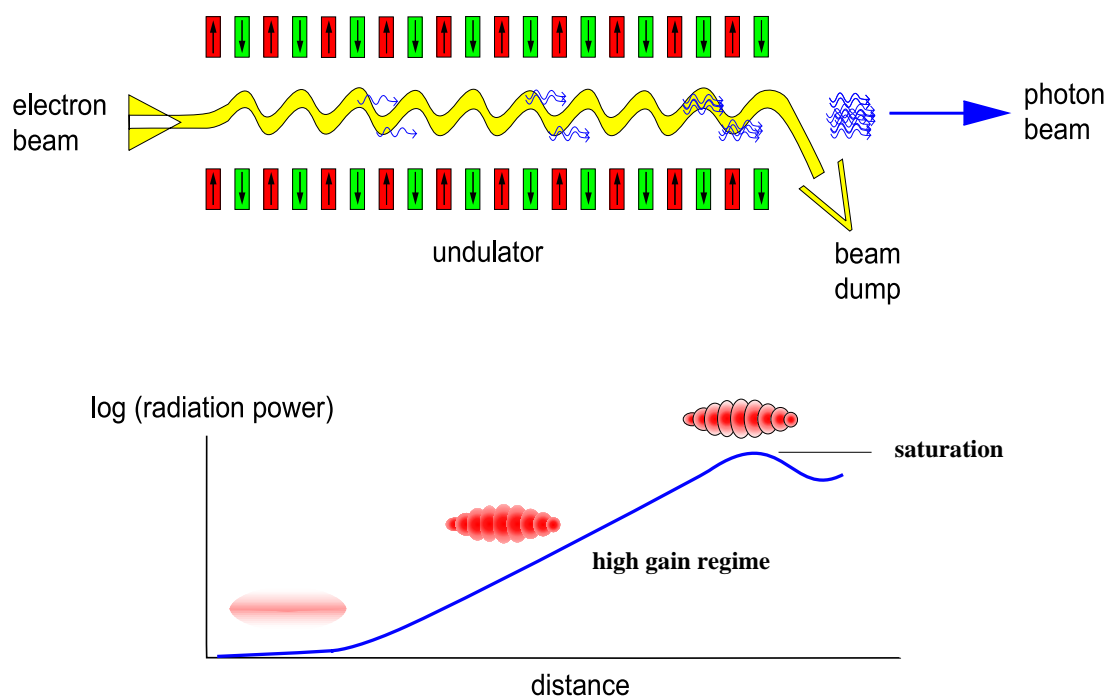unching) is shown together with the resulting exponential growth of the radiation power along the undulator in the high gain regime. At maximum micro-bunching the radiation power output becomes saturated [7].

Micro-bunching
The modulation of the electron distribution results from the interaction of the electrons with the electric field of the electromagnetic wave. This interaction leads to the process of micro-bunching, which is depicted in Figure 2.3. Electrons with different phases with respect to the light wave are accelerated or decelerated. As a result, the longitudinal velocity v_z of the electrons is modulated within the radiation wavelength λ_r. This velocity modulation is transformed into a density modulation of the electron beam. The longitudinal distribution of the electrons resembles dense slices (micro-bunches) separated by a wavelength λ_r. With complete micro-bunching, all electrons radiate almost in phase and the radiation power P becomes proportional to N_e^2, $P \propto N_e^2$, as opposed to $P \propto N_e$ of individually radiating electrons in a not modulated bunch.
During the operation of TTF1 it became obvious, that not the whole radiating part of

---

[1]The process of micro-bunching is not present in conventional undulator beam-lines, because the beam quality delivered by storage rings is not high enough.

the electron bunch radiates coherently. Actually, the radiating part is subdivided into 'longitudinal modes' which emit coherently. The length of the longitudinal modes is referred to as the 'coherence length' and the radiation power of the individual longitudinal modes is then proportional to N_e^2, where N_e is the number of electrons within one coherence length. The radiation emitted from individual modes differs slightly in wavelength. Coherent radiation from different longitudinal modes was measured and used to estimate the radiation pulse length of the FEL pulse, see section 2.1.6.

Gain along undulator
Along the undulator the radiation power $P(z)$ grows exponentially with the distance z

$$P(z) = AP_{in}exp\left(\frac{2z}{L_g}\right) \tag{2.5}$$

until the bunch is completely modulated in micro-bunches and saturation is reached. In equation (2.5) L_g is the field gain length, P_{in} the effective input power and A the input coupling factor. In a one-dimensional FEL theory A is equal to 1/9 [9].

2.1.3 VUV-FEL at DESY
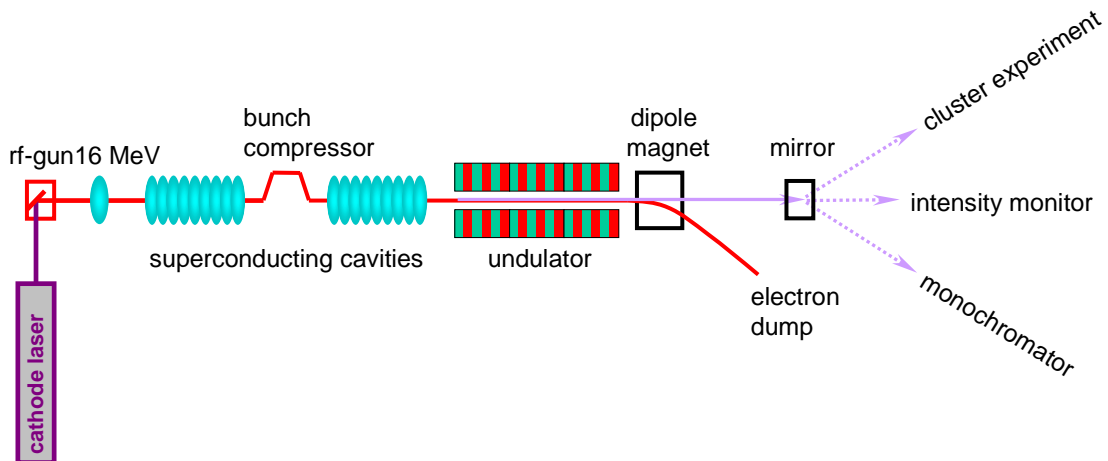
Figure 2.4: Schematic layout of phase 1 of the SASE-FEL at the TESLA Test Facility at DESY [10]. The linear accelerator contains two 12.2 m long cryogenic modules each equipped with eight 9-cell superconducting accelerating cavities. The FEL radiation is reflected by a mirror into one of the three experimental branches. They can not be used simultaneously. The total length is 100 m.

The free-electron laser at the TESLA Test Facility (TTF) at DESY produces radiation during a single pass of an electron beam through a long undulator. The amplification

process in the SASE-FEL develops from shot noise in the electron beam and intense, coherent radiation is produced in a narrow band at the resonance wavelength. In the high gain linear regime, the radiation power $P(z)$ grows exponentially with the distance z along the undulator [4]. The radiation wavelength is continously tunable from 80-180 nm.

Electrons:	
beam energy	220–270 MeV
bunch charge	2.7–3.3 nC
charge in lasing part of the bunch	0.1–0.3 nC
peak current	(1.3 ± 0.3) kA
rms energy spread	(150 ± 50) keV
rms normalised emittance	$(6 \pm 2)\,\pi$ mm·mrad
bunch spacing	0.44 / 1 μs
number of bunches in a train	up to 70
RF pulse repetition rate	1 Hz
Undulator:	
undulator period λ_u	27.3 mm
peak magnetic field	0.46 T
total magnetic length	13.5 m
Photons:	
wavelength range (with saturation power)	80–120 nm
pulse energy	30–100 μJ
pulse duration (FWHM)	50–200 fs
peak power level	1 GW
average power	up to 5 mW
spectral width (FWHM)	1%
spot size at undulator exit (FWHM)	250 μm
angular divergence (FWHM)	260 μrad

Table 2.1: Main parameters of the FEL operation in Phase 1 of the TESLA Test Facility (TTF1)

The injection of the electron bunch is based on a laser-driven $1\frac{1}{2}$-cell radio frequency (RF) gun electron source operating at 1.3 GHz. The injector mainly consists of a mode-locked solid-state UV laser system, a Cs_2Te photocathode and an RF gun operating at 1.3 GHZ. Illumination of the cathode with a train of UV laser pulses produces an electron bunch, which is accelerated in the RF gun to 4 MeV. The following supercon-ductive cavity boosts the energy to 16 MeV.
The main accelerator contains two 12.2 m long superconducting acceleration modules, separated by a magnetic bunch compressor. The bunch compressor acts as a chicane, in which the (fast) front electrons move on a longer trajectory than the (slower) tail

electrons. Thereby the bunch length is reduced, which is necessary to reach a high peak current. Downstream of the bunch compressor the charge distribution in the electron bunch is strongly non-Gaussian with a narrow leading peak and a long tail [4].

The undulator is a permanent magnet device with a 12 mm gap and an undulator parameter of K=1.17. As the electron bunch enters the undulator the SASE process starts as described in section 2.1.2. About 5 m downstream from the undulator exit a dipole magnet separates the electron beam from the FEL radiation.

The experimental station consisted of three separate branches, one of which was reserved for user experiments. The two other branches were available for photon diagnostics. Next to the users branch, the pulse energy of the FEL pulses was measured with an MCP, see section 2.1.5. In the third branch the spectral distribution of the FEL radiation was characterised by a monochromator.

2.1.4 Time structure
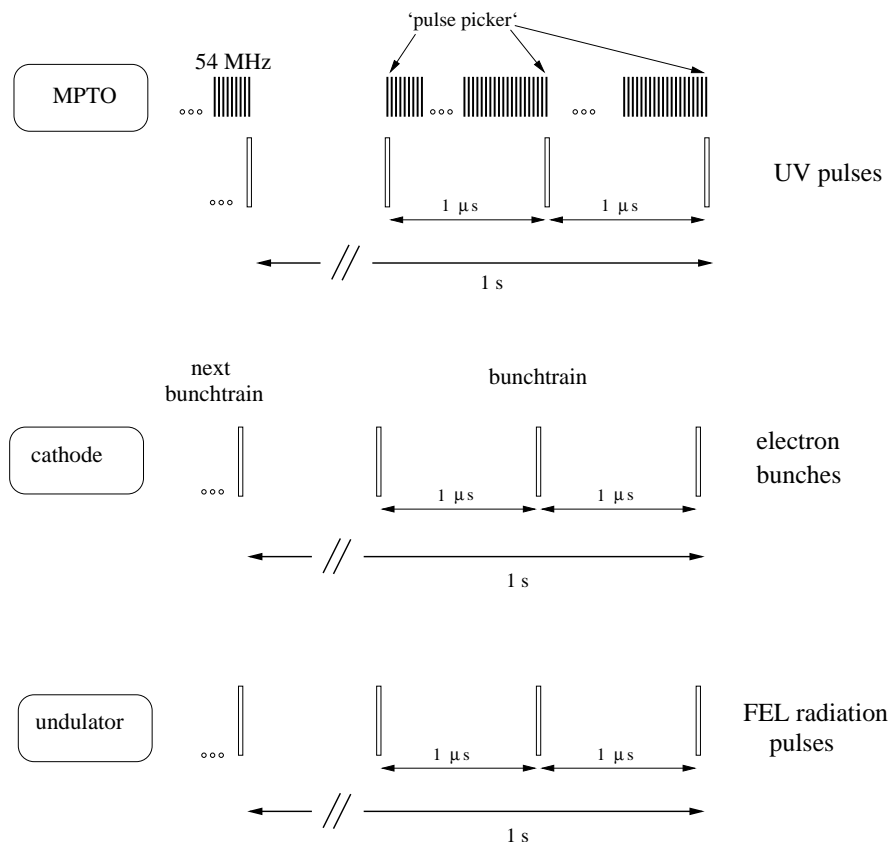

Figure 2.5: Time structure of FEL radiation (1 MHz mode): (top) initial IR pulses of the laser and selected UV pulses illuminating the cathode; (middle) electron bunches and (bottom) FEL radiation pulses. Durations of the particular pulses are $\simeq 7.1$ ps for the UV pulses, $\simeq 20$ ps for the electron bunches and $\simeq 50\text{-}200$ fs for the FEL radiation pulses.

In a SASE-FEL every injected electron bunch generates one radiation pulse. Therefore the time structure of the radiation refers back to the repetition rate of bunch trains, the number of electron bunches in a bunch train and the temporal separation between two consecutive electron bunches. In Figure 2.5 the evolution of the time structure is illustrated schematically.

At TTF1 the temporal separation as well as the number of electron bunches could be varied by the use of a pulse picker. This assembly consisted of a Pockels cell together with a polariser and reduced the 54 MHz output of a mode locked pulse train oscillator (MPTO). During the operation of TTF1 up to 70 pulses were 'picked' with time gaps of $10\,\mu s$, $1\,\mu s$ and $0.444\,\mu s$, which results in operating frequencies of the pulse picker of 0.1 MHz, 1 MHz, 2.25 MHz respectively. In any case, bunch trains were injected at a repetition rate of 1 Hz.

Later in this chapter the experimental set-up and the detectors will be described in detail. Because of limitations in the minimum flight-time of ions in the mass spectrometers the 2.25 MHz mode was not used. For the cluster ion mass spectrometer the 1 MHz mode suited best. In the case of the bi-polar detector a temporal gap of $10\,\mu s$ was necessary.

2.1.5 Intensity fluctuations

In a SASE-FEL the radiation energy strongly fluctuates from pulse to pulse. The fluctuations are inherent to the SASE process and result from the start of the amplification process from shot noise. In the left part of Figure 2.6 measurements of the energy of subsequent radiation pulses are given. Every circle represents the energy of a single pulse. Apparently, the energy varies strongly from pulse to pulse.
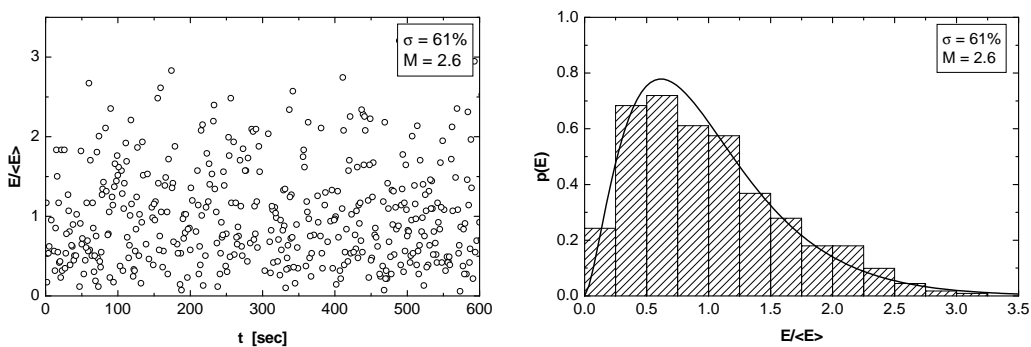

Figure 2.6: Pulse-to-pulse fluctuation of SASE pulses [5]. Left: measured single pulse energy versus time; Right: histogram of probability distribution extracted from the measurement

For the monitoring of the pulse energy a micro-channel plate (MCP) based detector was

used. The set-up consisted of a thin gold wire mesh that scattered a tiny fraction of the FEL radiation onto the MCP. Despite its characteristic nonlinear gain as a function of supply voltage, careful calibration of the MCP [11] allowed for absolute measurements of the radiation energy in the radiation pulses. The pulse energy E_{puls} was calculated using

$$E_{puls}[nJ] = 0.3 \cdot A \cdot Q_{puls}[nC] \tag{2.6}$$

where Q_{puls} is the total charge of the electron bunch. The factor A is the amplification of the MCP signal as compared to the MCP signal of spontaneous radiation.

In the first experimental run the MCP set-up and the cluster experiment were located in different experimental branches (see Figure 2.4). Therefore it was not possible to measure directly the pulse energy belonging to each ion mass or photoelectron spectrum. However, combining the stray-light peak seen in the experimental spectrum with pulse energy measurements of the MCP set-up allowed for assignment of the power density for each experimental single-shot spectrum. Before the second experimental run another intensity monitor, working in the same way as described above, was integrated in the same branch as the cluster experiment and served as an online monitor.

In both experimental sets the FEL beam was reflected and focussed into the experimental chamber by the use of three optical elements. A Ni-coated mirror reflects the FEL beam into the experimental branch, an ellipsoidal mirror (Au-coating) focuses the beam and finally a plane mirror (Au-coating) guides it into the experimental chamber. The respective reflectivities [2] of the optical elements add up to an overall reflectivity of 20 %. The photon fluence (and thus the radiation pulse energy E_{puls}) was corrected for the reflectivity throughout the work.

2.1.6   Pulse length

The duration of the radiation pulse τ_{rad} is a very important parameter for all user experiments at the FEL. It can be estimated by using statistical properties of the SASE process.

The SASE process starts from shot noise. As shot noise in the electron beam causes fluctuations of the beam density, which are random in space and time [12], the radiation produced by such a beam exhibits random amplitudes and phases in time and space. Therefore the radiation can be described with statistical methods. In the regime of exponential growth, the radiation pulse energy E is expected to fluctuate according to a gamma distribution $p(E)$ [13],

$$p(E) = \frac{M^M}{\Gamma(M)} \left(\frac{E}{\langle E \rangle} \right)^{M-1} \frac{1}{\langle E \rangle} exp \left(-M \frac{E}{\langle E \rangle} \right) \tag{2.7}$$

where $\langle E \rangle$ is the mean energy, $\Gamma(M)$ is the gamma function with the argument M, $M = 1/\sigma^2$ and $\sigma^2 = \langle (E - \langle E \rangle)^2 \rangle / \langle E \rangle$ is the normalized variance of E. The parameter

---

[2]Under grazing incidence (10°) the reflectivities become: Ni-coating 40 %, Au-coating 70 %.

M can be interpreted as the number of longitudinal 'modes' in the radiation pulse, which in turn is the number of spikes in the spectral distribution.
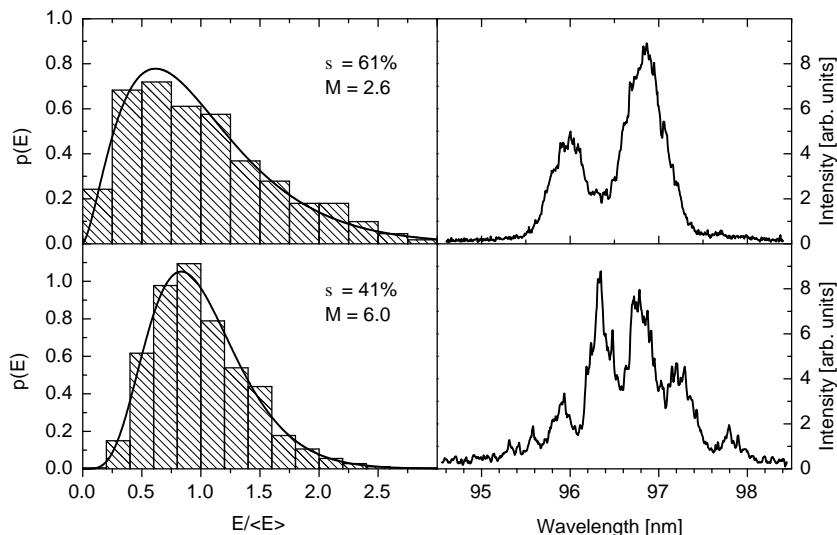
Figure 2.7: Determination of radiation pulse length by statistical and spectral methods. Left: Probability density distribution of the energy in the radiation pulse for different tailorings of the electron bunch [14]. The FEL has been operated in the high-gain linear regime. Solid curves represent gamma distributions. Right: Single-shot spectra for the corresponding modes of operation.

In Figure 2.7 statistical analysis and spectral measurements are compared for two different settings for the driving electron bunch [3]. The left part of Figure 2.7 shows the probability density distribution of the pulse energy $p(E)$. The solid curves represent gamma distributions with parameters M=2.6 and M=6. As is readily seen, these values derived from the statistical analysis correspond to the number of spikes in the measured single shot spectra given in the right part of Figure 2.7. Additionally, the number of modes in the spectral and in the temporal distribution is the same and the duration of the radiation pulse τ_{rad} becomes,

$$\tau_{rad} \simeq M \cdot \tau_c \qquad (2.8)$$

where the coherence time τ_c is the typical duration of one mode in the time domain. The coherence time t_c has been measured to be $t_c \simeq 20\,\text{fs}$ [4]. This results in pulse durations of $\tau_{rad} \simeq 50\,\text{fs}$ and $\tau_{rad} \simeq 120\,\text{fs}$ for the pulses shown in Figure 2.7 top and bottom respectively.
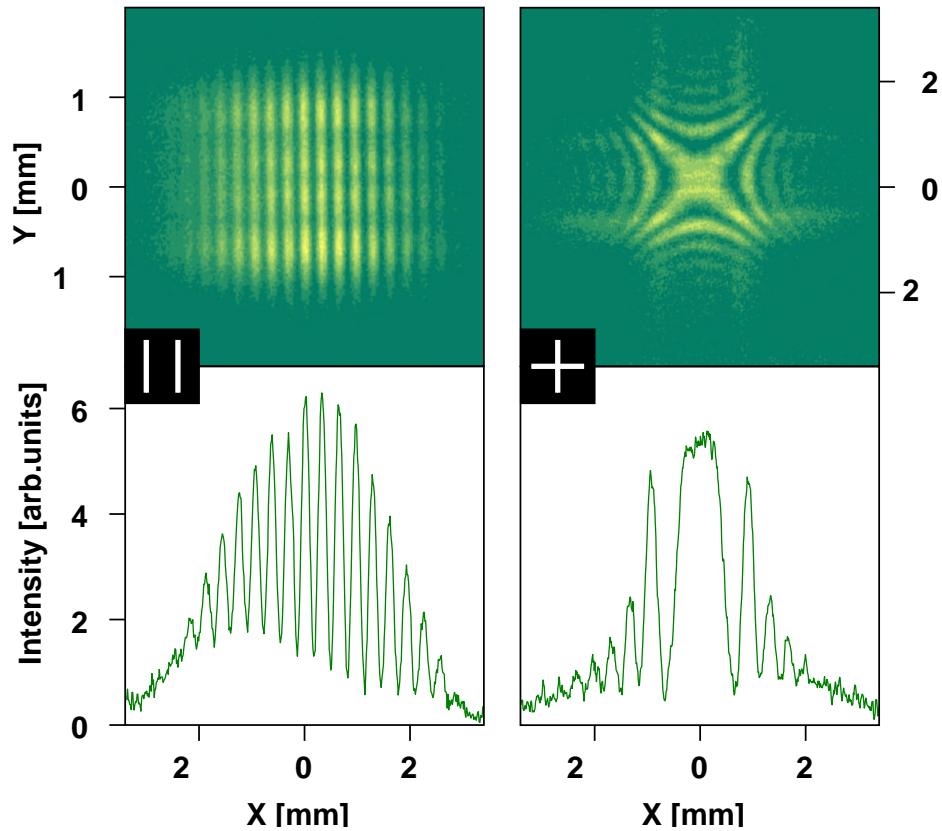
Figure 2.8: Diffraction patterns for two different slit arrangements illustrating the transverse coherence of the FEL radiation. Left: double slit, each slit $2\,\mathrm{mm}\times200\,\mu\mathrm{m}$, horizontal slit separation $1\,\mathrm{mm}$; Right: crossed slits, each slit $4\,\mathrm{mm}\times100\,\mu\mathrm{m}$. The slits are located $12\,\mathrm{m}$ behind the undulator exit. The images have been taken as a sum of a few consecutive FEL radiation pulses with a wavelength of $95\,\mathrm{nm}$. The lower part shows horizontal cuts through the centre of the respective diffraction pattern [5, 15].

2.1.7 Coherence

The emission of coherent radiation is one of the key features of an FEL. Coherence can be subdivided into two classifications, *longitudinal* and *transverse coherence*. The physical sense of the longitudinal coherence can be described by assuming a plate which splits the radiation pulse. The resulting two pulses are made to pass different path lengths, before they are combined together again. If the difference in pathlength is less than the coherence length $c\tau_c$, an interference pattern is observed for a shot-to-shot averaging [4]. This means that the radiation field is correlated within the coherence length [9].

---

[3]At TTF1 different bunch compressor settings were used to change the shape of electron bunches.

[4]Here the coherence time τ_c is related to the bandwidth $\Delta\omega$ of the radiation pulse by $\tau_c \simeq 1/\Delta\omega$.

Transverse coherence can be explained by assuming that the radiation pulse is directed onto a plate with two pinholes. If the pinholes are located close to each other, a clear interference pattern is observed. Now the distance between the pinholes is increased. At a certain distance $D > \Delta r_c$ no interference pattern is observed anymore after averaging over the ensemble of pulses. Qualitatively, Δr_c can be referred as the transverse coherence length [9]. The transverse coherence of the FEL radiation was measured at TTF1 and the resulting diffraction patterns are shown in Figure 2.8.

In Figure 2.8 two diffraction patterns of the FEL radiation measured at a distance of 3 m behind a double slit and two crossed slits are shown [5, 15]. Radiation from the FEL was converted to visible light by using a Ce:YAG fluorescent screen, thereby enabling the recording of the diffraction patterns. The images displayed in Figure 2.8 were recorded with a gated CCD camera. Intensity profiles are depicted in the lower part of the figure. From the high fringe visibility it was concluded, that the radiation of the FEL exibits a high degree of transverse coherence.

As mentioned earlier (see sections 2.1.2 and 2.1.6) statistical analysis of the pulse energy and spectral measurements of the FEL radiation indicate, that the radiating part of the electron bunch emits not with full longitudinal coherence but is subdivided into individually coherent radiating parts. The individually radiating parts are referred to as 'longitudinal modes'. FEL radiation therefore consists of a few longitudinally coherent contributions.

2.1.8 Higher harmonics
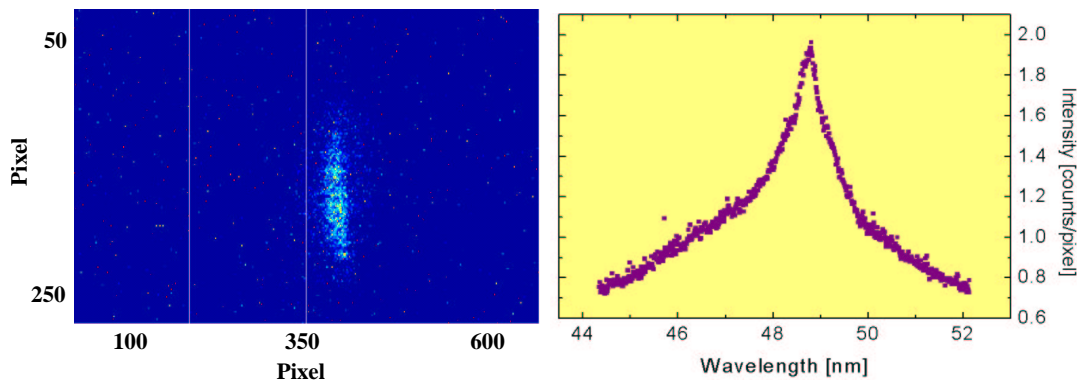
Figure 2.9: Spectral measurement of the second harmonic of the FEL radiation. On the left hand side, the CCD image of the dispersed 2nd harmonic of the FEL radiation in the exit plane of the monochromator is shown. The dispersive direction is in the horizontal. For the CCD image 1200 single shots were integrated. On the right hand side the spectra are evaluated quantitatively [10].

In an undulator not only radiation with the wavelength λ_r of the first harmonic is

produced, but also radiation corresponding to higher harmonics. The wavelength of a higher harmonic is $\lambda_n = \lambda_r/n$ where n is the number of the harmonic and the total radiated power decreases with increasing n. The 3rd and all uneven harmonics result from a harmonic modulation of the transverse component of the electron velocity v_x. Whereas for uneven harmonics the radiated power is maximal in the forward on-axis direction, the angular distribution of radiation from even harmonics, which result from harmonic modulations of the longitudinal electron velocity v_z, is different and theoretically zero in the forward on-axis direction [16].

Figure 2.9 displays spectral measurements of the 2nd harmonic during the operation of TTF1. The picture to the left gives a CCD image of the dispersed 2nd harmonic FEL radiation after integrating over 1200 single shots. On the right hand side the spectrum is evaluated quantitatively. Additional measurements with a gas ionization detector determined an upper limit of 1% for the on-axis radiated power with respect to the first harmonic [10].

The wavelength of the 3rd harmonic was beyond the spectral range of the monochromator. So no quantitative measurements were taken. However, from theoretical considerations its radiation power was estimated to be $\sim 0.1\%$ [17].

2.2 Experimental set-up

Spectroscopy on clusters with synchrotron radiation is a longterm scientific goal in our group. In 1989 our group started with valence shell spectroscopy of rare gas clusters at the experimental station CLULU [18]. A few years later a modified molecular beam machine allowed for the extension of these investigations to inner shell processes at the beam-line BW3 [19].

Design and construction of the set-up in this work was based on these earlier experiments. However, the different type of light-source and the location of the experiment inside the main accelerator tunnel less than 50 m away from the superconducting cavities imposed certain restrictions on the set-up.

The whole vacuum system of TTF1 including the experimental branches was operated without windows. Therefore the experimental set-up had to be 'oil-free' and 'dust-free'. Hydrocarbons and dust are expected to degrade the performance of the FEL and the optical elements.[5] To prevent degradation the partial pressure of gases having a mass above 45 amu was kept below 10^{-3} of the total pressure in the vacuum chamber. The contamination with dust particles was kept at the lowest possible level by following a strict procedure. All parts were cleaned in the main clean room at the DESY site. Then the clean parts were packed and transferred to a mobile clean room near the beam-line. Due to rigorous space restrictions at the beam-line in the TTF-tunnel the set-up could not be mounted completely outside the tunnel. Therefore a custom-made clean room was built in the TTF-tunnel, where the set-up was completed and connected to the beam-line. Finally , because of the location in the tunnel the operation of the set-up had to be fully remote controlled.

Figure 2.10 shows an overview of the experiment. The main vacuum chamber with the cluster source and the integrated mirror chamber was mounted on a frame. The mechanical degrees of freedom allow a preliminary adjustment of the set-up. Additionally, the main chamber could be moved in the plane of the picture by remote control during operation. The integrated mirror-chamber focuses the FEL radiation by an assembly of an elliptical and a plane parallel mirror. The shutter chamber contains a number of apertures ranging from 1 mm to 5 mm and it connects the experiment to the beam-line via a bellow.

---

[5]For example, dust particles are expected to cause arcs on the surface of the accelerating cavities, thereby limiting the acceleration gradient.
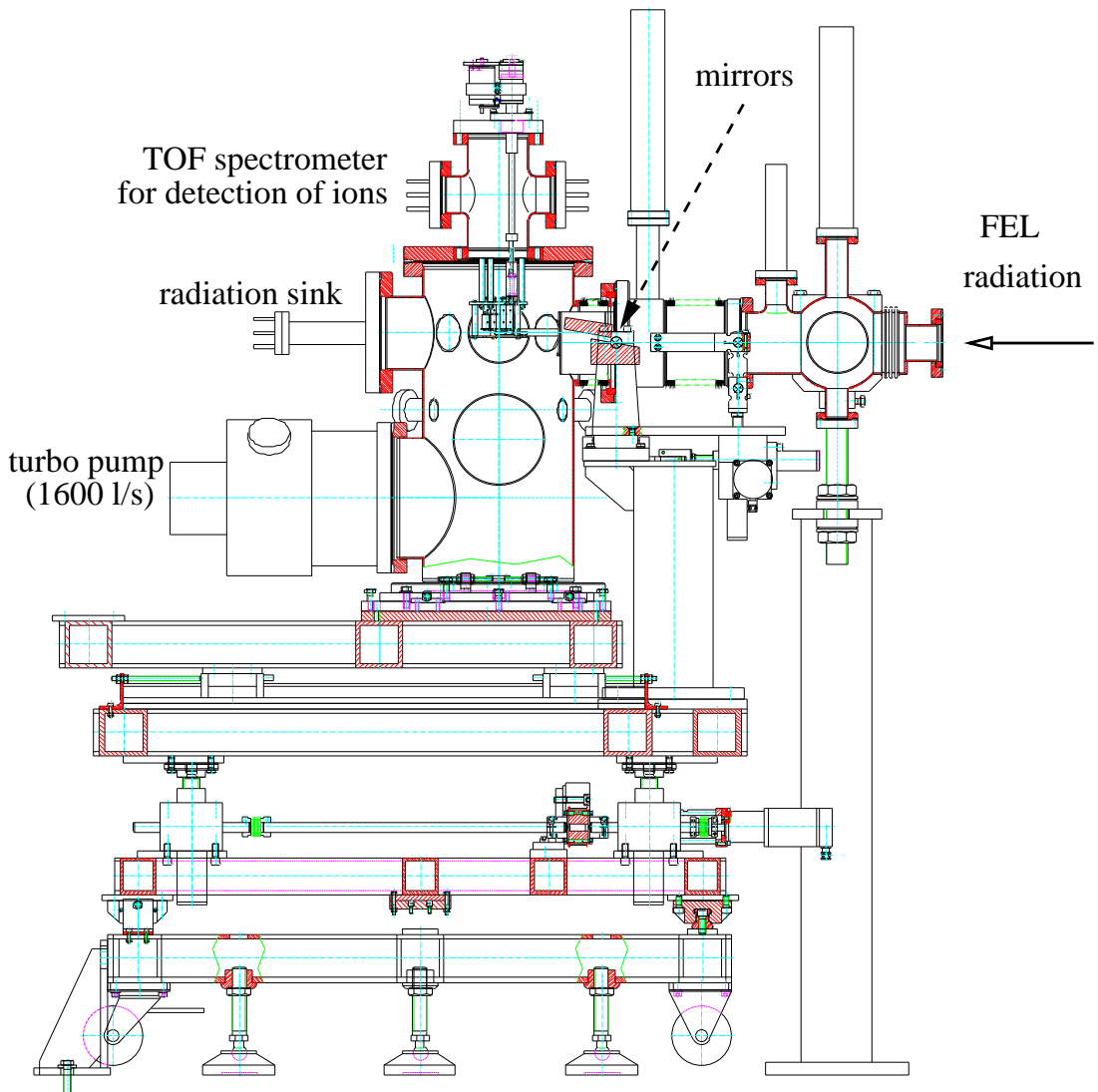
Figure 2.10: Longitudinal section of the set-up with cluster ion TOF. The cluster source, the focus camera and the quadrupole mass spectrometer are not depicted. The cluster source is located in front of the section. Focus camera as well as quadrupole mass spectrometer are located behind the section.

2.2.1 Mirror-chamber

In order to reach the nonlinear power density regime the FEL radiation was focused with an ellipsoidal mirror. At the undulator exit the radiation spot size (FWHM) was $250\,\mu$m with an angular divergence of $260\,\mu$rad [5]. After $13\,$m the radiation spot was enlarged to $\simeq 3.4\,$mm (FWHM). From ray tracing calculations the minimum spot size at the focus is expected to be $\simeq 5\,\mu$m. Important parameters are given in Table 2.2.
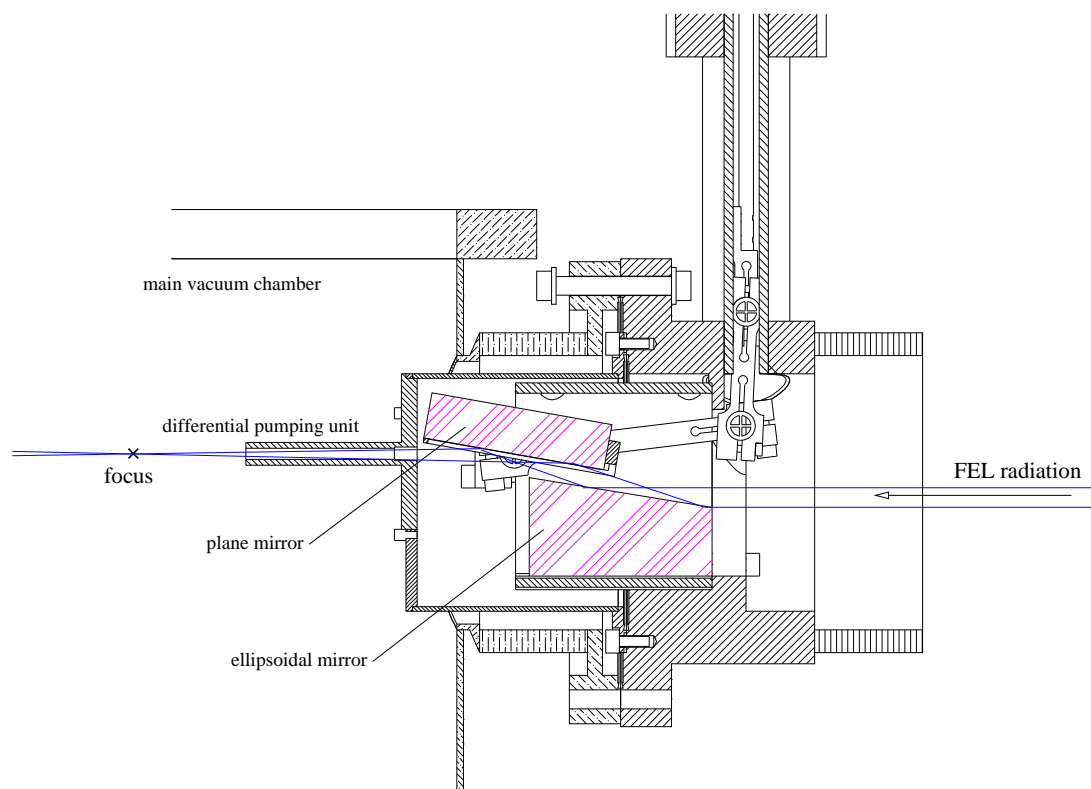
Figure 2.11: Longitudinal section of the mirror chamber. A small tube ($\varnothing 2\,mm$) separates the mirror chamber from the main chamber. The adjustment of both mirrors was remote controlled.

source distance	13 m
image distance (centre of TOF)	0.2 m
rad. spot size (FWHM) at:	
undulator exit (source)	$\simeq 250\,\mu$m
ellipsoidal mirror	$\simeq 3400\,\mu$m
minimum spot size at centre of TOF (focus)	$\simeq 20\,\mu$m

Table 2.2: Optical parameters of experiment.

2.2.2 Molecular beam machine for cluster preparation

In the present experiment clusters were prepared using the method of supersonic jets. In this method gas expanded from a high pressure p through a small orifice with diameter d into vacuum. This method is widely used to prepare cluster beams. Methods of the spectroscopy and preparation of molecular beams are discussed in [20]. A detailed theory of condensation in a supersonic expansion is described by Hagena and Obert

[21].

During the expansion the random velocities of the gas atoms are transformed into directional velocities along the beam axis. While the on-axis velocity increases the relative speed of the atoms is lowered and the beam is cooled efficiently. Condensation starts when the temperature drops so rapidly that the beam enters the supersaturated regime. After 4-6 mm the beam passes a differential pumping stage (skimmer).

The growth of the clusters is limited in two ways. First, as condensation goes on, the particle density is continously reduced, thereby reducing the number of collisions. Second, the process of condensation releases thermal energy, which heats up the cluster. Each time an atom condenses onto the cluster, the heat of formation is added to the cluster's internal energy. Once past the skimmer the particle density is to low for 'cooling' collisions. The cluster can cool only by evaporation of atoms. A generally accepted formalism to describe cluster formation relies on the dimensionless parameter Γ^* introduced by Hagena [22].

$$\Gamma^* = \frac{K \cdot p \cdot d^{0.85}}{T^{2.2875}} \tag{2.9}$$

The diameter of the nozzle d is measured in μm, the stagnation pressure p before the nozzle in mbar and the temperature T of the nozzle in Kelvin. The parameter K is calculated from the sublimation energy and describes the ability to condensate. For xenon K=5554. In this work the cluster size is determined by the method of Buck and Krohne [23]. As the authors point out for $350 \leq \Gamma^* \leq 1800$ the average cluster-size $\bar{N}$ has to be calculated by

$$\bar{N} = 38.4 \left(\frac{\Gamma^*}{1000} \right)^{1.64} \tag{2.10}$$

For larger values of Γ^*

$$\bar{N} = 33 \left(\frac{\Gamma^*}{1000} \right)^{2.35} \tag{2.11}$$

should be used. Both equations hold for nozzles with a simple orifice. For nozzles with a conical shape (like the one used throughout this work) the nozzle diameter d in equation (2.9) has to be replaced by the equivalent diameter d_{eq} of the conical nozzle. d_{eq} is a function of orifice d and the half opening cone angle θ, $d_{eq} = 0.719 \frac{d}{tan(\theta)}$. This yields $d_{eq} = 268\,\mu$m for the conical nozzle ($d = 100\,\mu$m, $\theta = 15°$) used in this work.

A conical nozzle was used, because at the same mass flow it allows the preparation of much larger clusters than simple orifices.[6] In the FEL-experiment the total pressure in the main vacuum chamber was limited to 10^{-5} mbar, due to the presence of multi-channel plates (MCP) in the time-of-flight (TOF) detectors. Therefore the conical nozzle was mounted on a commercial molecular beam source (Thermionics Northwest, Inc.) and the assembled cluster source was operated in pulsed mode. Throughout this work the repetition rate is 1 Hz (synchronised with the FEL) with an opening time of

---

[6]Additionally, the beam is also much more collimated.

5 ms. In this way the gas flow reduces to $5 \cdot 10^{-3}$ of that of a continuous source. Previous tests at the experimental station CLULU confirmed, that the cluster preparation in pulsed mode followed the scaling laws given above for opening times longer than 2 ms. The gas flow is further reduced by the use of a skimmer, which allows only a small portion of the cluster beam to enter the main chamber and therefore reduces the background pressure by two orders of magnitude. Consequently, cluster sizes covered a size range up to [7] $\bar{N} \sim 90,000$ (stagnation pressure p= 20 bar) in the case of xenon.

2.3   Detectors and data acquisition

Time-of-flight techniques were used for the detection of ions and electrons. An advantage of the present experiment is the simultaneous detection of ionic fragments with different masses in combination with the high time resolution of multi-channel plate (MCP) detectors. The principle of operation is as follows:

Under the influence of a pull-in voltage charged particles are drawn away from the interaction region and guided onto an MCP detector. Depending on the mass to charge ratio particles need a specific time to cover the distance to the MCP. The delay between the detection of a particle and the (nearly) instantaneous signal of scattered light from the FEL enables identification of the charge to mass ratio.

Energetic particles appear in the time of flight spectrum shifted relative to the position of particles initially at rest. As mass and charge state are already identified, the deviation in flight time can be used to determine the initial kinetic energy. In this way ejection energies of ions after Coulomb explosion of the parent cluster may be determined. This is shown in section 3.3. The energy of photoelectrons is discussed in section 3.4.

Two different TOF spectrometers are described in sections 2.3.1 and 2.3.2. The *cluster ion TOF* is a compact spectrometer with a short flight path for the detection of ionic fragments of clusters. The *bi-polar TOF* with its field free drift tube of 150 mm suits the requirements of time resolution necessary for photoelectron spectra. MCP detectors in both spectrometers couple out the signal at ground potential and both are equipped with 50 Ω impedance matched output connectors.

In section 2.3.4 the *data acquisition* by recording the analogue output of the spectrometers with a digital sampling oscilloscope and then storing every single spectrum separately on hard disk is described. It turns out that subsequent TOF spectra show a degradation of the signal. Therefore only spectra following the first radiation pulse are considered throughout the whole work.

---

[7]The size distribution is broad. As a rule of thumb the width of the distribution approximates the average size $\bar{N}$ (e.g. $\bar{N} = 100 \equiv 50 \leq 100 \leq 150$).

2.3.1   Time-of-flight spectrometer for detection of cluster ion

As already mentioned one advantage of a TOF spectrometer is that ions with different mass to charge ratios are detected simultaneously. However, if the temporal separation between successive pulses is shorter than the flight time of the slowest ionic fragment, then the fragment will appear in the mass spectra corresponding to the following radiation pulse. To simplify the analysis of mass spectra, the cluster ion spectrometer was designed in a very compact way. A distance of just 25 mm from the interaction region to the MCP [24] detector and an overall accelerating voltage of 3.4 kV results in a flight time of $\sim 0.987\,\mu s$ for a singly charged Xenon trimer Xe_3^+. This is shorter than the spacing of 1 μs between successive FEL pulses [8]. In Figure 2.12 a sketch of the cluster
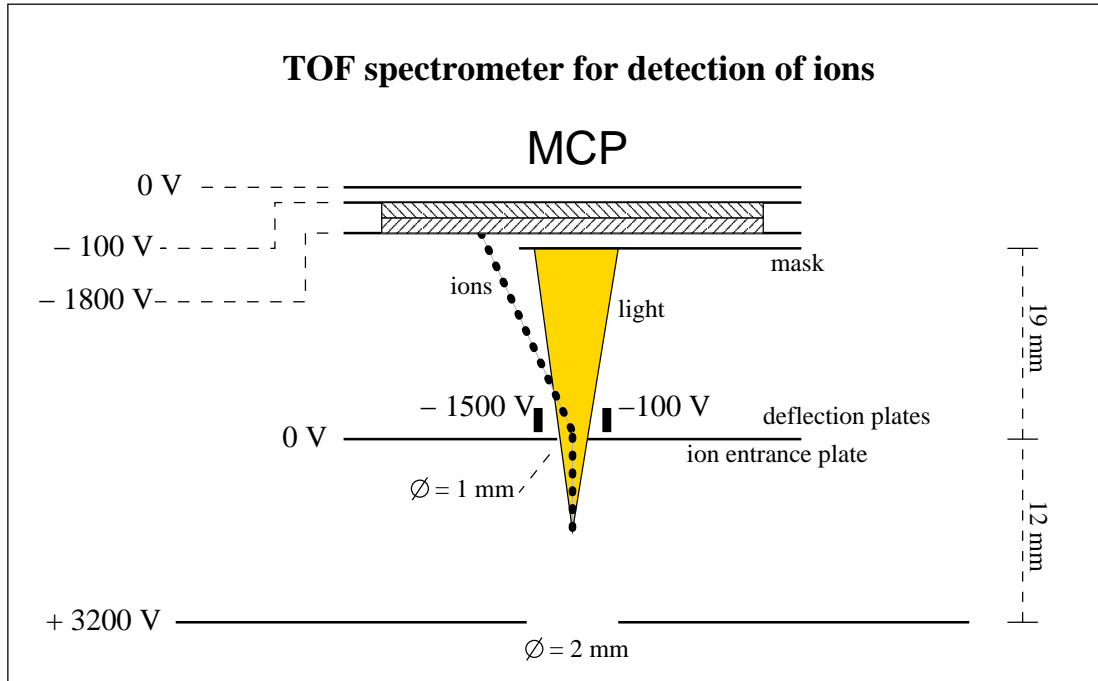
Figure 2.12: Sketch of the time-of-flight ion mass spectrometer. The positive ions are deflected onto the MCP detector. The fluorescence light emerging from the interaction zone is blocked away by a solid mask in front of the MCP.

ion TOF spectrometer is displayed. A special feature of the design is that the spectrometer is insensitive to fluorescence. This is because in the course of the excitation of a cluster radiative decay from electronically excited states can be expected. As a result, the luminescence signal may overlap with the TOF mass-spectrum. To prevent the luminescence from irradiating the MCP, a solid mask in front of the MCP blocks light produced in the interaction region. At the same time the ion optics guides ionic

---

[8]At that time it was not foreseeable, that the FEL could also be operated in single shot mode.

fragments onto the MCP. To achieve this a shaped stainless steel disk is mounted in front of the MCP. A slit in this mask, situated outside the fluorescence cone, allows ions to pass and hit the MCP. The ions are guided into the slit via two deflection plates. They create an additional electric field perpendicular to the pull-in voltage. In order to optimise ion trajectories for different electrode and voltage arrangements, simulations with the 3D ion optics simulation program SIMION 7.0 [25] were performed. Simulations were checked with test measurements at the experimental station CLULU. They confirmed that the detector is insensitive to luminescence. Furthermore, the mask does not reduce the count rate of ions initially at rest.

In Chapter 3.3 I will show that the interaction of intense VUV radiation from the FEL with clusters produces a variety of charge states, ejection energies and directions under which ionic fragments are ejected. Therefore further analysis of the experimental mass spectra requires a knowledge of the detector transmission T. The detector transmission $T(z, E_{ej}, E_{kin}, \Theta)$ is a function of ion charge state z, the ejection energy E_{ej} resulting from the Coulomb explosion of the cluster, the total kinetic energy E_{kin}[9] and the direction of ejection Θ. T can be separated in two contributions.

The first contribution is the *geometric acceptance g* which is mainly given by the actual sizes of the aperture and MCP and additionally the applied accelerating voltages. It was calculated by simulating the same number ($\sim$300,000) of trajectories for each ion charge state. The geometric acceptance of a specific charge state is the ratio of the trajectories reaching the MCP and the number of originally simulated trajectories. The relative geometric acceptance of charge state z is calculated by normalising the number of hits for z to the number of hits for Xe^+.

The second contribution is the *MCP detection efficiency ϵ*. In principle ϵ depends on both z and E_{kin}, but in our case the influence of E_{kin} dominates. Both contributions are discussed below. It is noteworthy that only relative values will be given, which allow to correct measured signal intensities of single charge states in one respective mass spectrum.

Geometric acceptance

The relative geometric acceptances for charge states Xe^+-Xe^{8+} and respective ejection energies E_{ej} were calculated using SIMION 7.0. A geometry file including the number, the geometry and the respective voltages of the electrodes for the ion spectrometer was created in SIMION. SIMION then simulated trajectories of ions in this geometry. To simulate a sufficient number of ions ($\sim$300,000) for each charge state the distribution of ions was generated externally by the custom-made program *Random Ion Generator*

---

[9]The total kinetic energy is the sum of the ejection energy and the kinetic energy due to the pull-in voltage: $E_{kin} = E_{ej} + z \cdot 3.4\,\text{keV}$

Random Ion Generator

uniform distribution of 314 000 ions on a sphere
convoluted with a gaussian energy distribution

azimuth distribution

elevation distribution

gaussian energy distributiom

SIMION 7.0
simulates ion trajectories

MCP

ion trajectories

mask

ion entrance plate

12 mm

19 mm

Results

6623 ions hit the MCP

angular acceptance

angular vs. ejection energy
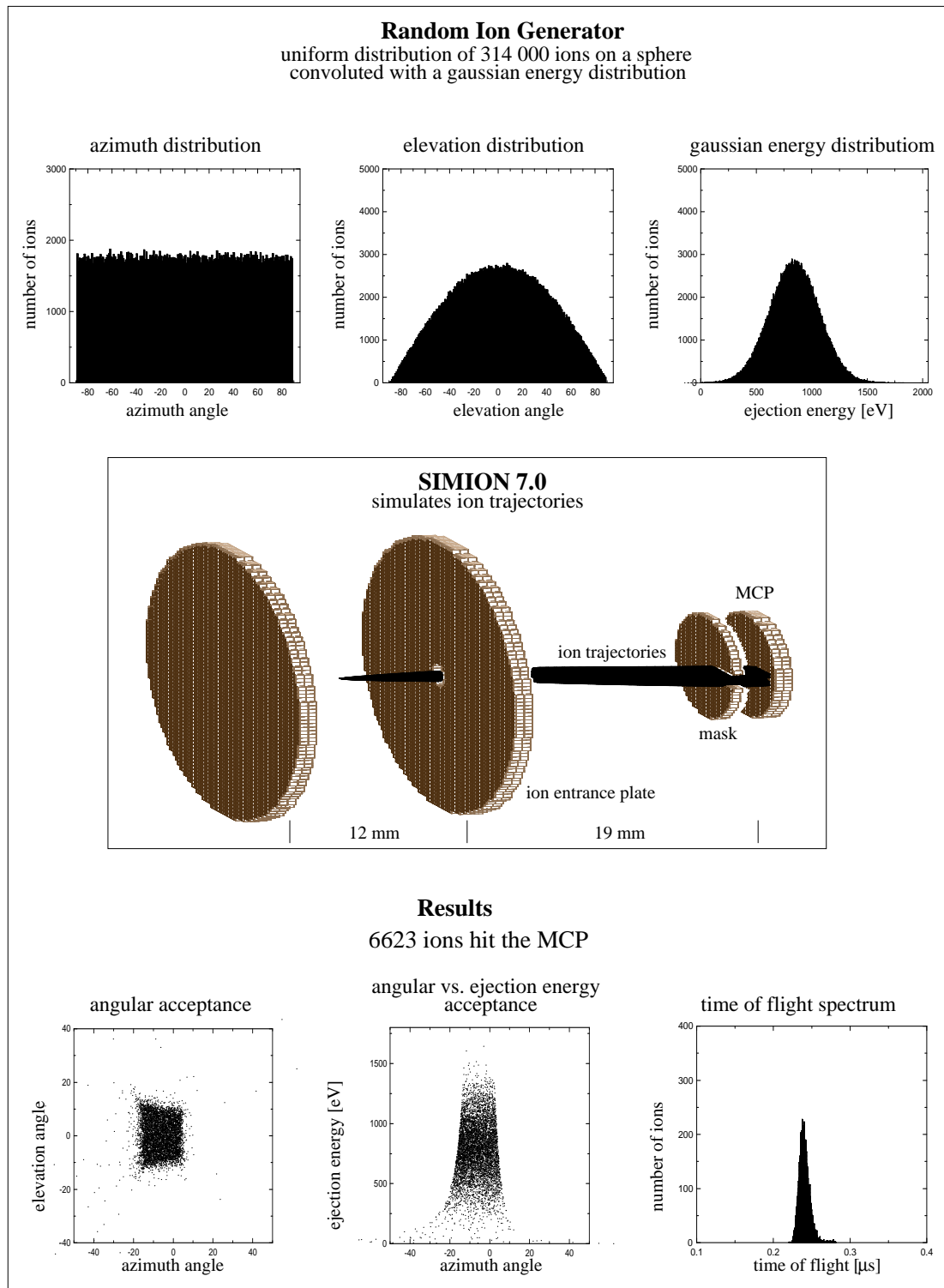acceptance

time of flight spectrum

Figure 2.13: Calculation of the relative geometric acceptance for Xe^{4+}.

(RIG) and then fed into SIMION. The source code of RIG is given in Appendix C.
The external program RIG generates a spherical, uniform random distribution in conjunction with a Gaussian distribution of E_{ej}. This means, that the speed directions of ions due to Coulomb explosion are distributed uniformly and randomly over a sphere. Mean value $\overline{E}_{ej}$ and the width (FHWM) of the kinetic energy distribution are determined beforehand by fitting the experimental mass spectra [10] and then they are used as input in RIG.

After the simulation is finished another custom-made program handles the output of SIMION 7.0. The program *Find Ions* extracts the number, the trajectories and input parameters of ions which have hit the detector. The source code is given in Appendix D.

As an example the procedure of calculating the relative geometric acceptance of Xe^{4+} is visualised in Figure 2.13. In the top part the uniform distribution on a hemisphere together with the Gaussian energy distribution is given. The reason for the unfamiliar look of the elevation distribution is the following. To simulate an isotropic distribution, the ions have to be distributed uniformly over the surface of the hemisphere. Going from the equator to one of the poles the area of bands between latitudes decreases with the cosine of the elevation angle, which is actually the shape of the elevation distribution in Figure 2.13. The reason as to why a whole sphere is not simulated immediately, results from computational restrictions.

In the middle part of Figure 2.13 the trajectories of the 6623 Xe^{4+} ions which hit the detector are displayed. With this result the relative acceptance of Xe^{4+} can now be calculated by normalising it to the result of Xe^{1+}, which is 21992 ions. The relative acceptance of Xe^{4+} is thus ~ 0.30.

At the bottom of Figure 2.13 a closer look at the geometric acceptance properties and the resulting time of flight spectrum is given. In the two graphs to the left each dot represents one ion.

MCP detection efficiency

A micro-channel plate (MCP) is an array of 10^4-10^7 miniature electron multipliers oriented parallel to one another [26]. An incoming ion hits the wall of one micro-channel, thereby releasing secondary electrons, which cause an electron avalanche by 'bumping' down the channel.

Secondary electrons may be produced by two different processes. The process of *potential emission* describes the release of secondary electrons due to neutralisation of the incoming ion. If the sum of the ionisation potentials up to the actual charge q=ze of the ion is greater than about twice the band gap of the channel wall material, then the potential energy released by the neutralisation of the ion can provide the energy necessary to free electrons from channel walls. *Kinetic emission* arises from the deposition

---

[10]As kind of a loop, kinetic energies are determined by comparison of experimental flight time and simulated flight time of ions initially at rest.

	Xe^+	Xe^{2+}	Xe^{3+}	Xe^{4+}	Xe^{5+}	Xe^{6+}	Xe^{7+}	Xe^{8+}
E_{ej}[eV]	93	261	526	844	1284	1729	2228	3102
E_{kin}[eV]	3493	7061	10726	14444	18284	22129	26028	30302
$\epsilon_{z,n} = \sqrt{\frac{E_{kin}(Xe^{z+})}{E_{kin}(Xe^+)}}$	1	1.422	1.753	2.034	2.289	2.518	2.713	2.946

Table 2.3: Normalised MCP detection probability $\epsilon_{z,n}$ for a specific set of Xenon ions. The respective individual detection efficiencies ϵ_z for different charge states are normalised to Xe^+.

of ion kinetic energy as the ion collides with the wall.

Despite the numerous published investigations [27, 28] up to now no complete quantitative picture of electron emission exists. However, it is generally accepted that there is a threshold velocity v_{th} below which no ion is detected. In a recent publication [29] v_{th} for Xe^+ was measured to be $2.71 \cdot 10^4 m/s$, which corresponds to 514 eV. Therefore *potential emission* dominates over the kinetic component at sufficiently low velocities, because it is energy independent. On the other hand, for ion velocities v much larger than v_{th} *kinetic emission* dominates and the electron yield γ depends linearly on the ion's velocity v or $\gamma \propto \sqrt{E_{kin}/m}$. In the present experiment the ion's velocity v resulting from the acceleration voltage of 3.4 kV in the spectrometer is sufficiently high to estimate the relative detection efficiency with the expression $\gamma \propto \sqrt{E_{kin}/m}$ for kinetic emission. The values for Xe^+-Xe^{8+} are given in Table 2.3. Please note that relative detection efficiencies may differ slightly as ejection energies change.

2.3.2 Bi-polar time-of-flight spectrometer for ion and electron detection

The name of this detector originates from its ability to detect either positive ions or negative electrons [30]. Thereby the output polarity is maintained at ground potential by electro-optically isolating the signal. This is realized by converting the electron avalanche from the MCP into photons in a scintillator and then reconverting them into electrons in a photo multiplier tube, whose signal output is kept at ground potential. Mass spectra of Xe ions resulting from an atomic beam and photoelectron spectra recorded with the bi-polar TOF are displayed in sections 3.2.3 and 3.4.2 . For the benefit of photoelectron time resolution a 150 mm long field-free drift tube is provided. The tube is made of μ-metal to reduce the influence of magnetic fields on the flight path of electrons. Additionally, the tube is kept at ground potential. To avoid surface charging in the tube as well as in the accelerating plate both are plated with gold. The settings of the bi-polar TOF for ion and electron detection are given in Table 2.4.
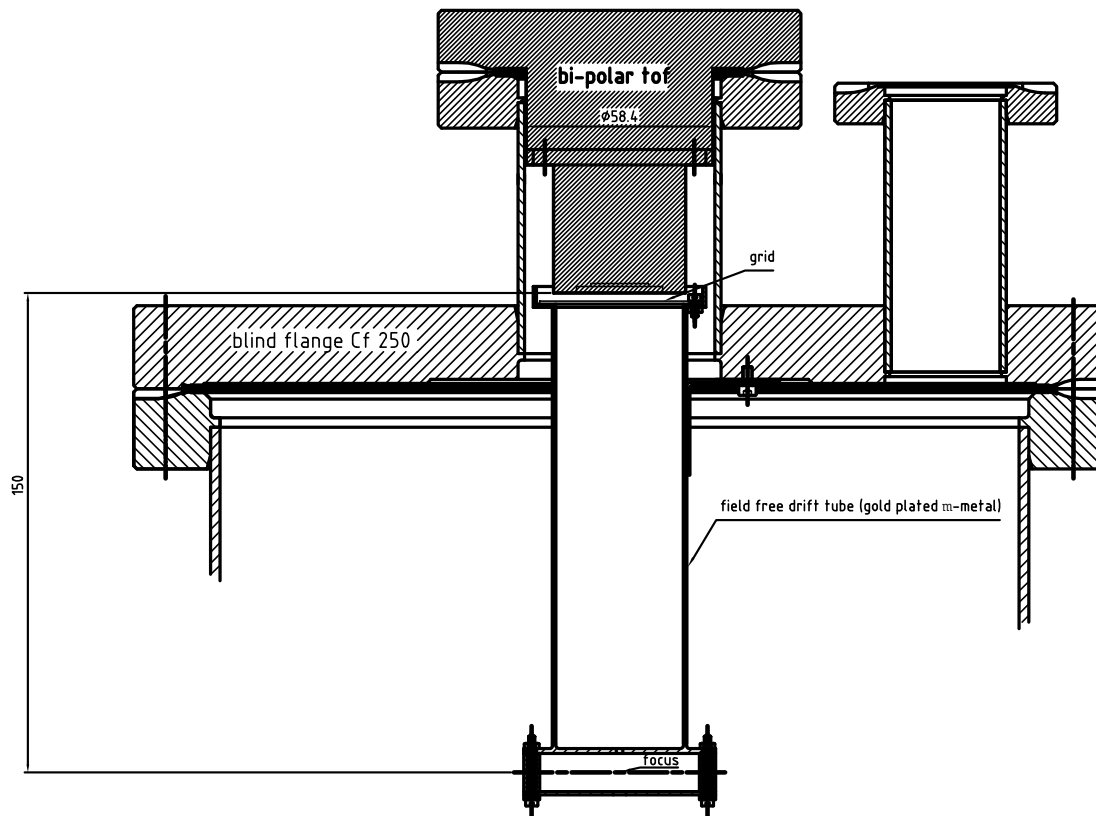
Figure 2.14: Longitudinal section of bi-polar TOF with flange body mounted on top of chamber.

applied voltages	ion detection	electron detection
acceleration plate (V)	+3200	5
drift tube	grounded	grounded
grid	grounded	grounded
MCP input (kV)	-1.8	grounded
MCP output (kV)	-0.8	+0.8
gain control (kV)	+1.2	+2.8
photo converter (kV)	-0.6	-0.6

Table 2.4: Settings of the bi-polar time-of-flight detector for ion and electron detection.

2.3.3 Fluorescence screen for determination of focal spot size

For the determination of the focal spot size of the FEL radiation a fluorescence screen (coating: ZnSCu) was integrated in the cluster ion TOF spectrometer described in section 2.3.1. The screen was located in the interaction region, beneath the ion entrance

aperture of the TOF spectrometer. The spot of the FEL radiation was recorded with a CCD camera [31] looking on the fluorescence screen and transferred to a monitor outside the accelerator tunnel. The maximum magnification of the camera was determined beforehand to be 200. Using the maximum magnification of the camera the minimum spot size on the monitor was 4 mm in diameter. Therefore the minimum spot size of the FEL radiation in the interaction region was 20 μm. Additionally, the fluorescence screen could be moved in and out of the radiation by remote control, thereby enabling frequent checks of the spot size.
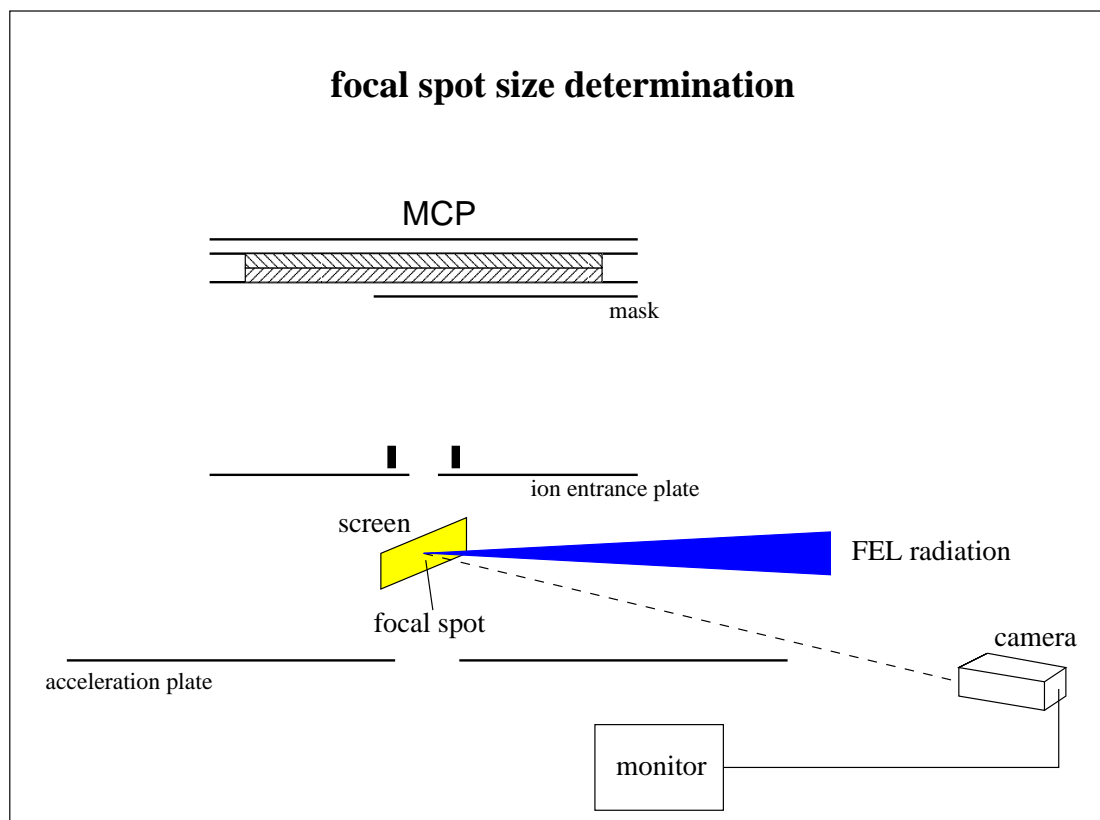
Figure 2.15: Schematic illustration of FEL focal spot-size determination. The fluorescence screen is located between acceleration and ion entrance plate of the TOF spectrometer depicted in Figure 2.12. A camera which is connected to the main vacuum chamber records the image of the FEL radiation spot.

At the beginning of the second experimental run the fluorescence screen was used to align the experimental set up and to check the spot size before the detectors were changed such that the bi-polar TOF spectrometer was implemented in the experimental set-up.

2.3.4 Data acquisition

All spectra were taken by recording 'directly' the detector output signal with a fast digital sampling oscilloscope. This measurement method can be referred to as analogue mode. The main advantage of this mode is that a multi-ion event (more than one ion hitting the MCP at the same time) which results in a higher output signal, is also recorded with its actual signal height[11]. $50\,\Omega$ impedance matching over the whole line from MCP to oscilloscope guaranteed unperturbed signals. Depending on the required temporal resolution sample rates of up to 8 giga samples per second, $8\,GS/s$, were used. Finally the data was transferred to a PC and stored on hard disk.
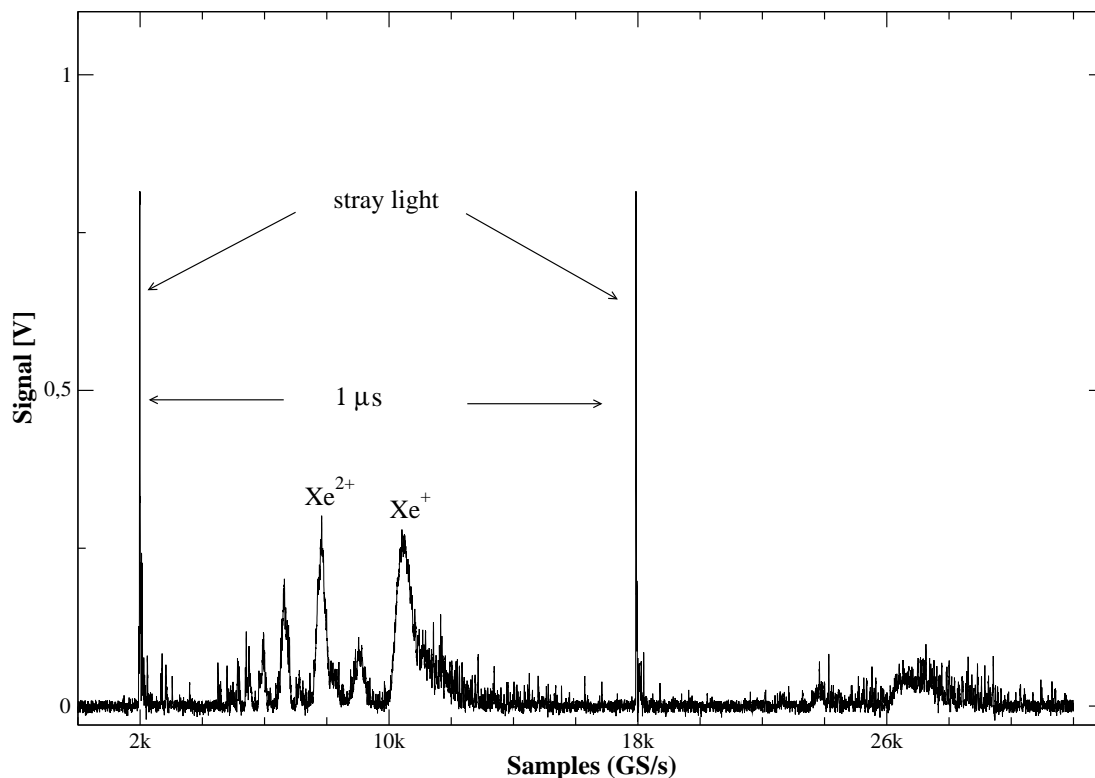
Figure 2.16: Unprocessed single-shot mass spectrum of Xenon clusters after irradiation with FEL light. Stray-light peaks are separated by $1\,\mu s$. TOF spectrum following second stray light peak is strongly degraded.

Figure 2.16 shows an unprocessed single-shot spectrum taken with the digital oscilloscope. The FEL was operated in the $1\,MHz$-mode, where bunch trains containing ten bunches each were produced with a repetition rate of $1\,Hz$ (section 2.1.4). The bunch separation was set to $1\,\mu s$. In Figure 2.16 a time range of $2\,\mu s$ was recorded, show-

---

[11]For example, in pulse counting mode every signal above a certain threshold is converted into a norm pulse no matter what the actual height of the signal was.

ing the ionisation products after irradiation with the first two radiation pulses of the bunch-train. At sample counts of about 2 k and 18 k the stray-light peaks of the pulses are visible. The stray-light peak was used in two ways. The intensity was used to specify the radiation intensity in the respective pulse and the rising flank of the stray-light peak marks the zero point of the time axis for each TOF spectrum. Compared to the time resolution of $\sim$1 ns of the MCP, the error due to the limited speed of light($<$0.1 ns) can be neglected.

In Figure 2.16 each stray-light peak is followed by a TOF spectrum of xenon ions. The stray-light peaks are equal in intensity. However, the two parts of the spectrum look quite different. Whereas in the first TOF spectrum several ion charge states are well resolved, the second spectrum reveals a degraded, broad feature. This behaviour has been seen in all recorded spectra. It shows that $1\,\mu$s is insufficiently short for the system to recover from the influence of the preceding pulse. As a consequence, only TOF spectra following the first radiation pulse were considered throughout the entire work.

Due to the stochastic nature of the SASE process, the peak power of the FEL radiation fluctuates strongly from pulse to pulse, see section 2.1.5. Therefore it is necessary to sort each single-shot according to its respective power density, whenever power density dependent processes are investigated. To facilitate this, every single TOF spectrum was stored separately on hard disk. Then, according to its stray-light intensity, each TOF spectrum was sorted with a routine. After sorting, only those spectra with a comparable stray-light intensity were averaged.

Chapter 3

Results and Discussion

3.1 Introduction

The experimental results presented in the following sections are the outcome of two experimental runs at the VUV-FEL in the first phase of the Tesla Test Facility (TTF1). Due to the nature of TTF1 as a test facility, the time for user experiments was very much restricted. The main scientific interest in both experimental runs was the interaction of intense VUV laser radiation from the FEL with rare gas clusters. Measurements investigating the ionisation of rare gas atoms were mainly taken for comparison with clusters. Thus the description of atomic ionisation in section 3.2 is only phenomenological.

During the first set of experiments in October 2001 the ionisation of clusters and also atoms was studied using a compact time-of-flight (TOF) mass spectrometer, which was specially designed for the detection of cluster ions. It is described in section 2.3.1. In addition photoelectron spectra were also recorded, but it became obvious, that the collection system of the photoelectron spectrometer could not provide signals of sufficiently high quality necessary for data acquisition in an analogue mode, see section 2.3.4. As a consequence, a new TOF spectrometer, the bi-polar TOF spectrometer described in section 2.3.2, using a commercial MCP with impedance matched output was designed. Additionally, the bi-polar TOF spectrometer was capable of detecting either negatively or positively charged ionisation products. This spectrometer was used to study photoelectrons as well as ions resulting from the ionisation of clusters and atoms during the second set of experiments in March 2002.

The experimental results are reproduceable and conclusive within each of the two separate experimental runs. A comparison of the TOF mass spectra after ionisation of clusters showed also, that the results concerning the ionisation of clusters are almost the same in both experimental runs. However, the TOF mass spectra recorded after the ionisation of atoms are significantly different. During the first run the cluster ion

optimised spectrometer detected only singly charged ions after the irradiation of a beam of Xe atoms. This can be seen in the bottom trace in Figure 3.8. The absence of higher charge states differs clearly from the detection of charge states up to Xe^{6+} with the bi-polar TOF spectrometer during the second run, see Figure 3.3.

The difference between the two experimental runs might be attributed to three different contributions. First, the MCP detectors used in the two different TOF spectrometers differ significantly in sensitivity. This observation is discussed in section 3.4.3.

Second, the detector transmission T of the two spectrometers is different. For example, it was observed, that the transmission T in the cluster ion optimised spectrometer was strongly enhanced for ions with a low kinetic energy ($< 1\,\mathrm{eV}$) compared to ions initially 'at rest', which arise after ionisation of atoms, see Appendix B.

Finally, uncertainties also come from the novelty of experiments at a light-source like the VUV-FEL. Constant improvements in the diagnostics of the FEL radiation like the installation of an online pulse energy monitor, briefly described in section 2.1.5, lead to uncertainties as to what extent measurements of the pulse energy are equivalent in both experimental runs. Additionally, properties like the orbit of the FEL radiation or the duration of the FEL radiation pulses, which can be best determined by spectral measurements with a monochromator which was situated in a different experimental branch (see section 2.1.6), could not be measured in parallel with the experiment, but were observed to change during one experimental shift of 8 hours [10].

The main part of this work is the study of VUV-light/cluster interaction. The TOF mass spectra resulting from the ionisation of clusters, for which the experimental results remained the same in both experimental runs, were then decided to be taken from the first run. The cluster ion spectrometer used in the first run was designed to fit the Wiley-McLaren conditions for time-of-flight focusing [32]. Different ion charge states are well separated in the TOF mass spectra and therefore the analysis is facilitated. TOF mass spectra after ionisation of Xe clusters are presented in section 3.3.4.

TOF mass spectra recorded after the irradiation of atomic beams are taken from the second experimental run, because the bi-polar spectrometer has a larger sensitivity. Additionally, the improved online detection of the FEL radiation pulse energy was regarded as advantageous. TOF mass spectra displaying the ionisation products after irradiation of beams of Xe and Ar atoms are presented in section 3.2.3.

The photoelectron spectra given in section 3.4.2 were also recorded during the second experimental run. Only after the new impedance matched signal output of the bi-polar spectrometer was installed at the beginning of the second experimental run, photoelectron spectra could be recorded.

In summary, the availability of the two different detectors allowed me to obtain ion mass spectra of atoms and clusters as well as photoelectron spectra. They provide the basis for first results of matter interactions with intense VUV-light.

3.2 Rare gas atoms

3.2.1 Introduction

The interaction of optical laser radiation with atoms has been investigated for more than two decades. Rare gas atoms serve as a model system in this context. Recent experiments using optical lasers address complex problems such as direct double ionisation of rare gas atoms [33], the generation of attosecond pulses [34] and their initial applications [35] and the improvement of coherent light-sources in the extreme-ultraviolet spectral regime by the optimisation of high harmonics generation in atomic gases [36]. The basic ionisation mechanisms have been studied in great detail both experimentally and theoretically since the 1980's [37]. However, these experiments were limited to the optical and near-ultraviolet (UV) spectral regime. At shorter wavelengths in the vacuum ultraviolet (VUV) region, where the energy of single photons becomes large enough to ionise rare gas atoms, light-sources capable of delivering intense radiation were not available. Consequently, the interaction of intense VUV radiation with matter remained unexplored. With the VUV-FEL it is therefore, for the first time, possible to extend investigations of the basic ionisation mechanisms of rare gas atoms into the VUV regime. The experiments presented here are a first attempt to obtain results for short wavelengths and can serve as a starting point for detailed future work.

Experiments in the optical and UV spectral regime showed that as the power density of the laser approaches $10^{13} - 10^{14}\,\mathrm{W/cm^2}$ multiphoton ionisation becomes important. As the power density is further increased the mechanism changes and the perturbation of the atomic potential gets so strong, that the electric field strength of the laser exceeds that of the Coulomb potential between the outermost electron and the ionic core (field ionisation process). However, this description needs a fast ionisation process with respect to the radiation frequency to assume the effective combined atomic-laser potential as a static one (adiabatic approximation). But if the radiation frequency is too high, field ionisation of the electron is hindered and the ionisation proceeds via multiphoton ionisation. This is the case for power densities around $10^{14}\,\mathrm{W/cm^2}$, where in the infrared (IR) regime ionisation of xenon atoms is due field processes, but at higher frequencies in the optical and UV regime the atoms are ionised by multiphoton absorption. So the type of ionisation depends in principle on both the laser electric field strength and the frequency of the radiation. The present experiment extends investigations to a formerly not accessible high radiation frequency. Therefore it provides the possibility to compare the experimental findings with results found in the UV regime and to see if the relevant models also apply at higher photon energies. A particularly interesting aspect was the comparison between Xe and Ar atoms: The ionisation energy of Xe is lower than the FEL photon energy, but for Ar the ionisation energy is higher than the photon energy. A further aim was to compare the interaction of atoms with

that of clusters, which is discussed in section 3.3.

In the following section first multiphoton processes are briefly introduced. This is followed by the presentation of time-of-flight mass spectra of atomic xenon and argon beams after irradiation with FEL radiation at 98 nm. Then the underlying ionisation process is analysed and discussed in the context of previous experimental and theoretical work in the UV spectral range.

3.2.2 Multiphoton processes in intense laser fields

In the literature the ionisation of a system is called nonlinear, when the condition $\hbar\omega < I_p$ is fulfilled, where I_p is the ionisation potential of the outermost electron in the system and $\hbar\omega$ is the photon energy [37]. The processes which lead to the ionisation in intense laser fields are separated into two regimes. In the *multiphoton ionisation* (MPI) regime the atom (or ion) is ionised by absorption of several (more than one) photons. In the *field ionisation* regime the electron can escape, because the atomic potential is strongly lowered by the electric field of the laser and the electron can tunnel through the remaining small barrier (*tunnel ionisation*). Furthermore, if the electric field strength E_0 of the laser exceeds the atomic field strength, then the electron is no longer bound and escapes over the barrier (*above barrier ionisation*), see Figure 3.1.

The two regimes can be roughly separated with the Keldysh parameter γ [38]. The parameter is deduced from the assumption that a tunnelling electron needs the time T_t to traverse the barrier width $l = I_p/eE$, where e is the electron charge and E is the electric field strength of the laser. Tunnel ionisation is possible if the tunnelling time T_t is much smaller than the cycle duration T_l of the laser. On the other hand, if T_l is much smaller, the electric field of the laser reverses its sign before the electron can jump through the barrier and tunnelling is forbidden. If the Keldysh parameter is expressed by $\gamma = T_t/T_l = \omega/\omega_t$, two regimes can be distinguished: for $\gamma \ll 1$ field ionisation governs the ionisation process and in the opposite case $\gamma \gg 1$ field ionisation is prohibited and the ionisation is due to MPI.[1] Using for the tunnelling frequency $\omega_t = eE_0/\sqrt{2m_e I_p}$ we get readily the expression:

$$\gamma = \sqrt{\frac{I_p}{2\frac{e^2 E_0^2}{4m_e\omega^2}}} = \sqrt{\frac{I_p}{2E_p}} \tag{3.1}$$

where ω is the laser frequency and the ponderomotive energy $E_p = e^2 E_0^2/4m_e\omega^2$ is introduced[2]. From equation (3.1) it can be estimated immediately that field ionisation dominates for intense and low frequency (infrared) laser fields, whereas for optical lasers

---

[1]Provided the laser intensity is high enough. At very low intensities no ionisation at all takes place.

[2]In the electric field of the laser an electron gains the kinetic energy $E_{kin}(t) = (e^2 E_0^2/2m\omega^2)sin^2(\omega t)$. After averaging over a few oscillation periods the average kinetic energy of an electron in a laser field becomes $\bar{E}_{kin} = e^2 E_0^2/4m_e\omega^2$, which is called the ponderomotive energy E_p.

and lower power densities ionisation is mainly due to MPI. As an example γ is calculated for the ionisation of Ar^+. With an ionisation potential of $I_p = 15.6\,\text{eV}$, a power density of $P_{FEL} = 10^{13}\,\text{W/cm}^2$ ($\hat{=}8.7 \times 10^9\,\text{V/m}$) and laser frequency $\omega_{FEL} = 1.9 \times 10^{16}\,\text{Hz}$ the Keldysh parameter becomes $\gamma \sim 29 \gg 1$. Because this is the lowest possible I_p in our case (Xe^+ is produced by single photon absorption), it can be expected that ionisation processes are due to MPI. In the following I want to start with a brief description of *field ionisation*.

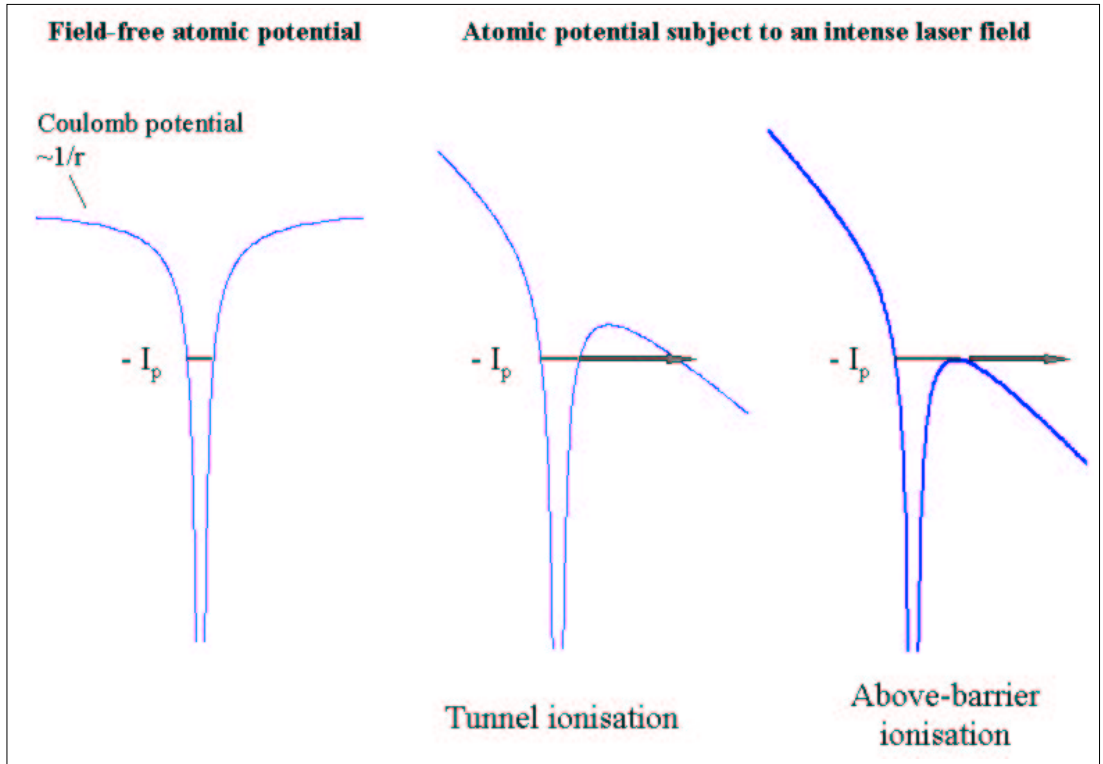**Field ionisation ($\gamma \ll 1$)**

Figure 3.1: Field ionisation processes in intense laser fields. If the ionisation process is much faster than the cycle duration of the laser, then the laser electric field can be assumed static.

In Figure 3.1 a schematic illustration of field ionisation processes is given. With no external laser field the atomic potential shows the usual $\sim 1/r$ dependence. If the incident laser field is strong enough and the frequency low enough then, within a quasi-static approximation, the field distorts the atomic potential to such an extent that a barrier is formed through which the electron can tunnel. Generally, tunnel ionisation happens at power densities from $10^{14} - 10^{15}\,\text{W/cm}^2$ [39]. As the field strength is increased the barrier becomes smaller and lower until the ground state is no longer bound. Usually above barrier ionisation dominates for power densities $> 10^{15}\,\text{W/cm}^2$. Values of the

electric field strength at which above barrier ionisation occurs for Xe atoms and ions in the adiabatic approximation are given in Table 3.2.
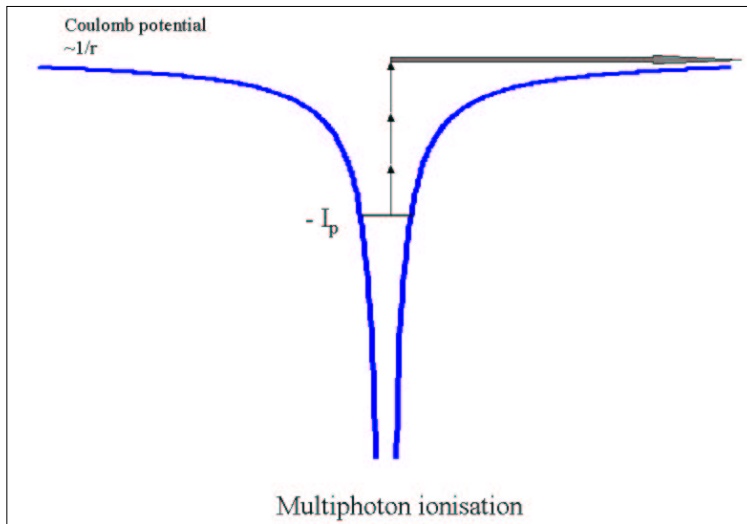
Multiphoton ionisation ($\gamma \gg 1$)

Figure 3.2: Schematic illustration the multi-photon ionisation(MPI) process. Photons are indicated by arrows.

Multiphoton ionisation (MPI) is the multiphoton transition from a bound state to a free (continuum) state [39]. In Figure 3.2 a schematic illustration of MPI by absorption of three photons is displayed. In lowest-order perturbation theory the n-photon ionisation rate is given by

$$\Gamma_n = \sigma_n P^n \tag{3.2}$$

where n is the minimum number of photons needed for ionisation, σ_n is the generalised cross section and P is the incident laser power density. MPI is most dominant for power densities $< 10^{14}$ W/cm^2. From equation (3.2) it is also evident, that at a low power density the ionisation rate is very low.

In principle two different processes of MPI can be distinguished [37]. The first is called *stepwise ionisation* where electrons are detached sequentially. If the case of a doubly charged ion A^{2+} is considered, then the first electron is detached from the atom A and subsequently the second electron is removed from the singly charged ion A^+. This type of process can be described by the reaction

$$A + n_1 \cdot \hbar\omega \quad \to \quad A^+ + e^- \tag{3.3}$$

$$A^+ + n_2 \cdot \hbar\omega \quad \to \quad A^{2+} + e^- \tag{3.4}$$
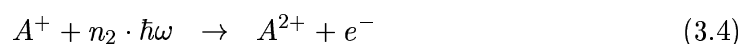
where n_1 and n_2 denote the number of photons needed for the respective transition. According to equation (3.3) the ion count rate of, for example, A^+ should follow in a *log*Γ-*logP* diagram ideally a straight line with the slope n_1 up to the saturation power density P_s (all neutral A ionised) and then remain constant. However, in actual experiments two additional effects cause a deviation from this behaviour: 1) A^+ ions originate not only from the interaction region of maximum power density P_{max}, but also from the peripheries of the spatial laser profile where $P < P_{max}$. This effect causes a further increase in the ion count rate above P_s. The slope of this increase is smaller than n_1, thus providing an indication of the value of P_s [40]. 2) As the power density increases the ions A^+ are eventually further ionised and eject a second electron. This effect happens even before P_s is reached and decreases the ionisation count rate of A^+. But in most experiments the first effect leads to a small overall increase [40].

This behaviour is observed and discussed below in sections 3.2.3 and 3.2.4. Needless to say, that stepwise MPI is not restricted to the production of doubly charged ions.

The process in which the doubly charged ion A^{2+} is produced due to a simultaneous detachment of two electrons is called *direct MPI*. It corresponds to the reaction

$$A + n_3 \cdot \hbar\omega \quad \rightarrow \quad A^{2+} + 2e^- \tag{3.5}$$
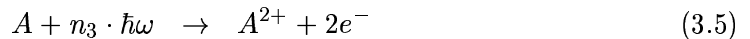
where n_3 photons are needed for the direct transition. Obviously the number of photons n_2 needed to remove the second electron in the stepwise process is lower than the number n_3 in direct MPI. Recalling equation (3.2) we note that stepwise and direct MPI can be distinguished by analysing the slope of $\Gamma_n(P)$ in a log-log diagram. This is done in section 3.2.4 for $Xe^{3+} - Xe^{5+}$ and Ar^{2+}.

3.2.3 Ionisation with VUV light

The power density dependence of the ion count rate as given in equation (3.2) makes TOF mass spectra a valid means for investigation of the underlying ionisation process. The mass spectra shown in Figures 3.3 and 3.4 were taken in the *second set of experiments* with the bi-polar TOF mass spectrometer described in section 2.3.2. The ionisation products of Xe and Ar atomic beams after irradiation with 98 nm radiation are given in each figure for three different power densities of the FEL. One main difference in the context of photon energy is, that the photon energy of 12.65 eV exceeds the ionisation potential $I_p \sim 12.1$ eV of Xe atoms, but is well below the first I_p of Ar atoms at 15.6 eV. Therefore the first electron in xenon can be detached by absorption of a single photon, whereas in argon a two-photon absorption is needed.

As can be expected from the large single photon absorption cross section of ~ 40 Mbarn [41] the signal from Xe^+ was already saturated at $< 10^{12}$ W/cm^2. [3] In the lower trace

---

[3]At 10^{12} W/cm^2 and a pulse duration of 100 fs the number of FEL-photons (12.65 eV) per cm^2 is about 5×10^{16} in one radiation pulse. This means, that two photons fall into the cross section of
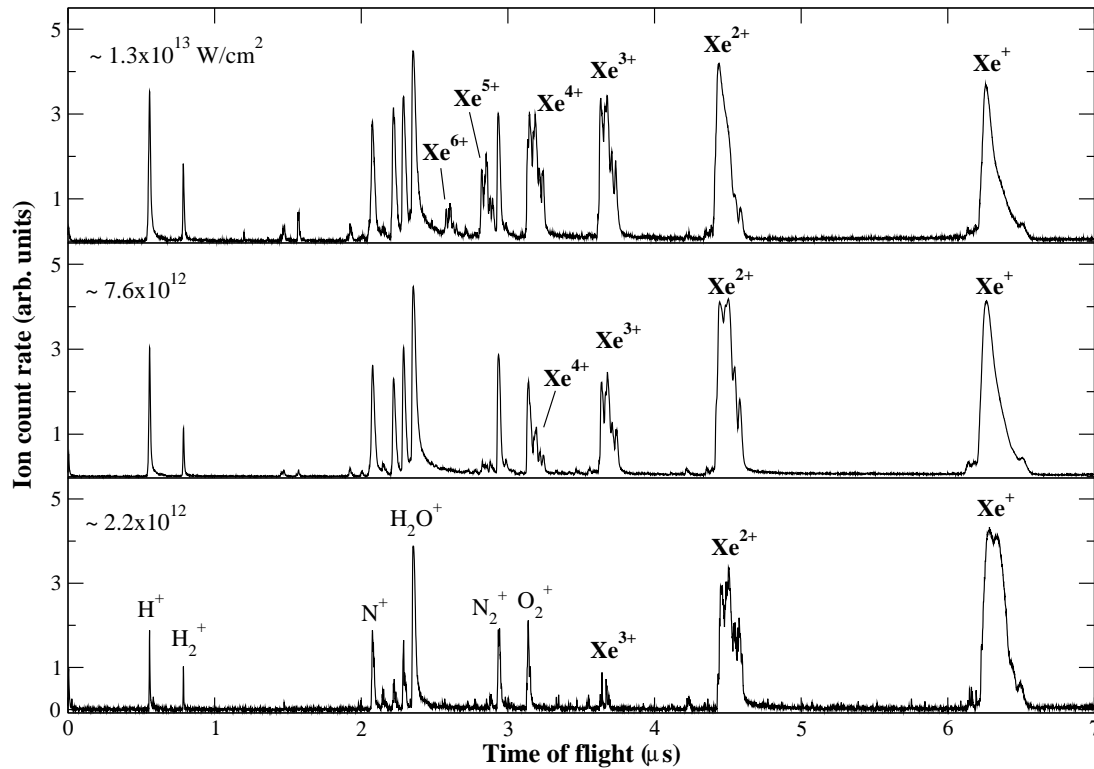
Figure 3.3: Ionic products after irradiation of an atomic xenon beam for three different power densities of the FEL. Power densities are given next to each trace. Charge state and count rate of atomic ions strongly depend on P_{FEL}, which illustrates the nonlinear nature of the ionisation process.

in Figure 3.3 the atomic ions Xe^+-Xe^{3+} can be seen and additional lines due to residual gases. Whereas Xe^{2+} and Xe^{3+} show a splitting due to the different isotopes, the shape of Xe^+ is unresolved, which indicates saturation of the MCP detector. Increasing the power density leads to the same behaviour for Xe^{2+}. This can be seen by following Xe^{2+} from the lower to top trace (power densities given next to each trace). Simultaneously the ion count rate of Xe^{3+} increases strongly and higher charge states arise. At the highest power density of $\sim 1.3 \times 10^{13}$ W/cm^2 all charge states up to Xe^{6+} are present.

The mass spectra of Ar atoms in Figure 3.4 look not that much different. The corresponding charge states appear at somewhat higher power densities. At $\sim 2 \times 10^{12}$ W/cm^2 Ar^{3+} is not yet detected and at the highest power density of $\sim 1 \times 10^{13}$ W/cm^2 (slightly lower than with xenon) the ion count rate of Ar^{4+} is very low. What the mass spectra of both elements have in common is the strong dependence on the power density. This behaviour points clearly to the nonlinear nature of the inter-

---

a neutral Xe atom (40 Mbarn) during one FEL radiation pulse. Consequently, all Xe atoms in the interaction zone are ionised.
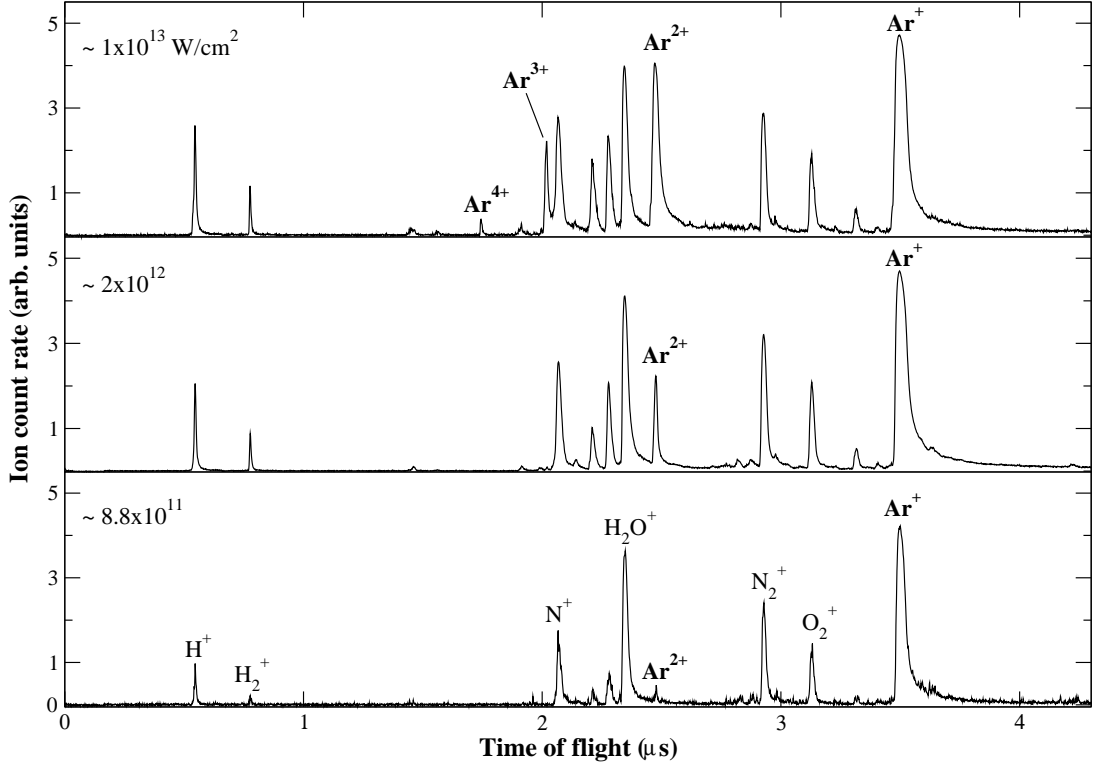
Figure 3.4: Ionic products after irradiation of an atomic argon beam for three different power densities of the FEL. Compared with Xe atoms, equivalent charge states appear at higher P_{FEL}, but the nonlinear nature of the ionisation process is also obvious.

action with the intense FEL radiation at 98 nm. The question as to which underlying processes are responsible for this interaction is addressed in the following section.

3.2.4 Ionisation mechanism

From the mass spectra presented in the previous section it is clear, that the ionisation process is highly nonlinear. From equation (3.2) it follows that the slope of $\Gamma_n(P)$ in double logarithmic scale reveals the order n of the nonlinear ionisation process. In Figure 3.5 ion count rates of Ar^{2+} and Xe^{3+}-Xe^{5+} are plotted as a function of power density. Linear fits are indicated as straight lines. The deviation of Xe^{3+} and Xe^{4+} from the linear fits at higher power densities can be attributed to the saturation effect that all parent ions, Xe^{2+} and Xe^{3+} respectively, in the interaction region are ionised [4]. The saturation power densities of Xe^{3+} and Xe^{4+} are estimated as $P_s(Xe^{3+}) \sim 5 \pm 2.8 \times 10^{12}\,\text{W/cm}^2$ and $P_s(Xe^{4+}) \sim 9 \pm 4.8 \times 10^{12}\,\text{W/cm}^2$ respec-

---

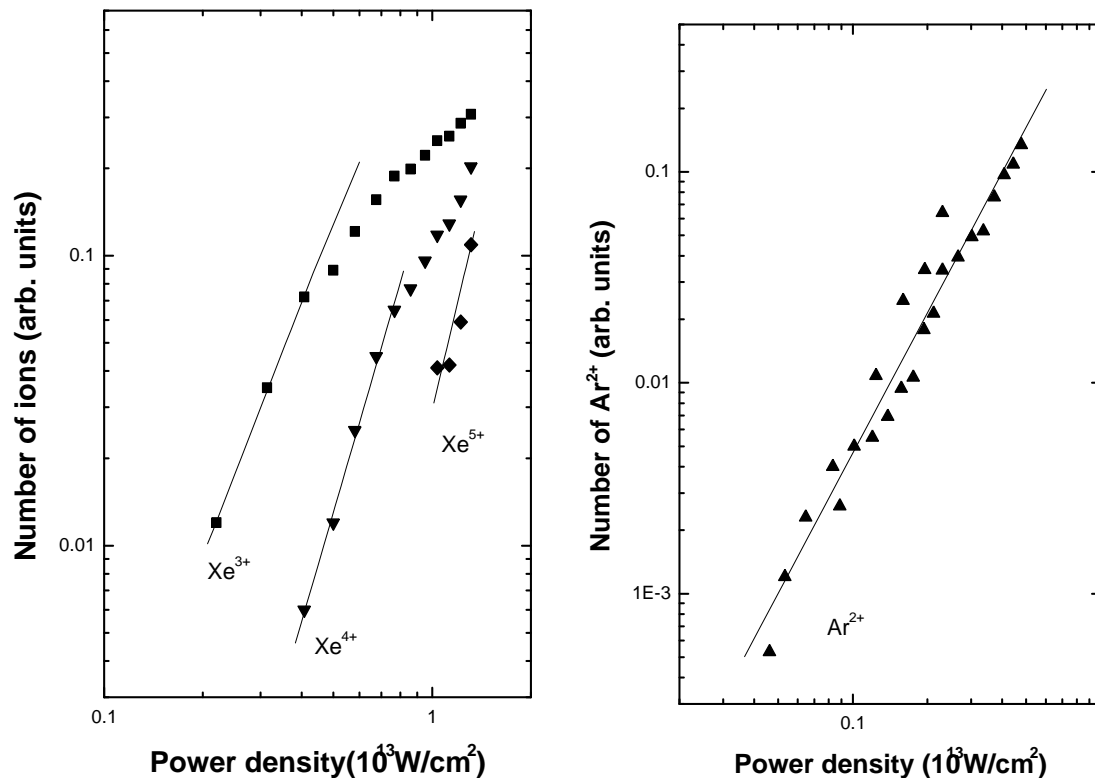[4]See explanation of saturation power density in section 3.2.2

Figure 3.5: Ion production rates of Xe and Ar atoms as a function of power density of the FEL at 98 nm. *left graph*: Ionisation count rate of Xe^{3+}, Xe^{4+} and Xe^{5+}. Slopes of linear fits are 2.9, 3.9 and 4.8 respectively. Deviations of Xe^{3+} and Xe^{4+} at higher count rates are due to saturation effects. *right graph*: Ionisation count rate of Ar^{2+} and linear fit (solid line) of the data. The slope of the linear fit is ~2.3 and reveals the order of the multiphoton process.

tively [5]. The saturation of Xe^{3+} coincides with the appearance Xe^{4+}, which is a first indication of stepwise MPI [40]. Further indications for stepwise MPI result from the following analysis of the slopes of the linear fits. The slopes of the respective linear fits are listed in Table 3.1 and compared with the minimum number of 12.65 eV photons needed for *direct* or *stepwise MPI*. For Xe^{3+}-Xe^{5+} derived slopes of linear fits agree well with the number of photons n needed for stepwise ionisation. For example, it needs 32.1 eV to detach the outermost electron from Xe^{2+}. Therefore Xe^{2+} has to absorb three 12.65 eV photons and the reaction becomes $Xe^{2+} + 3 \cdot \hbar\omega_{FEL} \rightarrow Xe^{3+} + e^-$. This is in good agreement with the value of 2.9 derived from the linear fit. On the other hand, direct MPI can be ruled out, because the neutral atom has to absorb six FEL-photons for a simultaneous detachment of three electrons. A schematic illustra-

---

[5]The error in P_s results from standard error propagation of the errors related to the focal spot size $r = 10 \pm 1\,\mu m$ and the radiation pulse length $\tau_{rad} = 100 \pm 50\,fs$ [42].

	direct		stepwise		measured
	I_p [eV]	n	I_p [eV]	n	n
Xe^{2+}	32.1	3	21.0	2	-
Xe^{3+}	65.2	6	32.1	3	2.9
Xe^{4+}	111.9	9	46.7	4	3.9
Xe^{5+}	171.6	14	59.7	5	4.8
Ar^{2+}	43	4	27	3	2.3

Table 3.1: Comparison of measured and theoretical nonlinearities of MPI process. I_p denotes the binding energies of ion charge state z when ionised from neutral atom (direct) or parent ion (z-1) (stepwise). n is the minimum number of photons needed for respective MPI, which gives the value of nonlinearity. The measured values of n are the slopes of linear fits in Figure 3.5.
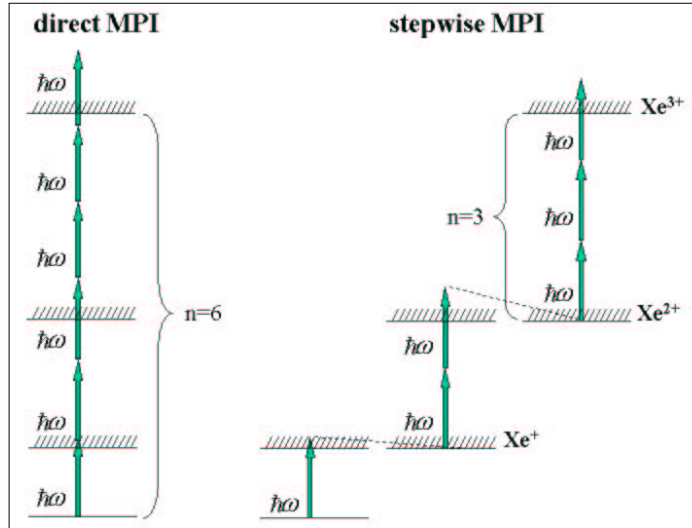
Figure 3.6: Schematic illustration of direct and stepwise MPI for the ionisation of Xe^{3+}. The derived slope of 2.9 indicates that the stepwise process accounts for production of Xe^{3+}. Spin orbit coupling is not included.

tion of the two MPI processes for production of Xe^{3+} is given in Figure 3.6. Resonant processes are not taken into account.

In the case of Ar^{2+} stepwise MPI is also more probable than the direct process. Even though the measured slope of 2.3 is lower than the theoretical limit of three photons for stepwise MPI, it is more likely than direct MPI, which requires four photons.

3.2.5 Discussion

The experimental findings show similar results as previous experiments with lasers in the optical and near ultraviolet range. Especially the mass spectra in [43] after irradiating an atomic beam of Xe atoms with 193 nm radiation, at a somewhat higher power density ($\sim 10^{14}\,\mathrm{W/cm^2}$) as in my work, reveal a similarity. The highest charge state observed is also Xe^{6+} and the relative intensities of different charge states is about the same as in this work. Lambropoulos et al. [40] found in their theoretical considerations basing on perturbation theory and using generalised cross sections, that the production of Xe^{2+}-Xe^{5+} (Xe^{6+} was not included) lies in the range 10^{13}-$10^{14}\,\mathrm{W/cm^2}$ for 193 nm. The results for a Gaussian laser pulse of 100 fs duration are given in Figure 3.7. This is essentially the same range as observed in the FEL-experiment at $\sim$98 nm. In the FEL-experiment charge states appear and saturate at about 10 times lower power densities compared to the calculations for 193 nm given in Figure 3.7. For example Xe^{3+} saturates in Figure 3.7 at a power density of about $5 \times 10^{13}\,\mathrm{W/cm^2}$, which is an order of magnitude higher than the saturation power density measured in the FEL-experiment.
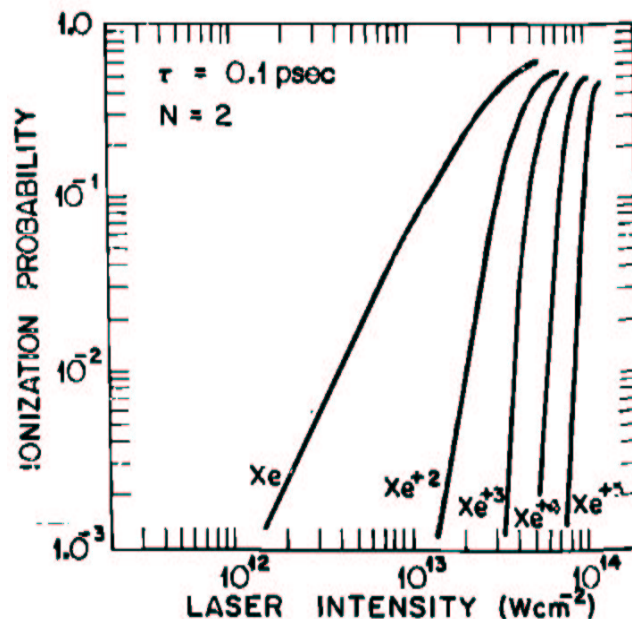
Figure 3.7: Theoretical calculations of ionic population as a function of peak power of Gaussian pulses after irradiation of Xe atoms at 193 nm wavelength. The laser pulse duration was set to 100 fs. The figure is taken from [40].

The production of high ionic charge states at lower power densities in the FEL-experiment might be attributed to the difference of the photon energies. At 193 nm a two-photon absorption is needed to produce Xe^+, whereas at 98 nm the much more efficient single photon absorption is sufficient and of course, for all following MPI processes the order

of nonlinearity in the FEL-experiment is always smaller than in the calculations. Additionally, it has to be mentioned that the authors of [40] showed that the ionisation is shifted to somewhat smaller power densities, when using a faster rising laser pulse than the purely Gaussian pulse shape used for Figure 3.7. But the shape of the FEL-pulses could not be measured and therefore no conclusion can be drawn from that.

Concerning the type of MPI process, Lambropoulos et al. [40] point out the much higher probability of a sequence of single electron MPI compared to the direct MPI process. The lower nonlinearities n in Table 3.1 of sequential processes as compared to direct processes, whose nonlinearities are about the sum of the sequential processes, are the reason for this behaviour. As a result, in the range 10^{13}- 10^{14} W/cm^2 all MPI processes are due to *stepwise MPI.*

These results further support the interpretation, that at 98 nm and at power densities of about 10^{13} W/cm^2 the MPI of Xe and Ar atoms is stepwise in nature.

In summary, the ionisation of rare gas atoms in intense VUV light is due to stepwise MPI. This result is expected from previous experiments in the UV spectral regime. The production of multiple charged ions starts at about 10 times lower power densities in the FEL-experiment compared with experiments at longer wavelengths. This trend agrees with what one expects intuitively and is supported by calculations made for the multiple ionisation of He atoms [44].

3.3 Xenon clusters

3.3.1 Introduction

Atomic clusters are a conglomerate made of a few (>2) up to many ($\sim 10^6$) atoms and bridge the gap between the molecular and the bulk solid state of matter. In a sense rare gases form the most simple clusters, because the constituting atoms are only weakly bonded by undirected van der Waals forces. Cluster beams provide the additional advantage that the overall sample is very dilute while the individual clusters reveal nearly solid density. Therefore the interest in these systems has been extensive since their first observation [45]. The interaction of light with clusters can be separated in two regimes, depending on the power density or the electric field strength of the light. For weak fields, which are only a small perturbation compared to the atomic field, the interaction is governed by single photon absorption processes. In the high power density regime the interaction becomes highly nonlinear, which includes multiphoton absorption or even field ionisation processes, when the light electric field is no longer small compared to the atomic field. Whereas in the weak field regime the whole spectral range of light is available, the high power density regime was in the past restricted to the optical spectral range. The extension of the high power density regime into the VUV and soft X-ray therefore opens the possibility to enlarge the understanding of the fundamental interaction of light with condensed matter.
In the following, first the interaction of 'weak' light sources in the VUV regime with clusters is briefly discussed. Then the interaction in strong optical fields is introduced in section 3.3.3. In section 3.3.4 time-of-flight (TOF) mass spectra after irradiation of Xe clusters are presented. This is followed by an analysis of the expansion mechanism and the responsible process in section 3.3.5. Section 3.3.6 is then dedicated to a description of the ionisation and absorption process, thereby checking the applicability of classical models to account for the experimental results. Finally, a discussion in section 3.3.7 closes the chapter.

3.3.2 Interaction of rare gas clusters with VUV light

Once the photon energy exceeds the ionisation potential, the cluster is ionised by single photon absorption. In the VUV spectral range up to 30 eV the photon energy is only capable of single-ionising the cluster. After the ionisation the remaining positive charge tends to delocalise due to interatomic hopping. On the other hand, the charge induces a polarisation of the surrounding atoms, which hinders the delocalisation. In a recent experiment [46] the luminescence emitted in the course of electronic relaxation of singly ionised Xe_N^+ clusters was used to investigate the charge localisation process.
It is interesting to examine the photon absorption probability of a Xe cluster when using

light of 100 nm wavelength from a conventional VUV light source. A typical VUV beam-line at a synchrotron radiation source like beam-line I at HASYLAB at DESY delivers 2×10^5 photons/pulse at a repetition rate of 5×10^6 Hz. At the cluster experiment CLULU [18] the minimum focal area is $1 \, \mathrm{mm}^2$, which gives 2×10^{11} photons/m^2 in one light pulse. Since the cross section of a Xe atom at 98 nm is about 40 Mbarn [41], the probability for an atom becomes to absorb a photon 8×10^{-10} during one light pulse. Therefore the probability of ionisation for a Xe_{2500} cluster is as low as 2×10^{-6}. This example shows, that the absorption of more than one photon by the same cluster can be completely neglected when using conventional VUV light sources. The situation changes dramatically when the VUV-FEL serves as light source. In addition to the enormous number of photons ($\sim 10^{12}$) in one light pulse, the high brilliance of the FEL allows a reduction of the focal spot size by a factor of 2500. As a result, the absorption probability of neutral Xe atoms in the cluster is increased by a factor of $\sim 10^{10}$, which leads to a high degree of ionisation as shown in section 3.3.4.

3.3.3 Clusters in a strong electric field

The invention of chirped pulse amplification in 1985 [47] permitted the construction of very intense lasers in the optical range with peak power densities of more than $10^{15} \, \mathrm{W/cm}^2$. At these power densities the electric field strength of the laser exceeds the atomic field strength, with which most valence electrons are bound to the nucleus. Experiments investigating the interaction of such intense radiation with rare gas clusters exhibited some remarkable results. Initial experiments at $10^{15} \, \mathrm{W/cm}^2$ showed the production of multiply charged ions and a disassembling of small argon clusters due to a *Coulomb explosion* [48]. Later experiments with 10 times higher power density revealed kinetic energies of up to 3 keV for electrons ejected from large clusters (>1000 atoms), which is about 30 times higher than the maximum kinetic energy resulting from irradiating an atomic beam [49]. The ions produced in this interaction exhibit unexpected high kinetic energies of up to 1 MeV, which was attributed to a different disassembling mechanism called *hydrodynamic expansion* [50].

The very high kinetic energy of the ionisation products in the laser-cluster interaction is a result of the *strong absorption* from the laser field by the cluster. In [50] each cluster was found to absorb a fair fraction of a nanojoule. Moreover an absorption efficiency of nearly 100% was observed over a propagation distance of a few millimetres through a cluster beam [51].

The observation of a *high X-ray yield* from rare gas clusters [52, 53] might be interesting for the design of efficient, table-top X-ray lasers sources. However, most of the high amount of energy absorbed from the exciting laser field is converted into ion kinetic energy and not into the X-rays.

The phenomenon of extremely high ion kinetic energies suggested the creation of plas-

mas through irradiation of clusters and the use of the energetic ions for substantial *nuclear fusion*. After the irradiation of deuterium clusters it was found that neutrons are produced in a quantity, which was formerly only reached by large-scale laser-driven fusion experiments [54].

All effects mentioned above are based on the strong electric field in conjunction with the relatively low frequencies of optical lasers. As a consequence of this conjunction, the laser electric field causes field ionisation processes of the atoms constituting the clusters and large quivering energies of the electrons in the laser field. On the other hand, the high frequency of VUV radiation can be expected to reduce or even inhibit these processes. Therefore the interaction of a strong electric field at a high VUV radiation frequency with clusters is very interesting.

3.3.4 Ionisation of clusters by intense VUV photons studied by mass spectroscopy

Interaction of intense radiation pulses with clusters results in various ionisation products, such as electrons and ionised cluster fragments of different size. The fragments as final products of this process directly reflect the dynamics, including absorption, ionisation and expansion of the cluster. Time-of-flight mass spectrometry is ideal for the study of the ionisation process, because it allows detection of all charged species and the determination of their kinetic energies resulting from the process simultaneously. In the following section TOF mass spectra are presented, which were taken with the TOF mass spectrometer described in section 2.3.1.

In Figure 3.8 time-of-flight (TOF) mass spectra of ionisation products of Xe atoms and clusters are shown. The spectra were recorded after ionisation with FEL radiation at a wavelength of 98 nm and an average power density of 8×10^{12} W/cm^2. Each spectrum is a sum of 100 subsequent single-shots. The bottom trace displays the atomic spectrum. It shows a splitting into several lines owing to the different isotopes. The absence of highly charged ions, which were observed in TOF mass spectra of an atomic beam taken in the second experimental run (see Figure 3.3) can be explained by different experimental conditions of the two different experimental runs, see discussion in section 3.1. The traces above the atomic spectrum display mass spectra of three different cluster sizes $\bar{N}$, which is the average number of Xe atoms comprised in the cluster. The biggest clusters comprise $\sim 90,000$ atoms and show all charge states of atomic ions up to Xe^{8+}. In all three cluster spectra the mass peaks are rather broad, indicating that the ions have a high initial kinetic energy. To quantify this observation the flight times of atomic Xe ions initially at rest were calculated with the simulation software package SIMION 3D 7.0. The calculated flight times are indicated by thin vertical lines in the uppermost part of Figure 3.8 for charge states Xe^+-Xe^{8+}. A comparison with the measured flight times reveals that for the biggest cluster size the atomic ions span
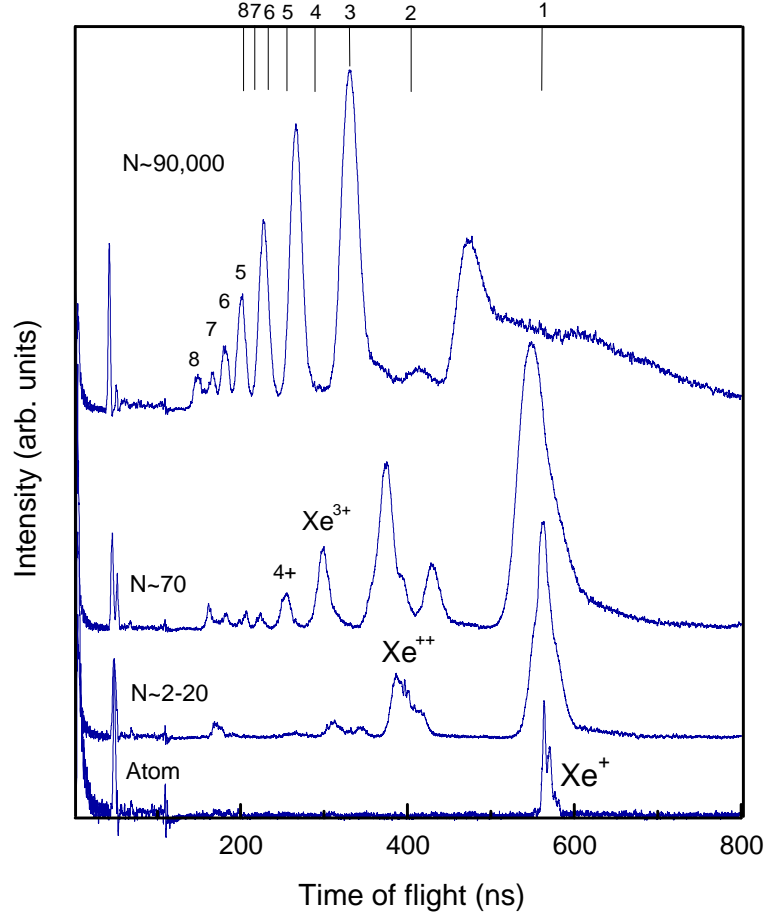
Figure 3.8: TOF mass spectra of Xe atoms and clusters at an average power density of $P_{FEL} = 8 \times 10^{12} \, \text{W/cm}^2$

a range of initial kinetic energies from $200 \, \text{eV}$ (Xe^+) to more than $3 \, \text{keV}$ (Xe^{8+}). The high kinetic energies together with the absence of heavier fragments (e.g. Xe_2^+ at $\sim 806 \, \text{ns}$ or Xe_3^+ at $\sim 987 \, \text{ns}$, see Figure 3.9), leads to the conclusion, that clusters absorb many photons and disintegrate completely. This behaviour can be understood in terms of a Coulomb explosion and will be discussed in section 3.3.5.

In Figure 3.9 the dependence of the fragmentation on the power density of the FEL was investigated. TOF mass spectra of Xe_{2500} clusters for five different power densities are displayed. The power densities P_{FEL} are given next to each trace and decrease from the top to the bottom. Apart from the spectrum at the bottom, all spectra were taken at a pulse energy of $\sim 25 \, \mu J$ of the $\sim 50 \, \text{fs}$ long [4] FEL-pulses. The highest power density $P_{FEL} = 3 \times 10^{13} \, \text{W/cm}^2$ corresponds to the power density in the focal spot ($\sim 20 \, \mu m$ diameter). By moving the interaction region out of the focal spot the power density could be lowered to $P_{FEL} = 8 \times 10^{10} \, \text{W/cm}^2$ at a distance of $15 \, \text{mm}$ to the focal region. The spectrum at the bottom was also taken at $15 \, \text{mm}$ distance

but at a lower pulse energy which further reduced P_{FEL} to 2×10^{10} W/cm^2. As can be seen, irradiation of 2500-atom Xe clusters at the highest power level produced all charge states up to 8+. Lowering P_{FEL} strongly reduced the intensity of highly charged states. At 8×10^{10} W/cm^2 only singly charged Xe ions with a high kinetic energy were detected. Further reducing P_{FEL} by averaging single-shots at low FEL gain resulted in a decreasing signal and simultaneously a change of the initial kinetic energy.

The clear message of Figure 3.9 is that optical nonlinear processes dominate the ionisation of the clusters.
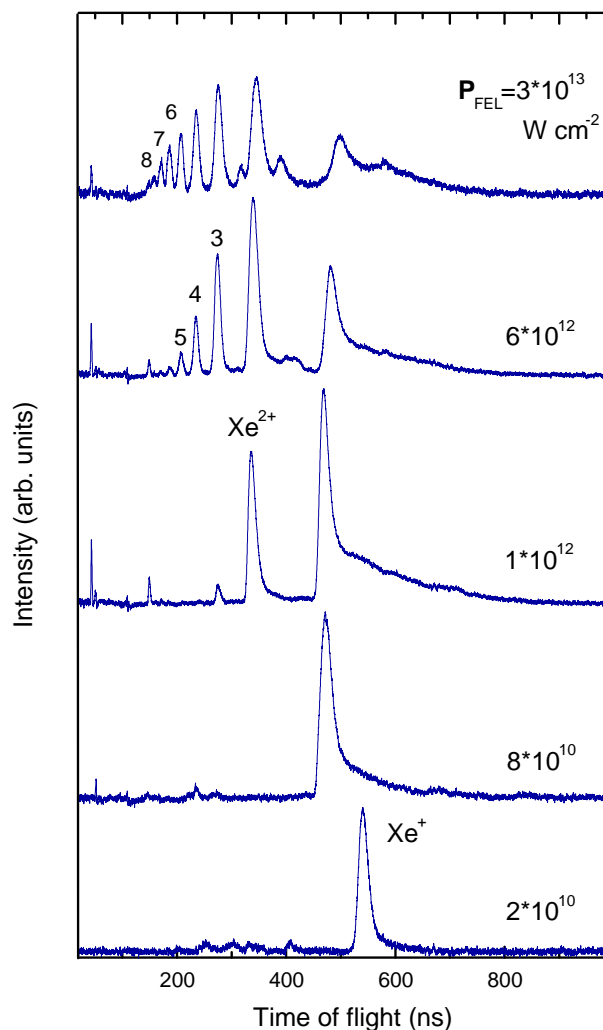

Figure 3.9: TOF mass spectra recorded after irradiation of Xe$_{2500}$ clusters as a function of power density.

3.3.5   Coulomb explosion

The observation of charge states with high initial kinetic energies in the TOF mass spectra raises the question: What mechanism causes the cluster to expand?

Two models for the expansion of clusters are described in the following.

Coulomb explosion is expected to govern predominantly the expansion dynamics of small clusters. In the framework of Coulomb explosion a significant loss of electrons causes a charge build up in the cluster. The mutual Coulomb repulsion of the highly charged ions in the cluster forces the cluster to expand [49]. In this case the accumulated Coulomb energy is converted into ion kinetic energy. A quadratic dependence of the ion kinetic energy as a function of ion charge state is well accepted as a signature of Coulomb explosion, see discussion below.

The *hydrodynamic expansion* of a cluster is mostly attributed to big clusters [49]. The driving force on the ions results from the pressure associated with hot electrons. The heated electrons expand and pull the cold, heavy ions outwards with them. In this case the thermal energy of hot electrons is transformed into ion kinetic energy. A linear dependence of ion kinetic energy as a function of ion charge state as a clear sign of hydrodynamic expansion is still matter of discussions [55, 56].

To identify the responsible expansion mechanism the ion kinetic energies or ejection energies of the ions were determined by simulating ions of the respective charge state in SIMION 7.0, see description in section 2.3.1. To this purpose, a number of ions with increasing ejection energies ($\Delta E_{ej} = 1\,\text{eV}$) were simulated for each charge state. The resulting flight times were used to build tables of the flight time as a function of ejection energy. Finally, the value of the ejection energy corresponding to the measured *mean* flight time was picked out of the tables for each charge state. The reliability of the simulation is is discussed in detail in section 3.3.6.3.

In Figure 3.10 the *mean* ejection energy $\bar{E}_{ej}$ of ion charge states belonging to the measurement displayed in the uppermost trace in Figure 3.9 is given as a function of the *individual* charge state z.

The ejection energy of the ions shows clearly a quadratic dependence on their charge. An explanation of the quadratic behaviour is given in [56]. The authors of [56] argue that an explicit quadratic dependence for the *mean* ejection energy $\bar{E}_{ej}$ and the *mean* charge state $\bar{z}$

$$\bar{E}_{ej} = \frac{(\bar{z}e)^2}{N} \sum_{i=1}^{N-1} \sum_{j=i+1}^{N} \frac{1}{\mid \vec{R}_i - \vec{R}_j \mid} \propto (\bar{z}e)^2 \qquad (3.6)$$

is obtained. Here N is the number of ions in the cluster and $\vec{R}_i$ and $\vec{R}_j$ denote the positions of ions i and j respectively. According to [56] the quadratic behaviour of the *mean* kinetic energy as a function of *individual* charge applies for charge states z lower than the *mean* charge state $\bar{z}(P_{max})$ at the maximum power density P_{max}. A linear behaviour is expected for charge states $z > \bar{z}(P_{max})$. The two different behaviours are
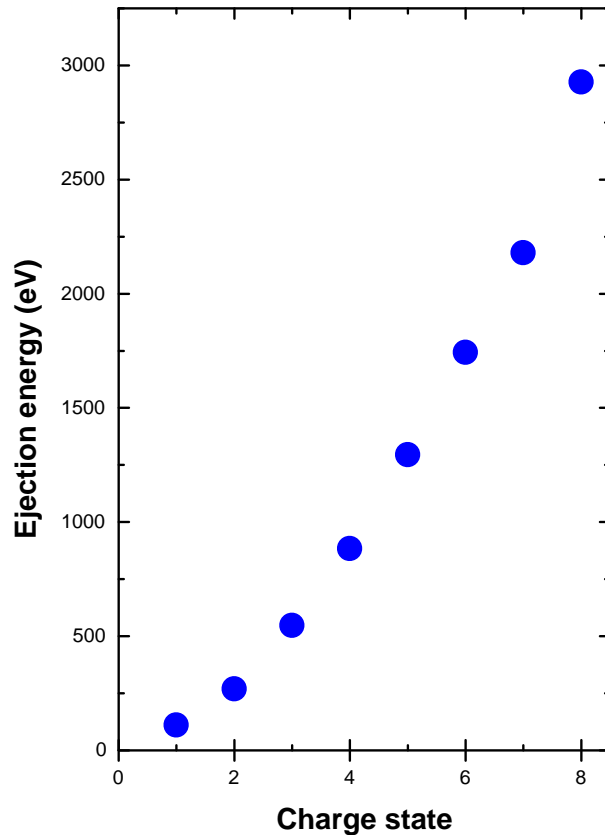
Figure 3.10: Mean ejection energies of ion charge states after irradiation of a Xe_{2500} cluster. The power density was $P_{FEL} = 3 \times 10^{13}$ W/cm^2. The quadratic dependence of the mean ejection energy is a clear sign of a Coulomb explosion. For details see text.

explained by the spatial profile of the laser, where the behaviour for $z < \bar{z}(P_{max})$ contains the contribution from the entire power density range, while that for $z > \bar{z}(P_{max})$ contains only the contribution from the limited spatial area where the power density is close to P_{max}. Both behaviours, the quadratic as well as the linear behaviour, result from a Coulomb explosion [56]. In conclusion, the strong quadratic dependence of the lower charge states (z$\leq$ 3) in Figure 3.10 evidences a Coulomb explosion.

For the sake of completeness, it should be also noted, that according to recent theoretical work [57] a quadratic behaviour is only observed if the duration of the laser pulse is short compared to the typical time needed for the cluster explosion.

Therefore the expansion mechanism of xenon clusters exposed to the short wavelength radiation of the FEL is due to a Coulomb explosion. Figure 3.9 shows that Coulomb explosion starts already at power densities below 10^{11} W/cm^2. This is about two orders of magnitude lower than in experiments with infrared lasers. This behaviour can be understood if one takes into account that the ionisation efficiency of Xe atoms by VUV light exceeds substantially that of IR light at 10^{11} W/cm^2.
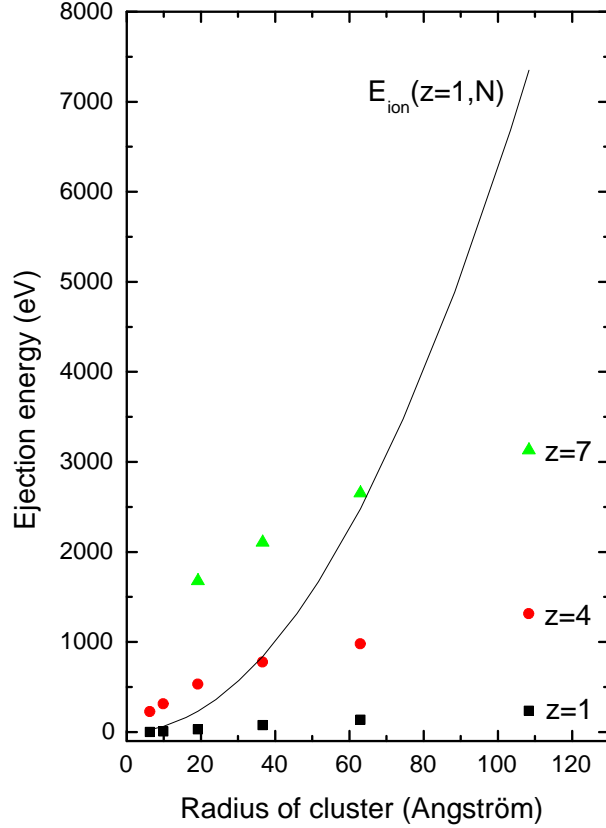
Figure 3.11: Ejection energy of three different ion charge states as a function of cluster radius. The ejection energies were determined from the set of TOF spectra given in Figure 3.8 with three additional cluster sizes. The average power density of the FEL was $P_{FEL} = 8 \times 10^{12}\,\mathrm{W/cm^2}$. The respective ion charge states are given next to the ejection energy corresponding to the biggest cluster radius. The solid line represents the mean ejection energy $\bar{E}_{ion}(z = 1, N)$ of singly charged ions as a function of cluster radius, if the cluster is regarded as a homogeneously charged sphere. The much lower values of the measured ejection energies indicate that the energy deposited in the cluster due to the interaction with FEL radiation is not sufficient to accomplish Coulomb explosion in the initial geometry of the cluster.

Another interesting question is whether or not Coulomb explosion starts initially from the geometric arrangement of the neutral cluster. To answer this question the total Coulombic energy of a charged cluster with radius R, where R corresponds to the intact geometry, is calculated using a simple model. The cluster containing N ions of the same charge state z is assumed as a homogeneously charged sphere with radius R and total charge $Q = Nze$, where e is the electron charge. The Coulomb energy of an ion on the surface of the cluster is then:

$$E_{ion}(z, N) = \frac{ze \cdot (Nze)}{4\pi\epsilon_0 R} \tag{3.7}$$

To calculate the total Coulombic energy E_C in the cluster the contributions of all ions have to be summed up. Additionally the radius R can be replaced by the relation $R = (3N/4\pi\rho)^{1/3}$ because the cluster is assumed as a sphere. Here $\rho = 2.74 \cdot 10^{28} \, \mathrm{m}^{-3}$ is the atomic density of solid xenon. Therefore E_C is:

$$E_C(z, N) = \frac{z^2 e^2}{4\pi\epsilon_0 \sqrt[3]{\frac{3}{4\pi\rho}}} \sum_{n=1}^{N} n^{\frac{2}{3}} \tag{3.8}$$

Dividing the total Coulombic energy E_C by the total number of ions in the cluster gives out the mean Coulombic energy per ion or in other words the mean ejection energy $\bar{E}_{ion}$ an ion gains in the course of a Coulomb explosion of a cluster with neutral state geometry as a function of the number of ions N in the cluster. In practical units [eV] equation (3.8) gives:

$$\bar{E}_{ion}(z, N)[eV] = 6.0 \cdot z^2 \frac{\sum_{n=1}^{N} n^{\frac{2}{3}}}{N} \tag{3.9}$$

In Figure 3.11 the theoretical curve for singly charged ions $\bar{E}_{ion}(z = 1, N)$ (solid line) is compared with measured values of ion ejection energies for three different ion charge states. The measured ion ejection energies correspond to the set of TOF mass spectra given in Figure 3.8 plus three additional cluster sizes. The determination of the ejection energies were achieved by simulating the mean flight times of the respective ion charge states as described above. For reasons of simplicity the ion ejection ejection energies are given as a function of cluster radius R, which is related to the total number of ions N in a cluster by the above relation $R = (3N/4\pi\rho)^{1/3}$. The calculated curve $\bar{E}_{ion}(z = 1, N)$ for a Coulomb explosion from intact cluster geometry reveals much higher ejection energies than measured in the experiment. This comparison shows qualitatively, that the Coulomb explosion in the FEL-experiment is not accomplished in the initial cluster geometry. Instead of this the cluster expands before all electrons are removed from the cluster. The removal or *outer ionisation* (see section 3.3.6.1) of the electrons is then completed at a bigger cluster radius than the initial radius R. From this, it can be concluded that the energy deposited in the cluster because of the laser-cluster interaction is not sufficient, to remove all Nz electrons from the cluster to infinity while the cluster remains in his intact geometry. This conclusion is also supported by the observation, that the experimental values in Figure 3.11 saturate with increasing cluster radius. This behaviour is expected, because the energy needed to remove N electrons from the cluster scales approximately with $\sim N^2$, see equation (3.8).

3.3.6 Theoretical description of cluster-light interaction

Clusters irradiated with infrared laser light at $> 10^{15} \, \mathrm{W/cm}^2$ completely disintegrate [49, 50, 55]. Therefore the interaction of intense lasers with clusters has attracted great

interest and has been studied extensively theoretically [58–62] in the past few years. For a very recent and extensive review see [63]. The interpretation of the heating mechanism is still a subject of discussion.

In the paper of Ditmire *et al.* [49] the authors propose a *nanoplasma model* for big clusters. In this model the interaction of the laser with the cluster is treated as an interaction of the laser with a small ball of high-density plasma. Once atoms in the cluster are field ionised by the laser a plasma is formed. It consists of positively charged ions and electrons which are confined to the cluster, but can move freely inside the cluster. Inverse bremsstrahlung of the electrons in the laser electric field efficiently 'heats' the electron gas, thereby absorbing energy from the laser field. Further (inner) ionisation mainly proceeds via collisional ionisation by the 'heated' electrons. The expansion is then dominated by the pressure of the hot electron gas (hydrodynamic expansion).

A different model was proposed by Rose-Petruck *et al.* in [58]. The authors studied the ionisation dynamics of small rare gas clusters via classical trajectory Monte Carlo simulations. According to the *ionisation ignition model* they proposed, the ionisation is driven by the combined electric field of the laser, the other ions and the electrons. This model predicts that the ionisation increases rapidly, once the laser power density has reached the threshold for single ionisation. As the ionisation proceeds beyond this first ionisation stage, strong electric fields build up within the cluster and further enhance the ionisation.

An alternative explanation of enhanced energy absorption for small rare gas clusters is given in [64]. According to the quasi-classical model in [64] a critical interionic distance R^* of the ionised atoms in the cluster exists at which the outer ionisation is strongly enhanced, provided that the laser pulse duration is sufficiently long to let the cluster expand until R^* is reached. The mechanism responsible for this enhancement is described in analogy with the *enhanced ionisation* (ENIO) [65, 66] first discovered in diatomic molecules as a lowering of the potential barriers for outer and inner ionisation simultaneously below the laser electric field.

However, in all above mentioned models the ionisation is explained by field ionisation of the atoms and the clusters by the strong electric field of the infrared laser.

In the FEL-experiment the frequency ω_{FEL} of the FEL radiation is so high that the direct effect of the laser field on the electrons is expected to be small [67]. Whether field ionisation is efficient can be estimated from the Keldysh formalism described in section 3.2.2. Field ionisation dominates if the Keldysh parameter γ is smaller than 1. The conditions in the FEL-experiment are such, that γ varies between ~ 8 (Xe atoms, ionisation potential $I_p = 12.1\,\mathrm{eV}$) and ~ 100 (electrons bound to highly charged Xe clusters). Therefore field ionisation can hardly account for the observations. Consequently, additional processes have to be considered for the understanding of absorption, ionisation and explosion dynamics with short-wavelength radiation.

Three questions will be addressed in the following:

1. What is the ionisation mechanism that causes the massive electron ejection?

2. How can the high charge states of the atomic ions be explained?

3. Which process allows the cluster to absorb such a large amount of energy from the laser field?

3.3.6.1   Modelling of inner and outer ionisation

To help the understanding of the findings, we recall that the binding energy of electrons in clusters increases strongly with the charge of the cluster. The total energy needed to remove N electrons from a cluster comprising N atoms is as high as $\sim 6 \times 10^8$ eV for $N = 90,000$, see equation (3.8), if the radius of the cluster remains unchanged during ionisation. It is assumed that the ionisation is a two-step process, as in the case of irradiation with infrared light [59, 62].

Inner ionisation
In a first step, atoms inside the cluster lose at least one electron. These electrons are confined to the cluster by space charge, but can move freely inside the cluster. This is called *inner ionisation.* It can be easily explained, because the energy of FEL photons at 98 nm wavelength (12.7 eV) exceeds the ionisation energy of Xe atoms (12.1 eV). Therefore, it is assumed that valence electrons in the cluster are promoted to excited states (conduction band). To estimate how fast this promotion is, it is recalled that the cross section for Xe atoms at 98 nm wavelength is 20-40 Mbarn($=10^{-18}$ cm^2) [41]. At $5 \mu J$ radiation pulse energy, we have a large number of photons ($\sim 2 \times 10^{12}$) impinging on a focal area of $A_{fokus} = \pi(10 \mu m)^2$. This gives $\sim 6 \times 10^{18}$ photons/cm^2 in one pulse. As a result, for a 50 fs long radiation pulse ($\sim 2.5 \times 10^{13}$ W/cm^2) the outermost valence electron of each atom is promoted during the first few femtoseconds of the pulse.

Outer ionisation: Numerical modelling of electron trajectories
In a second step, the electrons are removed from the cluster to infinity. This process is called *outer ionisation.* To explain the outer ionisation simulations of the electron movement in Xe$_{13}$ and Xe$_{55}$ clusters have been performed using a classical model [68]. The classical trajectory calculations are based on a model presented in [59]. The motion of the unbound (inner ionised) electrons are simulated under the influence of the ions and electrons in the cluster and of the electric field of the FEL. The simulations start with a nearly spherical $(Xe^{Z+})_N$ cluster containing $N \cdot z$ free electrons. The positions of the ions are arranged in an fcc-structure with atomic distances of 4.33Å, which is the nearest neighbour distance in solid xenon. This simplification should not affect the results, since the basic shell-like structure of rare gas clusters is not affected. The ion positions are kept fixed during the simulation. The electrons are treated as

classical point charges. They move under the influence of the laser electric field $\vec{E}$ and the combined potential of the ions U_{ion} and the electrons U_e. The laser electric field

$$\vec{E} = \vec{e}_x E_0 \cos(\omega_{FEL} t) \tag{3.10}$$

is linearly polarised in the x-direction and assumed to be constant over the cluster dimensions. The power density P_{FEL} and therefore also the maximum electric field strength E_0 is kept constant during the simulation of an FEL pulse and the phase is set to zero [59].

The potential of the ions is given by:

$$U_{ion} = -\frac{BZ}{r} + \frac{C}{r^6} \tag{3.11}$$

Here r denotes the distance between electron and ion. The first term with $B = 14.385\,\text{eV\AA}$ describes the attracting Coulomb potential. The second term models the elastic scattering of the electrons at the ion cores. C was set to $C = 410\,\text{eV\AA}^6$. According to [59] the constant C has only minor influence.

Finally, the repelling Coulomb forces between the electrons were taken into account:

$$U_e = \frac{B}{\sqrt{r^2 + r_0^2}} \tag{3.12}$$

where r is the distance between the electrons. The pole of the potential is avoided by 'rounding' it with a minimum distance of $r_0 = 0.2\,\text{Å}$. This is to avoid numerical instabilities. The simulation then works by numerically integrating the equations of motion in discrete time steps Δt:

$$\vec{r}(t + \Delta t) = \vec{r}(t) + \vec{v}(t)\Delta t \tag{3.13}$$

$$\vec{v}(t + \Delta t) = \vec{v}(t) + \vec{a}(t)\Delta t \tag{3.14}$$

The acceleration $\vec{a}(t)$ of the kth electron is the sum of the acceleration by the ions $\vec{a}_{ion}$, the other electrons $\vec{a}_e$ and the electric field of the FEL $\vec{a}_{FEL}$.

$$\vec{a} = \vec{a}_{ion} + \vec{a}_e + \vec{a}_{FEL} \tag{3.15}$$

The contributions of ions and electrons are calculated using $\vec{a} = \vec{F}/m_e = e \cdot grad U/m_e$, where U denotes U_{ion} and U_e respectively:

$$\vec{a}_{ion} = \frac{e}{m_e} \sum_{i=1}^{N} \left(\frac{Bz}{r_i^3} - \frac{6C}{r_i^8} \right) \vec{r_i} \tag{3.16}$$

$$\vec{a}_e = -B \sum_{m=1, m \neq k}^{Nz} \frac{\vec{r_m}}{\left(r_m^2 + r_0^2 \right)^{3/2}} \tag{3.17}$$

Here e and m_e are the mass and charge of the electron.

The contribution of the FEL is:

$$\vec{a}_{FEL}(t) = \frac{e}{m_e} \vec{e}_x E_0 cos \left(\frac{2\pi c}{\lambda_{FEL}} t \right) \tag{3.18}$$

Here the relation $\omega_{FEL} = 2\pi c/\lambda_{FEL}$ is used.

The resulting electron positions for three simulations with different laser parameters are presented in Figure 3.12. For all three simulations the laser polarisation is along the x-direction. The vertical scale $(y^2 + z^2)^{1/2}$ shows the distance from the cluster.

In the uppermost panel conditions typical for optical laser experiments were chosen. The laser wavelength is $800\,\text{nm}$ and the power density is $10^{16}\,\text{W/cm}^2$. Two snapshots of the positions after $10\,\text{fs}$ and $20\,\text{fs}$ are shown. In both cases the electrons are emitted preferentially into the laser polarisation direction. Inspections of individual trajectories show that most electrons exit the cluster during the first optical cycle. This is a clear sign for field ionisation.

On the contrary, the electrons in the middle panel are emitted isotropically. The
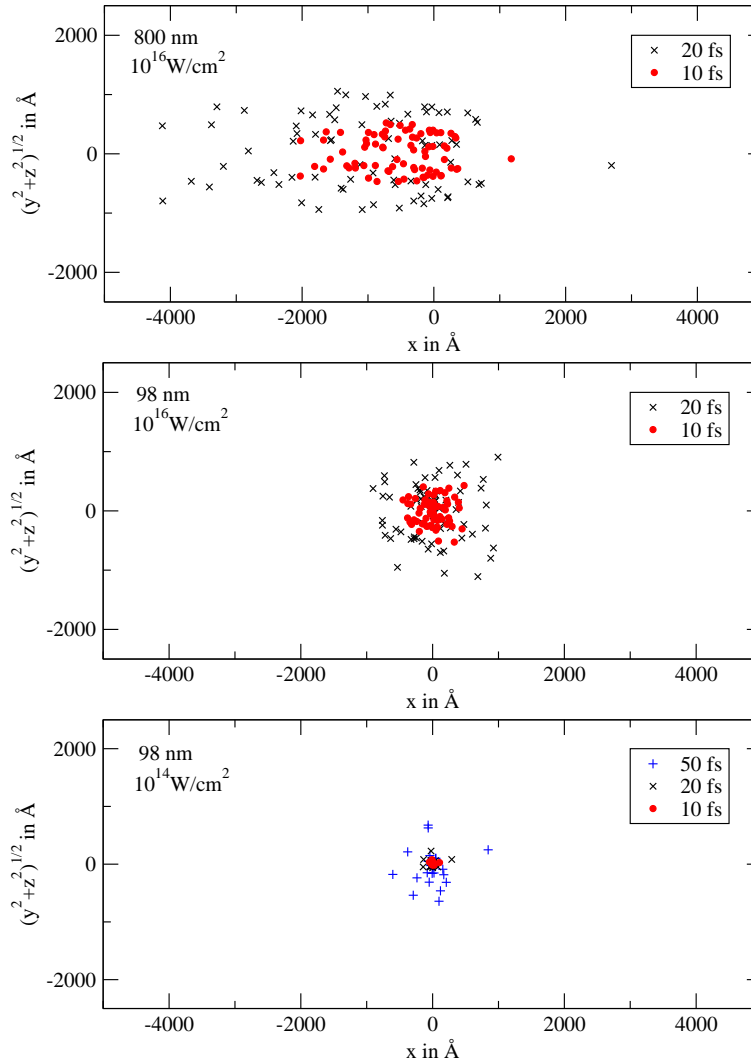

Figure 3.12: Electron emission of Xe_{55} clusters calculated with classical particle simulation [68]. For details see text.

power density of 10^{16} W/cm^2 is the same as in the upper panel but the wavelength of 98 nm is now that of the FEL. Further, it is evident that the electrons stay longer inside the cluster.

In the lowermost panel the power density of 10^{14} W/cm^2 was adjusted to our experimental conditions. Electron emission is also isotropically but strongly reduced and electrons need even more time to leave the cluster. To show that the simulation still predicts noticeable emission a snapshot after 50 fs was added.

The isotropic emission of electrons at 98 nm wavelength shows that field ionisation does not play a significant role. On the other hand, electrons need more time to escape the cluster. The explanation for this prolongation of the ionisation process can be given by a closer inspection of the electron trajectories.
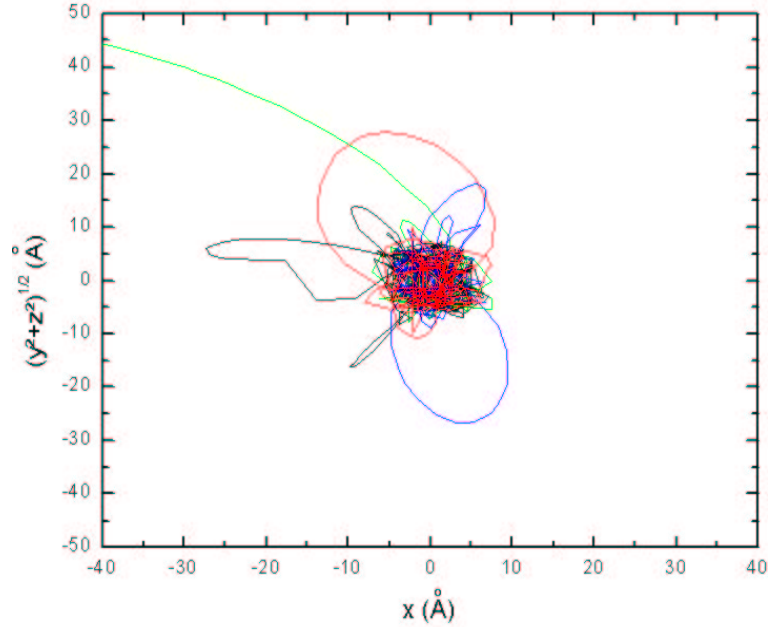

Figure 3.13: Classical simulation of electron trajectories in a $(Xe^{6+})_{13}$ cluster. The four displayed trajectories were randomly taken from the set of 78 simulated trajectories. The laser parameters for the simulation were set to 98 nm wavelength, 10^{14} W/cm^2 and 50 fs pulse duration. Only after many scattering events one electron has gained enough energy to leave the cluster.

In Figure 3.13 four trajectories of electrons are displayed. The four displayed trajectories were randomly taken from a set of 78 trajectories, which were simulated for 78 unbound electrons in a $(Xe^{6+})_{13}$ cluster for a 50 fs long pulse at 10^{14} W/cm^2 and 98 nm wavelength. The trajectories show that the electrons undergo many scattering events before eventually one electron has gained enough energy to leave the cluster.

In Figure 3.14 the steps of the proposed ionisation process are illustrated. The Coulomb potential of the cluster is shown at the beginning of the FEL pulse, at its maximum
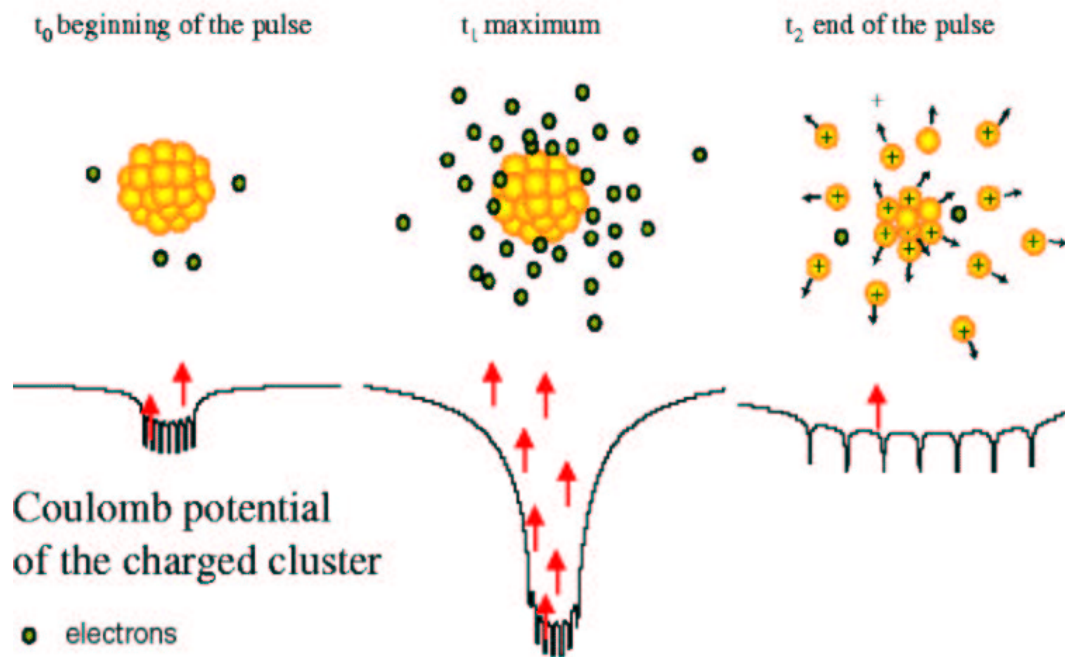
Figure 3.14: Schematic illustration of the ionisation of Xe clusters and a subsequent Coulomb explosion.

and at the end of the pulse. Photons are indicated by arrows. In the first step a few electrons are ejected from the cluster, because their binding energy is smaller than the energy of the FEL photons. This process depends on the cluster size. However, once a few electrons leave, the cluster becomes charged and the binding energy for remaining electrons increases. At the stage where the binding energy exceeds the photon energy, only hot electrons can leave the cluster. On the other hand, electrons in valence band and in excited states can absorb photons. Therefore it is assumed that after a few femtoseconds a nanoscale plasma is formed, which is confined by the cluster. Because the Coulomb force is long range, the electrons can stay with a high probability outside the cluster, but still bound to it. These loosely bound electrons can then be removed to infinity (second step) by absorption of additional photons or by collisions with other electrons in the vicinity of ions. Once a large number of electrons have left the cluster, the cluster starts to disintegrate by Coulomb explosion. As a result, the Coulomb potential flattens and the binding energy of the electrons is reduced. This favours the outer ionisation of electrons.

3.3.6.2   Population of high charge states

Now addressed is the question as to how the appearance of high charge states can be explained.

It can be assumed that highly charged ions are formed at the surface of the cluster by field ionisation in the strong Coulomb field of the ions inside the cluster [60]. If the cluster is assumed to be a homogeneously charged sphere, the electric field strength E_{ion} originating from the positively charged ions as a function of the distance from the centre d can be calculated,

$$E_{ion} = \frac{N \bar{z} e d}{4 \pi \epsilon_0 R} \qquad (3.19)$$

Here N is the number of charged ions, $\bar{z}$ is the average ion charge state and R is the radius of the charged sphere, i.e. the radius of the cluster. The horizontal lines in Figure 3.15 mark the appearance field strengths of Xe ions charge states $E_{ap}(Xe^{z+})$ from Xe$^+$ - Xe^{8+}. Following the Bethe-model, $E_{ap}(Xe^{z+})$ is defined as the field strength E_{ext} at which an external electric field compensates the atomic field strength [63]. Using

$$V_{com}(x) = -\frac{z e^2}{4 \pi \epsilon_0 x} - e E_{ext} x \qquad (3.20)$$

for the combined potential of the ion and the external field as a function of x. Setting $\frac{\partial V_{com}(x)}{\partial x} = 0$ results in

$$E_{ap}(Xe^{z+}) = \frac{I_p(Xe^{z+}) \pi \epsilon_0}{4 z e^3} \qquad (3.21)$$

where $I_p(Xe^{z+})$ denotes the energy needed to ionise an ion from charge state $z - 1$ to z (ionisation potential). Values for Xe$^+$ - Xe^{8+} are given in Table 3.2.

ionisation potential I_p [eV]	charge state z	E_{ap} [V/m]	P_{ap} [W/cm^2]
12.1	1	2.54×10^{10}	8.57×10^{13}
21.0	2	3.82×10^{10}	1.94×10^{14}
32.1	3	5.96×10^{10}	4.72×10^{14}
46.7	4	9.46×10^{10}	1.19×10^{15}
59.7	5	1.24×10^{11}	2.03×10^{15}
71.8	6	1.49×10^{11}	2.95×10^{15}
92.1	7	2.10×10^{11}	5.87×10^{15}
105.9	8	2.43×10^{11}	7.86×10^{15}

Table 3.2: Electric field strengths E_{ap} and power densities P_{ap} at which Xe ions appear due to above barrier ionisation. For comparison, at 2.5×10^{13} W/cm^2 the electric field strength of the FEL is $E_{FEL} = 1.4 \times 10^{10}$ V/m, which is even lower than E_{ap} for Xe^+.

In Figure 3.15 E_{ion} is preselected for a Xe$_{2500}$ cluster (R=32.6 Å) with 2500 singly charged ions. This corresponds to a situation in which one electron per atom is outside

the cluster. Well before the cluster radius of 32.6 Å is reached, E_{ion} is high enough to produce even Xe^{8+}, which is the highest charge state observed in our experiment. This gives a straightforward explanation for the production of highly charged ions.
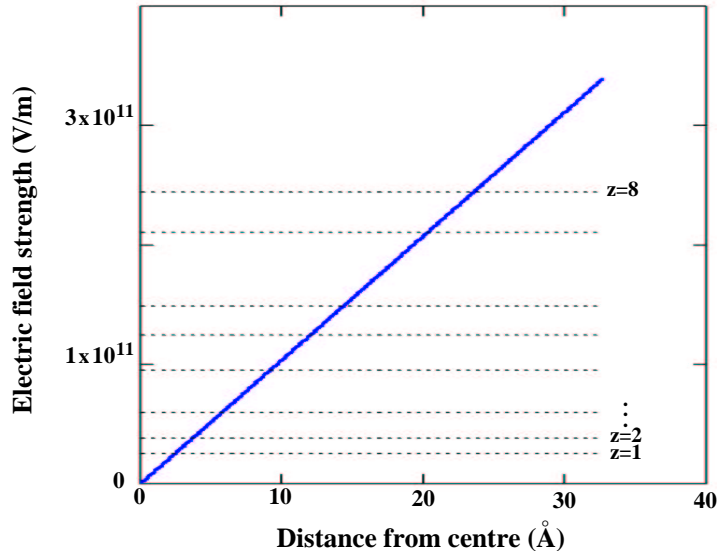

Figure 3.15: Electric field strength of a homogeneously charged Xe_{2500} cluster as a function of distance from the centre. The cluster with a radius of 32.6 Å contains 2500 singly charged ions. At the horizontal lines the electric field of the cluster is strong enough to produce Xe ions with charge state z by above barrier ionisation. Charge states z are given next to each line.

3.3.6.3 Average energy absorption and cross section

The mechanisms which allow the cluster to absorb such a high amount of energy are now further discussed. The energy released in the Coulomb explosion corresponds to that due to the absorption of many photons. This number of photons is estimated by dividing the average ejection energy of ions by the photon energy.

Average ejection energy

The procedure to calculate the *average ejection energy* of ions is as follows. At the beginning the mean kinetic energies of the peaks belonging to single charge states and their appropriate widths were determined. This was done by fitting the measured TOF mass spectrum, assuming the shape of the peaks as Gaussian. Input parameters and simulation results are given Table 3.3. Next, the *relative geometric acceptance* is determined as described in Section 2.3.1. Briefly, the mean kinetic energy and width of the energy distribution for each charge state were used as input parameters to generate

isotropic ion distributions. By simulating the same number of ions for each charge state, the final number of ions hitting the detector was then regarded as the *relative geometric acceptance*. To show the reliability of the simulation, measured and simulated TOF mass spectrum are compared in Figure 3.16. For the simulated spectrum the input parameters are listed in Table 3.3. The measured spectrum was taken after Coulomb explosion of $(Xe)_{2500}$ clusters at a power density of $P_{FEL} = 2.5 \times 10^{13} \, W/cm^2$.
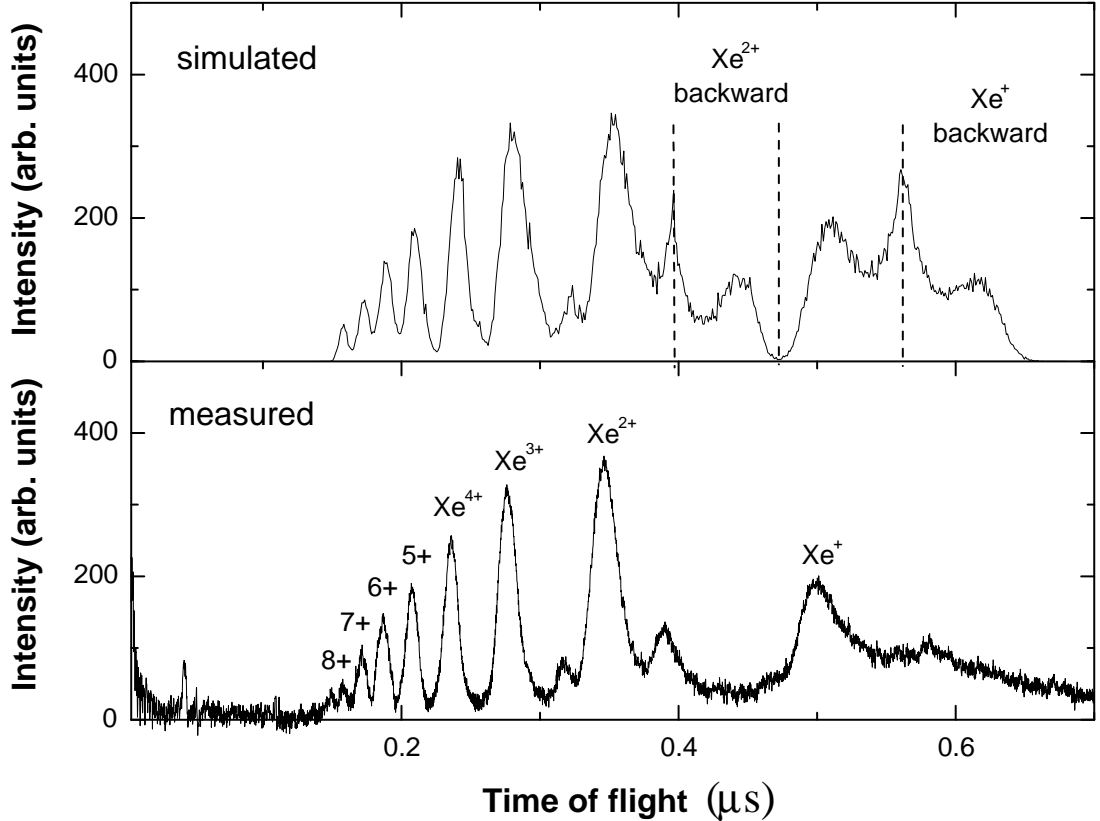

Figure 3.16: Comparison of measured and simulated TOF spectrum. Mean energy of charge states and respective widths were taken as input parameters for the simulation.

Experiment and simulation are in good agreement. The most significant difference in the simulation shows up for Xe^+ and Xe^{2+} ions ejected into the hemisphere facing away from the detector, which are called 'backward' in the figure. 'Backward' ions are ejected against the potential gradient of the pull-in voltage and arrive at longer flight times at the MCP than ions of the same charge state ejected into the 'forward' direction.[6] The 'backward' Xe^+ and Xe^{2+} ions seem to be smeared out or even absent in the experimental mass spectrum. For higher charge states 'forward' and 'backward' ions overlap in the simulated spectrum and the difference is not that pronounced anymore, but the

---

[6]The present TOF spectrometer was designed to obey the conditions of Wiley-McLaren time-of-flight focusing [32]. This is the reason why 'forward' and 'backward' ions are separated in flight time.

	Xe^+	Xe^{2+}	Xe^{3+}	Xe^{4+}	Xe^{5+}	Xe^{6+}	Xe^{7+}	Xe^{8+}
Input parameters								
mean ej. energy [eV]	93	261	526	844	1284	1729	2228	3102
FWHM [eV]	109	257	416	524	699	899	1061	1177
number of ions:								
simulated (for/back)				314,000 for each charge state				
Simulation results								
hits (for): $N_{z,hit}$	21992	13717	8812	6623	5423	4892	4411	3467
$G_{z,n} = N_{z,hit}/N_{1,hit}$	1	0.624	0.401	0.301	0.247	0.223	0.201	0.158
integrated intensity A_z	8.03	8.98	4.71	2.80	1.76	1.26	0.71	0.28

Table 3.3: Simulation of a whole TOF mass spectrum: Input parameters and simulation results. The integrated intensity A_z is given for the sake of completeness. Its values were determined from the measured TOF mass spectrum given in Figure 3.16.

simulated peaks are broader than their measured counterparts. This observation leads to the conclusion, that the actual detector (*cluster ion TOF*) suppresses 'backward' emitted ions. This suppression might be attributed to the effect of space charge. After removing the contributions of 'backward' ions from the simulation the agreement is in fact very good. Consequently, the *relative geometric acceptance* was calculated taking into account only the forward contribution of each charge state. Because Coulomb explosion is isotropic, this does not affect the results.

With the knowledge of the mean kinetic energy $\bar{E}_{z,ej}$, the geometric acceptance g_z, the MCP detection efficiency ϵ_z (section 2.3.1) and the integrated area A_z of each charge state in the measured spectrum, the *average ejection energy* is calculated by:

$$\bar{E}_{ej} = \frac{\sum_{z=1}^{8} \left(\bar{E}_{z,ej} \cdot \frac{A_z}{G_{z,n} \cdot \epsilon_{z,n}} \right)}{\sum_{z=1}^{8} \frac{A_z}{G_{z,n} \cdot \epsilon_{z,n}}} \qquad (3.22)$$

where $G_{z,n} = G_z/G_1$ which is the same as $G_{z,n} = N_{z,hit}/N_{1,hit}$ as defined in Table 3.3 and $\epsilon_{z,n} = \epsilon_z/\epsilon_1$ is taken from Table 2.3.

For Xe_{2500} clusters irradiated at a power density of $P_{FEL} = 2.5 \times 10^{13}\,\text{W/cm}^2$ this yields:

$$\bar{E}_{ej} = 640\,eV/atom \qquad (3.23)$$

Average charge state

Following the procedure introduced above, the *average charge state* was calculated with:

$$\bar{z} = \frac{\sum_{z=1}^{8} \left(z \cdot \frac{A_z}{G_{z,n} \cdot \epsilon_{z,n}} \right)}{\sum_{z=1}^{8} \frac{A_z}{G_{z,n} \cdot \epsilon_{z,n}}} \qquad (3.24)$$

resulting in

$$\bar{z} = 3.0 \, /atom \tag{3.25}$$

for $(Xe)_{2500}$ clusters irradiated at a power density of $P_{FEL} = 2.5 \times 10^{13} \, \mathrm{W/cm^2}$.

Average cross-section

At a power density of $P_{FEL} = 2.5 \times 10^{13} \, \mathrm{W/cm^2}$, a pulse duration of $\tau_{rad} = 50 \, \mathrm{fs}$ and a photon energy of $\sim 12.65 \, \mathrm{eV}$, every atom absorbs on average $640 \, \mathrm{eV}$ within one radiation pulse. This corresponds to an absorption of $\sim 50 \, \mathrm{photons}$. At this power density the FEL delivers $\sim 6 \times 10^{17} \, \mathrm{photons/cm^2}$ during the radiation pulse. If it is assumed that the absorption is due to sequential processes a rough estimate for an average cross section can be made and the average single photon cross section per atom $\bar{\sigma}$ is calculated by:

$$\bar{\sigma} = 84 \, Mbarn/atom \tag{3.26}$$

Here the possible influence of space charge effects is not included in the calculation of the mean ejection energy $\bar{E}_{ej}$ and the cross section $\bar{\sigma}$ per atom. The discussion of space charge effects in Appendix A indicates that space charge effects may have to be taken into account. Therefore the influence of space charge as well as other experimental uncertainties such as the focal spot size and the radiation pulse length are discussed in section 3.3.7.
The average charge state $\bar{z}$ is not affected by the above mentioned experimental uncertainties.

3.3.6.4 Absorption mechanisms

In the following the absorption mechanism will be discussed. The strong absorption can not be explained by single photon ionisation of Xe atoms. Although 24 photons per pulse ($E_p = 5 \, \mu\mathrm{J}$) fall into the absorption cross section ($40 \, \mathrm{Mbarn}$) for the initial ionisation, the energy of a single photon is not sufficient to excite or ionise further Xe ions inside the cluster. Therefore, other absorption mechanisms have to be taken into account.
In the next paragraphs the contributions of different absorption mechanisms will be studied.

Inverse bremsstrahlung

The *nanoplasma model* proposes that the energy absorption is mainly due to *inverse bremsstrahlung* (IB). In the process IB an electron can gain energy from the radiation field after scattering elastically with an ion. Thereby the electron is de-phased or in other words, after the collision the velocity of the electron is changed in direction. If now the electric field of the laser points favourably in the opposite direction (negatively charged electron), it accelerates the electron. In this way the electron absorbs energy

from the laser field. For comparison, without a de-phasing collision the electron follows the laser electric field from the beginning of the pulse until its end. In the same way the electron gains energy while the electric field increases, it loses energy in the decreasing second half of the pulse and no net energy absorption occurs.

The energy absorption in the cluster was calculated according to the model proposed in [49]. The model assumes the cluster as a dielectric sphere. The time derivative of the energy density in the laser field (in other words the damping rate) is then taken as the energy deposition rate in the cluster. In the following, the laser field surrounding the cluster is approximated as constant over the cluster dimensions, because the wavelength of the radiation is much larger than the diameter of the cluster. By using a simple Drude model for the dielectric constant the energy absorption rate per unit volume in the cluster is:

$$\Delta U = 4\pi\epsilon_0 \frac{9\omega_{FEL}^2\omega_p^2\nu_{ei}}{8\pi\left(9\omega_{FEL}^2\left(\omega_{FEL}^2+\nu^2\right)+\omega_p^2\left(\omega_p^2-6\omega_{FEL}^2\right)\right)}E_0^2 \tag{3.27}$$

where E_0 is the electric field strength of the laser in vacuum, ω_{FEL} is the frequency of the FEL radiation and $\omega_p = \sqrt{e^2zn_i/\epsilon_0m_e}$ denotes the plasma frequency with n_i and z the ion density and the charge state of the ions, respectively. According to [69] the electron-ion collision frequency ν_{ei} is calculated by

$$\nu_{ei} = \frac{4(2\pi)^{1/2}z^2e^4n_i}{3m_e^{1/2}(kT_e)^{1/2}}\ln\Delta\cdot\left(\frac{1}{4\pi\epsilon_0}\right)^2 \tag{3.28}$$

when the oscillation velocity is much smaller than the thermal velocity. Assuming a thermal energy $3/2kT_e = 10\,\mathrm{eV}$ for the excited electrons in the cluster this condition is fulfilled because the ponderomotive energy of the electrons is much smaller($\sim$150 meV). $\ln\Delta$ denotes the standard Coulomb logarithm [70].

The parameters are explained in the following table.

ϵ_0	dielectric constant	$= 8.85 \times 10^{-12}\frac{A^2s^4}{m^3kg}$
n_i	ion density (solid density)	$= 1.72 \times 10^{28}m^{-3}$
n_e	electron density	$= z \cdot n_i$
z	charge state of ion	$= 1$
$\frac{3}{2}kT_e$	thermal energy of electrons	$= 10 \cdot 1.602 \times 10^{-19}J (= 10eV)$
$\frac{3}{2}\tau$	thermal energy of electrons in K	$= 10 \cdot 1.160 \times 10^4 K (= 10eV)$
$\ln\Delta$	standard Coulomb logarithm;	$= 1.24 \cdot 10^7 \cdot \frac{\tau^{3/2}[K]}{\sqrt{n_e}[m^{-3}]}$
λ_{FEL}	wavelength of FEL radiation	$98 \times 10^{-9}m$
ω_{FEL}	frequency of FEL radiation	$= 1.92 \times 10^{16}s^{-1}$
ω_p	plasma frequency	$= \sqrt{\frac{e^2n_e}{\epsilon_0m_e}} = 7.399 \cdot 10^{15}s^{-1}$
P_{FEL}	power density of FEL	$= 2.5 \times 10^{13}W/cm^2$
E_0	electric field strength of FEL	$= 2740\sqrt{P_{FEL}} = 1.4 \times 10^{10}V/m$

For the calculation the situation in the cluster after the first few femtoseconds of the radiation pulse is regarded: Each atom has lost one electron by single photon absorption. The corresponding electrons have not left the cluster yet. Additionally, the expansion of the cluster has not started. In this situation the density of ions n_i in the clusters is the same as the atomic density of solid xenon.

Calculating the electron-ion collision frequency ν_{ei} with the given parameters yields $\nu_{ei} = 2.05 \times 10^{15} \, s^{-1}$.

Using this result one obtains for the energy absorption of an electron during a laser pulse of 50 fs length

$$\Delta U = 10 \, eV \qquad (3.29)$$

This corresponds to an average cross section of $\bar{\sigma} = 1.3$ Mbarn/atom.
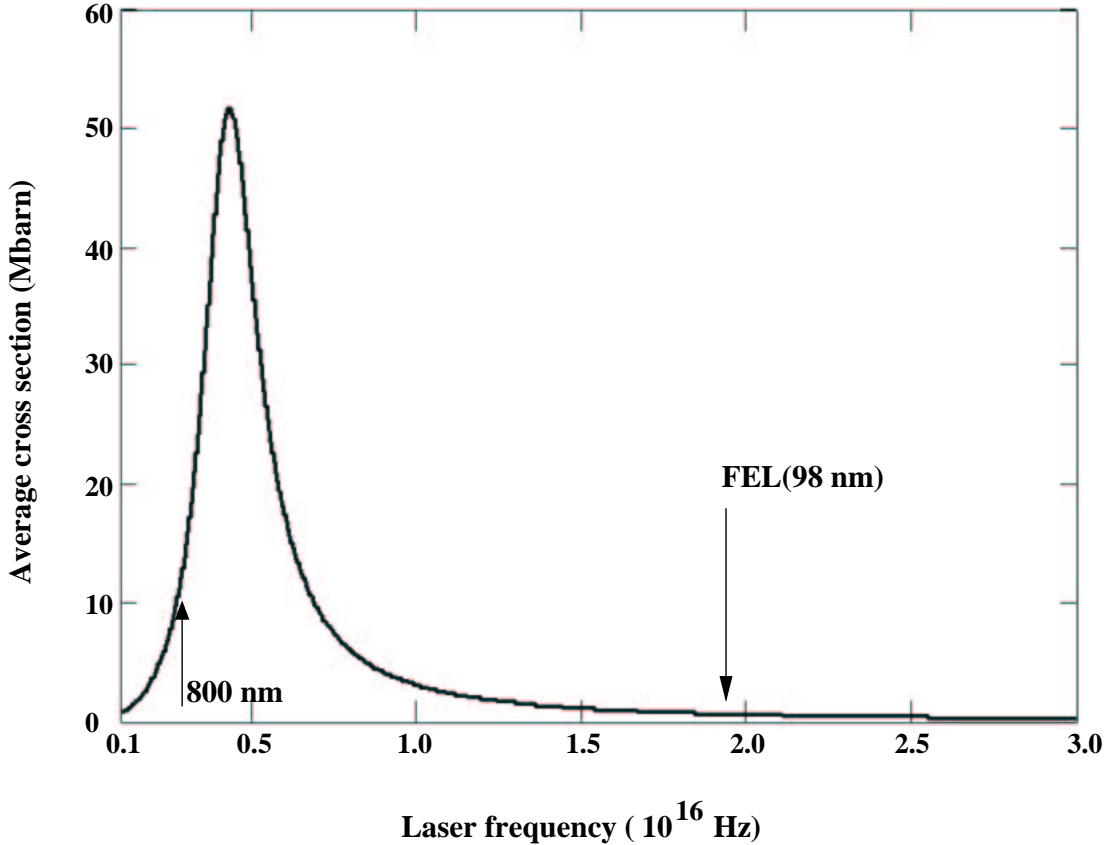

Figure 3.17: Cross section of inverse bremsstrahlung as a function of laser frequency. Parameters are average ionic charge state $\bar{z}{=}1$, thermal energy of the electrons $3/2kT_e = 10$ eV and power density P$=2.5\times10^{13}$ W/cm^2. Frequencies of FEL (98 nm) and optical laser (800 nm) are indicated by arrows.

For the situation described above the average cross section is given as a function of the laser frequency ω in Figure 3.17. For comparison, the much higher cross section

belonging to 800 nm radiation at the same power density is marked. As stated above, the energy an electron absorbs in a collision with an ion is on average equal to the ponderomotive energy. The strongly reduced ponderomotive energy at 98 nm is one reason for the low cross section.

In the following, the dependence of the absorption rate ΔU on the collision frequency ν_{ei} is discussed. There is maximum electron-ion collision frequency $\nu_{ei,max}$ which is a function of the thermal velocity of the electron and the inter ionic distance. Assuming a Maxwellian distribution the most probable velocity of the electron is $v_{th} = \sqrt{2kT_e/m_e}$, which results for the chosen thermal energy of 10 eV in $v_{th} = 15.3$ Å/fs. Taking the inter ionic distance to be 4.33 Å for solid xenon the collision frequency becomes $\nu_{ei,max} \simeq 4 \cdot 10^{15}\,s^{-1}$. This limit is reached for the experimentally observed average ionic charge Z=3 and the calculated cross section becomes $\bar{\sigma} = 8.8$ Mbarn. Therefore, the calculated cross section for an average charge state $\bar{z}$=3 is only about one ninth of the experimentally observed cross section $\bar{\sigma} = 84$ Mbarn. Average cross sections for charge states z=1-3 and two different thermal electron energies are given in Table 3.4. All cross sections are well below the experimentally observed cross sections. As a result, absorption due to IB does not appear to be sufficient to explain the experimental observations.

To complete the picture it is further stated that $\nu_{ei,max}$ is a function of v_{th} and increases with increasing thermal energy of the electrons. Here the limit is the frequency of the driving laser field of the FEL. But for $\nu_{ei} \sim \omega_{FEL}$ it would need $kT_e = 215$ eV and an average ionic charge state of $z = 14$, what is in contradiction to the experimentally observed value of z=3.

Plasmon absorption

Another way to couple energy from laser field into the cluster lies in the excitation of plasmon oscillations. The plasmon oscillation is a collective motion of the electron gas, in which the light electrons oscillate relative to the heavy ions. The *plasma frequency* (eigenfrequency) in a homogenous solid is given by $\omega_p = \sqrt{\frac{e^2 n_e}{\epsilon_0 m_e}}$. Assuming the cluster as a small dielectric sphere the plasma frequency is reduced by a factor of $1/\sqrt{3}$ and the eigenfrequency of the *surface* or *Mie plasmon* becomes:

$$\omega_{Mie} = \frac{1}{\sqrt{3}} \cdot \sqrt{\frac{e^2 n_e}{\epsilon_0 m_e}} \tag{3.30}$$

Apparently the coupling of the laser field becomes resonant for $\omega = \omega_{Mie}$, where ω is the frequency of the driving laser field. The energy absorption of the cluster results from the damping of this oscillation. Following [71] the absorption cross section σ of metallic clusters as a function of the laser frequency ω is given by

$$\sigma(\omega) = \frac{n_e e^2}{\epsilon_0} \cdot \frac{\omega^2 \Gamma(T_e, R)}{m_e c \left(\left(\omega^2 - \omega_p^2\right) + (\omega\Gamma)^2 \right)} \cdot 10^{22} \tag{3.31}$$

where $\Gamma(T_e, R)$ denotes the electron temperature and cluster radius dependent damping factor. According to [72] the damping factor is a sum of two contributions $\Gamma(T_e, R) = \gamma_0(T_e) + \gamma_s(T_e, R)$. The first contribution $\gamma_0 = v_F/l_e$ is the damping corresponding to free-electron metals, where v_F is the Fermi velocity and l_e the mean free path of electrons in bulk material. The second contribution $\gamma_s = Av_F/R$ takes into account the interactions of the conduction electrons with the cluster surface as an additional scattering process when the size of the cluster is comparable to l_e [72]. At an electron kinetic energy around $10\,\mathrm{eV}$, l_e is on the order of $50\,\text{Å}$ [73, 74] and this condition is certainly fulfilled. For a conservative estimate the constant A, was chosen to be A=0.5 in the present case, see also below.

In Figure 3.18 the absorption cross section resulting from plasmon absorption is given as a function the laser frequency for a Xe_{2500} cluster and an average ionic charge state of $\bar{z}=1$. At a frequency corresponding to $800\,\mathrm{nm}$ radiation the cross section is about $10\,\mathrm{Mbarn}$. At the frequency of the FEL radiation the cross section is strongly reduced to $\sim 0.2\,\mathrm{Mbarn}$ (logarithmic scale!).
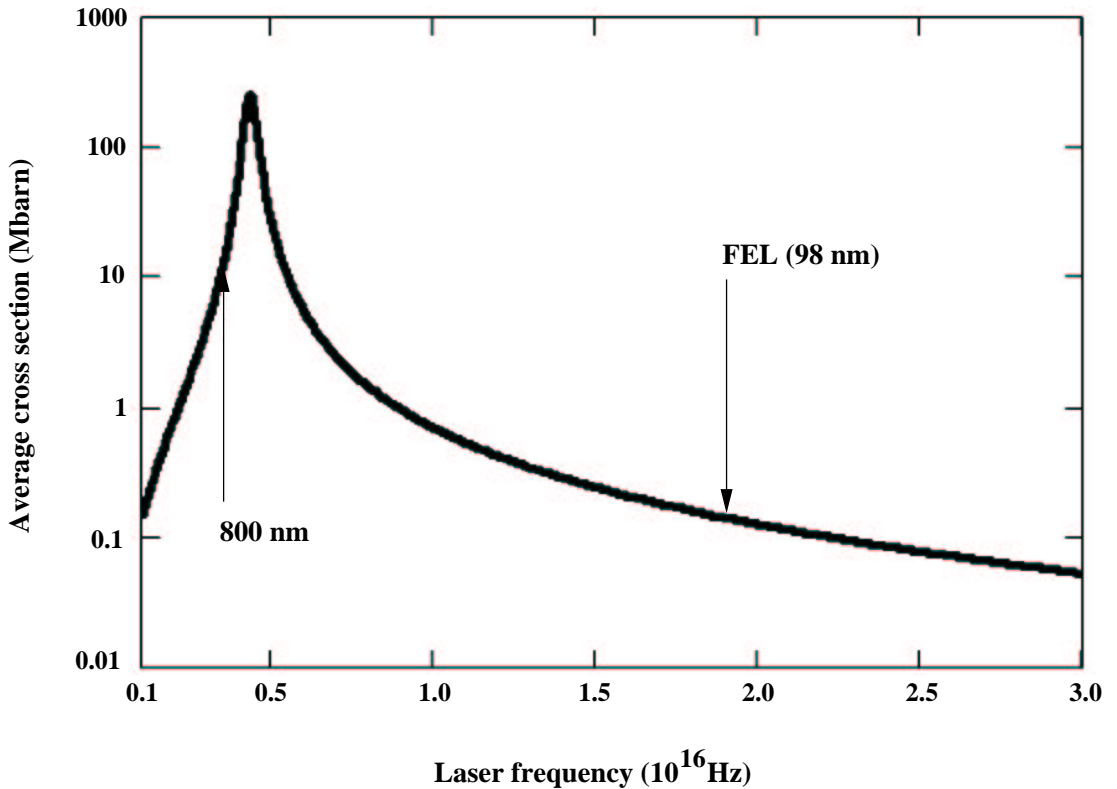

Figure 3.18: Plasmon absorption cross section for a $(Xe)_{2500}$ cluster as a function of laser frequency for the situation of one free electron per atom. Parameters are average ionic charge state $\bar{z}=1$, thermal energy of the electrons $3/2kT_e = 10\,\mathrm{eV}$ and power density $P=2.5\times10^{13}\,\mathrm{W/cm^2}$. Frequencies of FEL ($98\,\mathrm{nm}$) and optical laser ($800\,\mathrm{nm}$) are indicated by arrows. The cross section at $98\,\mathrm{nm}$ is only ~ 0.2 Mbarn (logarithmic scale!).

Equation (3.31) assumes a 'metallic' cluster with free conduction electrons. This assumption seems valid, since in the FEL experiment valence electrons in the Xe clusters are promoted during the first femtosecond of the radiation pulse to excited states (conduction band), see preceding paragraph *inner ionisation*. However, the choice of A=0.5 probably overestimates the absorption, because the quivering amplitude X_0 due to the oscillation in the FEL radiation field is very small $(X_0 \sim 0.06\,\text{Å})$[7] compared to the radius R of the cluster (R=32.6 Å) in the present case of a Xe_{2500} cluster. The number of electron-surface collisions is therefore limited. Results of the calculated plasmon absorption cross sections for different electron temperatures and densities are given in Table 3.4. All calculated cross sections are more than 10 times smaller than the experimental observed one. The explanation for the inefficiency of plasmon absorption is, that in our case ω_{FEL} is always larger than ω_{Mie} and therefore no resonantly enhanced absorption occurs, see Table 3.6 for energetic positions of Mie surface plasmons.

	$3/2kT_e$=1.5 eV		10 eV		100 eV	
charge z	plasmon	IB	plasmon	IB	plasmon	IB
1	0.13	-	0.20	1.3	0.49	0.25
2	0.30	-	0.44	5.5	1.09	2.0
3	0.51	-	0.74	8.8	1.55	7.0

Table 3.4: Calculated cross sections in Mbarn for plasmon absorption and inverse bremsstrahlung IB. The cross sections belong to three different electron temperatures kT_e and average ionic charge states z.

Classical simulation of electron motion

The simulation [68] described in Section 3.3.6.1 should include the classical processes of IB and plasmon absorption. To compare the results with that in the preceding section the time dependent development of the energy absorption of the electron gas is investigated. In Figure 3.19 the total energy of 55 unbound electrons in a $(Xe^+)_{55}$ cluster is shown as a function of laser pulse duration. The power density of the laser was set to $5 \times 10^{13}\,\text{W/cm}^2$, slightly higher than in the actual experiment. At 98 nm laser wavelength the 55 unbound electrons absorb an energy of $\sim$800 eV in total during the laser pulse duration of 50 fs, or each electron absorbs on average 14.5 eV($\sim$ 1.1 FEL-photons) during the laser pulse. Since the FEL delivers $\sim 1.2 \times 10^{18}$ photons/cm^2 in one radiation pulse at $5 \times 10^{13}\,\text{W/cm}^2$, the number of 1.1 absorbed photons results in an average cross section of $\sim$ 1 Mbarn. The approximately linear increase shows that the absorption is hardly changing with the electron temperature. At $2.5 \times 10^{13}\,\text{W/cm}^2$ results for different simulation parameters are summarised in Table 3.5. The cross

---

[7]The quivering amplitude is calculated by $X_0 = eE_0/m_e\omega_{FEL}^2$, where E_0=1.4×10^{10} V/m is the peak electric field strength and $\omega_{FEL} = 1.92 \times 10^{16}\,\text{s}^{-1}$ is the frequency of the FEL radiation.

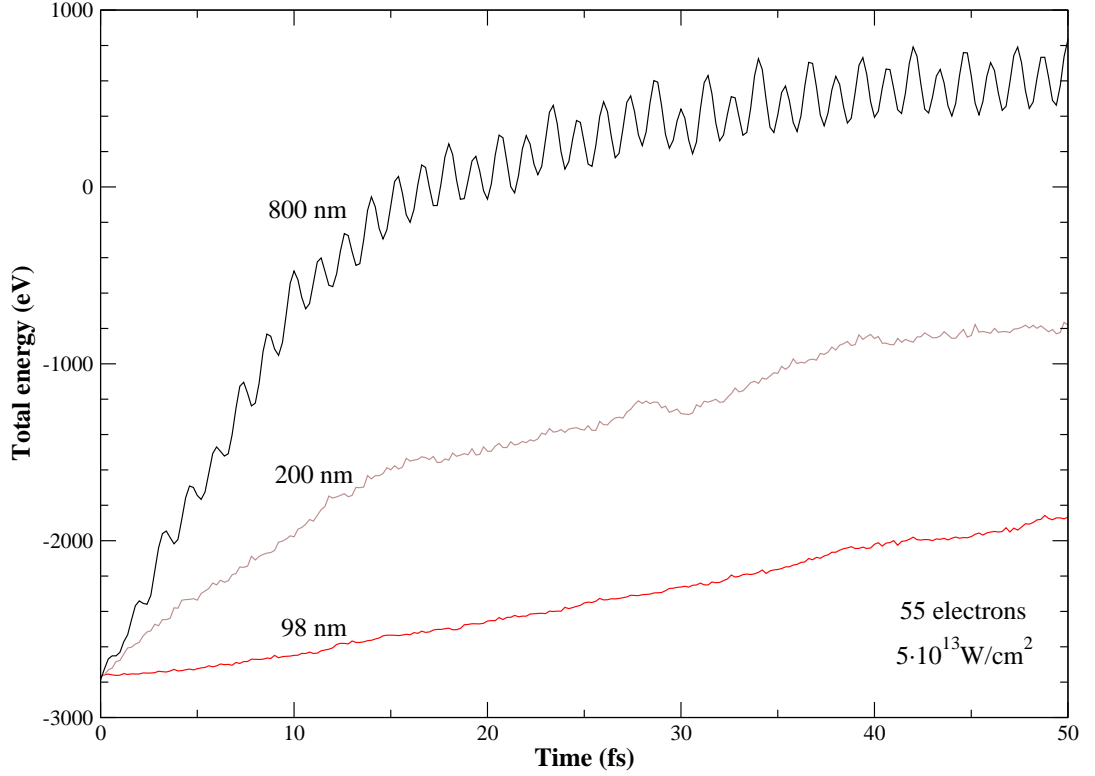**Figure 3.19:** Energy absorption of 55 unbound electrons in a Xe_{55} cluster under the influence of a laser-field at $5 \times 10^{13}\,\mathrm{W/cm^2}$. Absorption calculated with a classical simulation of electron motion [68] for three wavelengths. At 800 nm the total energy fluctuates with the oscillation frequency of the driving laser field. Absorption is most efficient at the optical wavelength 800 nm. At 98 nm the absorption is strongly reduced. The total amount of energy absorbed in 50 fs allows for determination of average atomic cross section.

sections increase strongly with increasing density of unbound electrons. For the situation of one unbound electron/atom (Figure 3.19) the absorption cross section is about 1 Mbarn. Doubling the electron density to two unbound electrons/atom increases the cross section to 2.8 Mbarn. However, the experimental value of 84 Mbarn is not reached even for an experimentally not observed high density of six electrons per atom.

	$(Xe^{1+})_{13}$	$(Xe^{1+})_{55}$	$(Xe^{2+})_{55}$	$(Xe^{6+})_{55}$
unbound electrons	13	55	110	330
absorption $\left[\frac{eV}{50\,fs\,atom}\right]$	16	26	68	374
cross section $\bar{\sigma}\,[Mbarn]$	0.5	1.0	2.8	16.6

Table 3.5: Simulated energy absorption and cross section for different electron densities at $2.5 \times 10^{13}\,\mathrm{W/cm^2}$.

Two additional simulations for wavelengths in the optical and ultraviolet spectral range are shown in Figure 3.19. As expected the absorption at 800 nm is strongly enhanced compared to 98 nm. The absorption is also more efficient than at a wavelength of 200 nm. This situation changes clearly, when the density of free electrons is increased to six electrons per atom.
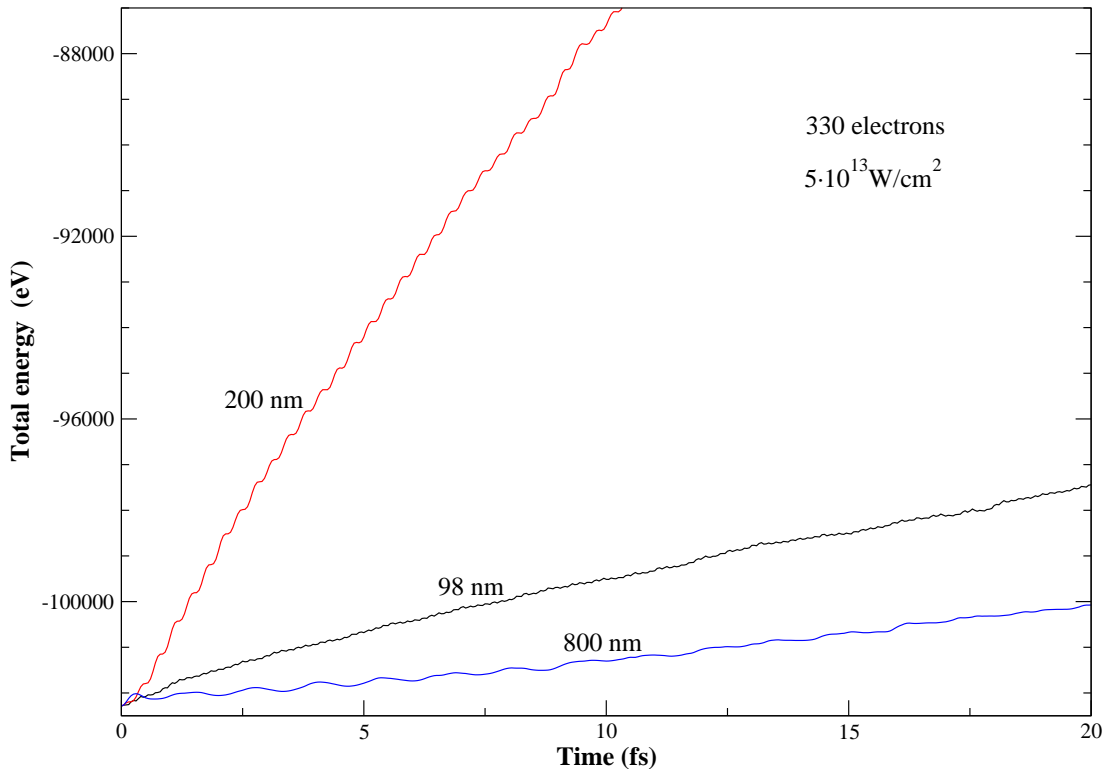

Figure 3.20: Energy absorption of 330 unbound electrons in a Xe_{55} cluster under the influence of a laser-field at 5×10^{13} W/cm^2. Absorption calculated with classical particle simulation [68] for three wavelengths. Due to high density of unbound electrons (6 e$^-$/atom) absorption is most efficient at 200 nm.

In Figure 3.20 results of simulations with 330 free electrons in a $(Xe^{6+})_{55}$ cluster are illustrated. Now the energy absorption is most efficient at 200 nm and the absorption at 98 nm is even higher than at 800 nm. This behaviour is in agreement with the recent theoretical work of Last and Jortner [59]. The strong wavelength dependent resonance can be explained by oscillations of unbound electrons in the cluster and plasmon absorption. As the electron density increases the plasma frequency $\omega_p \propto \sqrt{n_e}$ is shifted to higher values and likewise the resonance condition $\omega_p/\sqrt{3} = \omega_{laser}$ occurs at shorter wavelengths. In Table 3.6 some values of the Mie surface plasmon energy are calculated for different average ion charge states $\bar{z}$. Increasing $\bar{z}$ from 1 to 6 changes the wavelength for resonant absorption from 443 nm to 180 nm, which is in accordance with the change of the more efficient absorption at 800 nm in Figure 3.19 to 200 nm in Figure

3.3. XENON CLUSTERS

3.20. But in spite of the increase of the resonant photon energy, all values in Table 3.6 are well below the photon energy of the FEL. Furthermore, for the calculations in Table 3.6 the cluster geometry was assumed unchanged. However, it is quite likely that the cluster expands before the average charge state $\bar{z}$ is reached (see section 3.3.4). In this way the reduction of the electron density would result in a even stronger discrepancy between resonant and FEL photon energy.

aver. charge state $\bar{z}$	1	2	3	4	5	6
$\hbar\omega_p/\sqrt{3}$ [eV]	2.8	4.0	4.9	5.6	6.3	6.9
res. wavelength [nm]	443	310	255	220	197	180

Table 3.6: Energy of Mie surface plasmon for different electron densities. The energy of the plasmon increases with increasing electron density, but is for all values of the average ionic charge state well above the wavelength of the FEL.

3.3.7 Discussion

A significant result of the ionisation of Xe clusters with intense VUV radiation is the unexpectedly high energy absorption. The aim of the following discussion is to estimate the experimental errors in the determination of absorption of the clusters. Then the experimental results will be compared with the theoretical predictions from the models presented in the preceding section.

One experimental error is the potential influence of space charge due to the ionisation of many clusters in the interaction region on the kinetic energy of the ions charge states resulting from the ionisation of clusters. Space charge effects are estimated in detail in Appendix A. The result of a simple electrostatic model indicates that the influence of space charge can be quite strong. However, two observations show that the contribution to the ion kinetic energy due to space charge is by far not the leading contribution. First, the ion ejection energies in Figure 3.10 show a clear quadratic dependence on the ion charge state, which is in clear contrast to a linear scaling due to space charge. Second, experiments on Ar clusters show very similar results [75], ions are ejected with kinetic energies up to $3\,\mathrm{keV}$. On the other hand, the skimmer transmission for argon is substantially lower, so that space charge effects can be neglected. If a conservative estimate is made that one third of the measured ejection energy of Xe^+ is due to space charge effects, then the ejection energies of the ion charge states would be reduced by $30\,\mathrm{eV}$ per charge. This results in a reduction of the mean ejection energy calculated in section 3.3.6.3 to $\sim 550\,\mathrm{eV}$ per atom, a reduction of a mere $\sim 14\,\%$

For a comparison of the experimental results with the theoretical predictions the experimental uncertainties in the determination of the power density have to be taken into account. In the following the errors for the focal spot size as well as the radiation

classical simulation	$(Xe^{1+})_{55}$	$(Xe^{2+})_{55}$		$(Xe^{6+})_{55}$
unbound electrons	55	110		330
absorption $[\frac{eV}{50\,fs\,atom}]$				
at 3.5×10^{13} W/cm^2	11	29.5		172
at 1.5×10^{13} W/cm^2	4.5	13.4		85
inverse brems. (IB)	z=1	z=2	z=3	
absorption $[\frac{eV}{50\,fs\,atom}]$				
at 3.5×10^{13} W/cm^2	7	30	47.4	
at 1.5×10^{13} W/cm^2	3	12.4	20.3	

Table 3.7: Error estimation for the determination of the energy absorption. For the experimental observed average charge state $\sim \bar{z} = 3$ the calculated values are a factor of 11-25 lower than the space charge corrected experimental absorption of 550 eV. Details see text.

pulse length are estimated and included in two theoretical models.

The procedure to determine the focal spot size is described in section 2.3.3. It is assumed that $r = 10\,\mu$m$\pm 1\,\mu$m, where r is the radius of the focus. The radiation pulse length of the FEL could not be measured directly, but was estimated from statistical and spectral properties, see section 2.1.6. Following the considerations in [5], the error in the pulse length is estimated by 50 fs$\pm$20 fs. Using standard error propagation the power density becomes $P_{FEL} = (2.5 \pm 1.0) \times 10^{13}$ W/cm^2. The mean ejection energy was calculated in section 3.3.6.3 at $P_{FEL} = 2.5 \times 10^{13}$ W/cm^2.

In Table 3.7 the energy absorption per atom for the power densities 3.5×10^{13} W/cm^2 and 1.5×10^{13} W/cm^2 due to inverse bremsstrahlung (IB) is given and additionally the results of the classical simulation. For the experimentally observed average charge state $\bar{z} \sim 3$ the values in Table 3.7 are are at least one order of magnitude lower than the space charge corrected experimental absorption of 550 eV per atom. This indicates, that the process of inverse bremsstrahlung and the classical simulation underly systematic shortcomings and therefore cannot fully account for the absorption seen in the FEL experiment. According to recent theoretical work, the absorption of a cluster plasma confined by a strong Coulomb potential is enhanced compared with that of an infinite plasma [76]. The enhancement is due to collisions of the electrons with the whole cluster ion, an effect which is not included in the conventional IB model. In the classical simulation an increase of the absorption was observed for increasing cluster size. Whether this effects can explain the enhanced absorption could be checked by simulations for larger clusters. Finally, according to very recent theoretical work non Maxwellian electron distributions can contribute to enhanced absorption [77].

In addition I would like to note, that the simulation treats the electrons as classical particles which are driven by a plane wave. This simplification neglects intermediate states in the highly charged cluster ion, which may resonantly absorb FEL photons.

The energy of the FEL photons is of the same order of magnitude as the level spacing in Xe atoms and Xe ions. Therefore it is quite likely that a quantum mechanical description including resonant intermediate states could give larger absorption than the classical simulation.

3.4 Photoelectrons of xenon atoms and clusters

3.4.1 Introduction

Photoelectron spectra can give a complementary and more detailed view of non-linear processes of atoms and clusters in intense laser fields. In clusters, for example, the observation of very energetic electrons up to 3 keV after irradiation with intense laser radiation supported the nanoplasma model [78]. In the following, photoelectron spectra of Xe atoms and clusters are presented. The distribution after irradiation of Xe clusters indicates a kind of thermionic ionisation process, as it is proposed by the simulation results in section 3.3.6.3.
The results presented in the following paragraph give some additional information on the ionisation process. As a consequence of very limited beam-time only a few measurements could be performed.

3.4.2 Photoelectron spectra

Time-of-flight (TOF) photoelectron spectra were taken with the bi-polar TOF spectrometer described in section 2.3.2. A pull-in voltage of 10 V was applied across the interaction volume to increase the count rate. The measured electron yield per time interval (dI/dt) was converted into electron yield per kinetic energy interval (dI/dE), recalling that $dI/dE \propto t^3 \cdot dI/dt$ [79]. In the calculation of the kinetic energy the contribution from the pull-in voltage was subtracted.
In Figure 3.21 photoelectron spectra of Xe atoms and clusters are given. In both spectra the background resulting from electrons of residual gases and due to electrons from metal apertures was subtracted and the spectra were converted to energy scale. Due to a low count rate the spectra represent the averages of 100 subsequent single-shots. In this case only an average power density of the FEL can be estimated, which is given in each spectra. In the top spectrum, the dominant peak belongs to electrons resulting from the single photon ionisation of neutral Xe atoms. The measured energy of ~ 0.7 eV is slightly lower than expected from $E_{kin} = \hbar\omega_{FEL} - I_p \sim 0.9$ eV, where I_p is the first ionisation potential of Xe atoms (~ 12.1 eV). At higher kinetic energies no significant features are visible. The lower spectrum displays the kinetic energy distribution of electrons resulting after the irradiation of Xe clusters ($N \sim 70$). The distribution starts at zero energy and then reveals an exponential decay up to about 30 eV kinetic energy. The dip in the distribution at ~ 0.9 eV results from the subtraction of the background and is an experimental artefact. While the cluster source nozzle is closed, Xe atoms are still among the residual gases. As in the atomic spectrum, the background spectrum reveals a signal from electrons at ~ 0.9 eV. Now with expanding a cluster beam through the nozzle the Xe atoms in the interaction region belonging to the background are re-

placed by clusters and a distinct atomic signal is lacking in the spectrum. Therefore a subtraction of the two different spectra generates the observed dip.
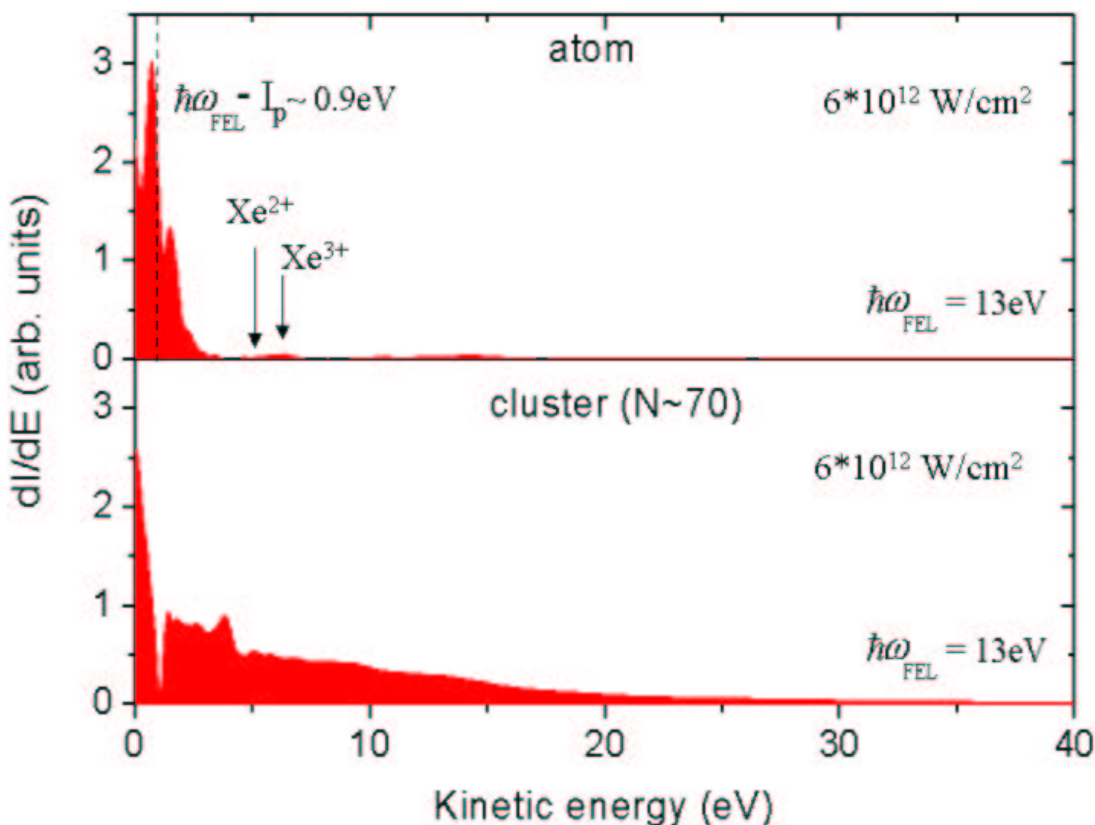

Figure 3.21: Photoelectron spectra of Xe atoms and clusters. The photoelectrons in the top spectra result after irradiation of an atomic beam of xenon at a pressure of 35 mbar. The significant peak at ~ 0.7 eV belongs to single photon absorption of neutral Xe atoms. It is slightly shifted with respect to the theoretical position which is indicated by the dashed line. The theoretical positions of photoelectrons resulting from stepwise MPI of Xe^+ and Xe^{2+} (5 eV and 6.9 eV) are indicated by arrows. The production rate is >0.5 % than that of the single photon ionisation of neutral Xe atoms. The kinetic energy distribution of electrons after irradiation of clusters(N=70, pressure=1 bar) in the bottom spectrum starts at zero kinetic energy and decays exponentially to about 30 eV. The observed dip in the distribution is due to an experimental artefact, for explanation see text. Both spectra are averages of 100 subsequent single shots. Corresponding average power densities are given in each spectrum.

3.4.3 Discussion

In the atomic photoelectron spectrum only the peak from electrons liberated from neutral Xe atoms by single photon absorption is visible. Electrons resulting from stepwise

MPI of Xe^+- Xe^{4+} at higher kinetic energies (5 eV, 6.9 eV, 5.3 eV and 5.3 eV respectively) are absent in atomic spectrum. The very low, unresolved structure around 5 eV in the spectrum is most probably an artefact due to subtraction of the background spectrum.

In any case, the production of photoelectrons corresponding to the ionisation of multiple ion charge states is smaller than 0.5 % of the counting rate of electrons from neutral Xe atoms. This might give a straightforward explanation for the absence of multiple ion charge states in the atomic TOF mass spectrum recorded with the cluster ion TOF, see lowest trace in Figure 3.8. The recordings of the cluster ion TOF spectrometer show a noise level of ∼1 %, so that the detection of multiple charge states might be hidden in the noise. That the recordings with the bi-polar TOF spectrometer show the multiple ion charge states, indicates the enhanced sensitivity of the bi-polar MCP detector.

The absence of photoelectrons from multiple charge states can be explained by the much lower cross sections of MPI processes, compared to the single photon ionisation of neutral Xe atoms. The relative ion intensity of for example Xe^{3+} with respect to Xe^+ in Figure 3.3 cannot be taken as a measure of the reduced cross section, because the MCP detector is saturated for Xe^+. However, a comparison of the saturation power densities of Xe^+ and Xe^{3+} can illustrate the large difference in the respective electron production rates. The saturation power density of Xe^+ ($< 10^{12}$ W/cm^2) is about two orders of magnitude smaller than for Xe^{3+}. Therefore Xe^+ results from a much bigger interaction volume than Xe^{3+} whose production is limited to a much smaller volume (focal spot), see also discussion of saturation power density P_s in section 3.2.2 and section 3.2.3.

The photoelectron spectrum after irradiation of Xe clusters with an average size of $\bar{N} \sim 70$ reveals an exponentially decaying distribution of 'cold electrons' starting at zero kinetic energy and vanishing count rate at about 30 eV. The maximum of the distribution at very low kinetic energies shows, that the electrons leave the cluster as soon as they overcome the Coulomb potential of the charged cluster. On the other hand, the distribution is not limited to kinetic energies $E_{kin} \leq \hbar\omega \sim 13$ eV. This is a clear indication, that outer ionisation (see section 3.3.6.1) is not due to excited electrons in the cluster which are finally liberated by absorption of a photon. Quite the contrary, the behaviour that a significant fraction of electrons exceed the photon energy but the maximum kinetic energy of about 30 eV is relatively low indicates, that before outer ionisation the electrons undergo many scattering events. This observation points to a outer ionisation process, which can be described as a thermionic emission. A kind of thermionic emission is also in accordance with the simulation results presented in section 3.3.6.1, that electrons leave the cluster only after many scattering events and the angular distribution is isotropic.

The experimental findings are remarkably different from what was found in experiments with intense IR-lasers. In [78] Xe clusters of $\bar{N} = 2100$ were irradiated with a 800 nm laser at $\sim 2{\times}10^{16}$ W/cm^2. Energetic electrons up to 3 keV were detected.

The kinetic energy distribution shows two different peaks. The first is referred to as 'warm' electrons around 900 eV and the second peak ('hot electrons') is located around 2400 eV. Simulation of the authors indicated that the 'warm electrons' are produced at the beginning of the laser pulse near the surface of the cluster. They are emitted very fast and preferentially along the laser polarisation axis. 'Hot electrons' on the other are generated later and leave the cluster after many collisions in random directions. The authors state that the experimental findings can be explained in the nanoplasma model (see section 3.3.6). Although the clusters in [78] are significantly larger and the power density is two orders of magnitude higher, the findings in the present FEL-experiment seem qualitatively different. Field ionisation processes or the generation of a 'hot' electron gas cannot account for the electron distribution of outer ionisation in the present experiment.

Chapter 4

Summary and outlook

The interaction of intense, short wavelength radiation from a VUV free-electron laser (FEL) with rare gas atoms and clusters is investigated. Clusters serve as a model substance of condensed matter, which allow continuous sample renewal.

As one of the first experiments performed with DESY's short-wavelength FEL many experimental requirements were new. For example, performing the experiment under clean room conditions and the fully remote controlled operation of the equipment had to be fulfilled, because the set-up was situated inside the main accelerator tunnel, not far away from the superconducting acceleration modules of the FEL driving linear accelerator.

The experimental results in this work consist of three parts. In the first part, the ionisation of Xe and Ar atoms is investigated. Irradiation with FEL light at highest power density ($\sim 1 \times 10^{13}\,\mathrm{W/cm^2}$) shows strong ionisation up to ion charge states of Xe^{6+} and Ar^{4+} in the ion mass spectra. Reducing the power density of the FEL light results in the rapid vanishing of higher ion charge states, what highlights the clearly nonlinear nature of the ionisation process. The occurrence of multiple ion charge states as a function of the power density reveals that the ionisation is due to sequential absorption of FEL photons of each atom. Furthermore, the order of the multiphoton processes indicates that the ionisation proceeds in a 'stepwise' manner, i.e. it is due to a so-called 'stepwise' multiphoton ionisation (MPI) process.

The main scientific part of this present work is the investigation of the interaction of intense short wavelength radiation with clusters. An important result is that the absorption in cluster beams is strongly enhanced as compared to atomic beams. At comparable power densities the cluster completely disintegrates and ion charge states up to Xe^{8+} with high kinetic energies up to $3\,\mathrm{keV}$ are detected. Variation of the power density clearly demonstrates the nonlinear nature of the absorption process. A comparison of different cluster sizes indicates a more efficient absorption in bigger clusters. The high ion kinetic energies and the complete disintegration results from Coulomb explosion of the highly charged cluster. In this way, the energy absorbed from the FEL

beam is released. Coulomb explosion of the clusters begins at a power density as low as $10^{11}\,\text{W/cm}^2$, which is approximately two orders of magnitude lower than the threshold for such a process in optical laser experiments.

In the following, a model for the ionisation and expansion of the cluster is proposed. In a first step, atoms in the cluster are ionised efficiently by single photon absorption. Therefore it is assumed that after a few fs a nanoscale plasma is formed, which is confined in the cluster. Once a large number of electrons has left the cluster, the highly charged cluster starts to expand. The expansion lowers the confining Coulomb potential and ionisation of loosely electrons is eased ('outer ionisation').

From the ion kinetic energies resulting from the Coulomb explosion it can be estimated, that in a Xe_{2500} cluster each atom absorbs $\sim 550\,\text{eV}$ at $P_{FEL} = 2.5 \times 10^{13}\,\text{W/cm}^2$, corresponding to a large number of ~ 43 VUV photons. Theoretical predictions of classical processes such as inverse bremsstrahlung (IB), plasmon absorption and a classical simulation of electron trajectories reveal cross sections which are a factor of more than three lower than the experimental value. The enhanced absorption might be due to three different effects:

1) resonant intermediate states

2) non-thermal electron distribution with a large fraction of low energy electrons

3) inverse bremsstrahlung collisions with the whole cluster

In the third part of this work initial photoelectron spectra of Xe atoms and clusters irradiated with intense VUV pulses of the FEL are presented. They give insight into the ionisation mechanism. Excitation of atomic beams reveals only electrons resulting from the ionisation of neutral Xe atoms. The absence of electrons resulting from the ionisation of Xe ions can be explained by the much lower cross section of multiphoton ionisation processes. Photoelectron spectra of Xe clusters show a distribution of 'cold' electrons peaking at zero kinetic energy and then exponentially decaying up to $\sim 30\,\text{eV}$. From the maximum around zero kinetic energy it can be concluded, that the electrons leave the Coulomb potential of the cluster as soon as they can escape from the Coulomb field. The detection of a significant fraction of electrons with higher kinetic energies than the photon energy indicates a photon assisted thermionic electron emission process. The conclusion that electrons are scattered many times before outer ionisation takes place is in accordance with results of the classical simulation.

At $100\,\text{nm}$ wavelength the results for clusters differ strongly from that obtained when optical light interacts with clusters. Coulomb explosion starts at two orders of magnitudes lower power densities. This is reasonable, because the photon energy exceeds the first ionisation potential of Xe atoms and thus the first ionisation is very efficient.

Field ionisation, the dominant process at optical frequencies, does not contribute to the ionisation of the clusters. On the other hand, it is concluded that field ionisation

by the static Coulomb field of the highly charged cluster accounts for the production of multiply charged atomic ions. Finally, at optical wavelengths the energy absorption can be qualitatively explained by the classical interaction of the laser electric field with a plasma. However, in the present FEL experiment, there is evidence that quantum mechanical processes may have to be included, in order to explain the efficient energy absorption of the FEL radiation.

In conclusion, this work presents first experimental results for the interaction of intense radiation with matter, in a spectral regime where the photon energy exceeds the ionisation potential. The experimental results can serve as a starting point for a large variety of future experiments, studying fundamental intense light-matter interaction at shorter wavelengths down to the Å regime. Recent theoretical work [80] indicates that in the X-ray regime the ionisation of clusters is less efficient than the ionisation of atoms. This is contrary to observations in the present study. The results can have important implications for the imaging of biological samples with X-ray FELs, because then the sample damage thresholds might be higher than originally expected. Therefore, the extension of atom/cluster investigations to higher photon energies is highly desirable. An upgrade of the experimental set-up is already under way to continue investigations at the second phase of TTF-FEL in 2004 down to 6 nm wavelength.
Investigations of the dynamics of the electron emission from the cluster ('outer ionisation') and the expansion dynamics of the cluster on a fs-timescale would further our understanding of the explosion dynamics of the cluster. Pump-probe techniques could be used to follow the electron emission and the expansion on fs-timescales. Thereby, as a pump-pulse the FEL would induce Coulomb explosion. The scattered light of a delayed FEL probe-pulse would then be used to monitor the dynamics. This would be an important step towards direct visualisation of electron and ion motion.

Appendix A

Calculation of space charge effects

Due to the high ionisation degree of atoms and clusters in the interaction zone of light and cluster beam the global charge build-up is calculated to estimate the possible influence of space charge on the ion kinetic energies.

In the following, first the number of atoms in an extended interaction volume is calculated. To this end the transmission characteristics of a skimmer has to be taken into account. Then the kinetic energy of ions resulting from the Coulomb repulsion is estimated in a simple electrostatic model of a cylindrical shaped space charge volume. The values of all parameters used in the calculations are summarised in Table A.1. They apply to a cluster size of Xe_{2500}.

The centre beam density of atoms in a free streaming nozzle expansion (this means without a subsequent skimmer) is proportional to the density in front of the nozzle n_0 and the open area of the nozzle. At a distance x the density is reduced by a factor $1/x^2$, because the nozzle can be regarded as a point source. The density of atoms at a distance x is given by [81]

$$n(x) = 0.157 \cdot n_0 \cdot \left(\frac{d_{eq}}{x}\right)^2 \tag{A.1}$$

where d_{eq} is the nozzle diameter and the n_0 can be calculated by $n_0 = p_0/kT$, where p_0 is the stagnation pressure and T is the temperature of the gas in front of the nozzle. With the values given in Table A.1 and at the distance of the focal spot beneath the entrance aperture of the TOF mass spectrometer x_f the density of atoms becomes $n_f = 1.8 \times 10^{20}\,\mathrm{m}^{-3}$.

The volume in which space charge can have an effect on the kinetic energy of ions is a cylindrical volume limited by the area of the focal spot, which has a diameter of $2a = 20\,\mu\mathrm{m}$ and the diameter of the entrance aperture of the TOF mass spectrometer described in section 2.3.1, which is $l = 1\,\mathrm{mm}$. With the parameters given in Table A.1

the number of atoms N_f in the extended focal volume is therefore $N_f = 5.7 \times 10^7$, if a skimmer transmission of 100% is assumed.

The transmission of a skimmer is dependent on the composition of the entering beam. For a beam of atoms the transmission decreases with increasing density at the location of the skimmer (increasing stagnation pressure p_0), because the mean free path of the atoms λ decreases and the increasing number of scattering events hinders the flow of the gas. On the other hand, the condensation of atoms into clusters reduces the number of scattering centres drastically. As a result, the transmission as a function of the stagnation pressure stays about constant from the onset of condensation [81]. In [81] the onset of nearly constant transmission was found to correspond to the dimensionless parameter $\Gamma^* \sim 400$. This parameter refers to the formalism of condensation of clusters described in section 2.2.2. From Γ^* the relevant stagnation pressure can be calculated, from which on the transmission stays nearly constant. With $p_0 = \Gamma^* \cdot T^{2.2875}/K \cdot d_{eq}^{0.85}$ and the parameters given in Table A.1 the relevant stagnation pressure becomes $p_{0,xe} = 276$ mbar for xenon.

The transmission trough the skimmer at this stagnation pressure is calculated by

$$T_{xe} = 1.38 \cdot e^{-0.32\left(\frac{2R_s}{\lambda_{xe}}\right)} \tag{A.2}$$

where R_s is the radius of the skimmer aperture, $\lambda_{xe} = (5.98 n_s)^{-1} \left(\frac{kT}{C_6}\right)^{1/3}$ is the mean free pathlength at the position of the skimmer and n_s is the density of atoms at the skimmer position. With the values given in Table A.1 the maximum skimmer transmission of Xe clusters becomes $T_{xe} = 0.156$. As a result the maximum number of atoms in the cylindrical focal volume is $N = N_f \cdot 0.156 = 9 \times 10^6$.

The kinetic energy of ions due to a Coulomb repulsion by the charge cloud in the focal volume is estimated with a simple electrostatic model of a homogeneously charged cylinder. The electric potential U of a charged cylinder is twofold. For distances r smaller (or equal) than the radius a of the cylinder the potential U is:

$$U = -q\frac{\rho}{4\epsilon_0}r^2 \quad r < a \tag{A.3}$$

For distances $r > a$ U becomes

$$U = -q\frac{\rho a^2}{2\epsilon_0}\ln\frac{r}{a} \quad r > a \tag{A.4}$$

where ρ is the charge density in the cylinder and $q = -ze$ is the charge of the ion with charge state z. The maximum kinetic energy E_{max} an ion can gain corresponds to a starting point (nearly) on the central axis of the cylinder. The ion gains energy while travelling through the charge cloud after equation (A.3) and once it has exited the charged cylinder it gains further energy due to equation (A.4). The maximum kinetic energy as a function of the distance r to the centre axis then becomes:

$$E_{max}(z,r) = -ze\left(\frac{\rho a^2}{2\epsilon_0}\ln\frac{r}{a} + \frac{\rho}{4\epsilon_0}a^2\right) \quad r > a \tag{A.5}$$

To calculate the *average* kinetic energy $\bar{E}$ it is taken into account, that each time an ion leaves the charge cloud the charge density $\rho = Q/V$ is reduced, where $Q = -\bar{z}eN$ is the total charge for the respective number of N ions in the space charge volume V and $\bar{z}$ is the average ion charge state.

$$\bar{E}(z,r) = \frac{-zea^2}{2\epsilon_0} \left(\ln \frac{r}{a} + \frac{1}{2} \right) \frac{-\bar{z}e}{V} \cdot \frac{\sum_{i=1}^{N} i}{N} \quad r > a \tag{A.6}$$

In Figure A.1 the average kinetic energy $\bar{E}(z,r)$ is given for eight different individual ion charge states $z = 1 - 8$ (given next to each trace) as a function of the distance r to the centre axis of the space charge volume. Because the space charge volume extends over the focal spot area, it can be expected that the power density of the FEL is strongly reduced in the peripheries and the average ion charge state is estimated to be $\bar{z} = 1$. In Figure A.1 the average energy is given beginning at a distance of $10\,\mu$m,
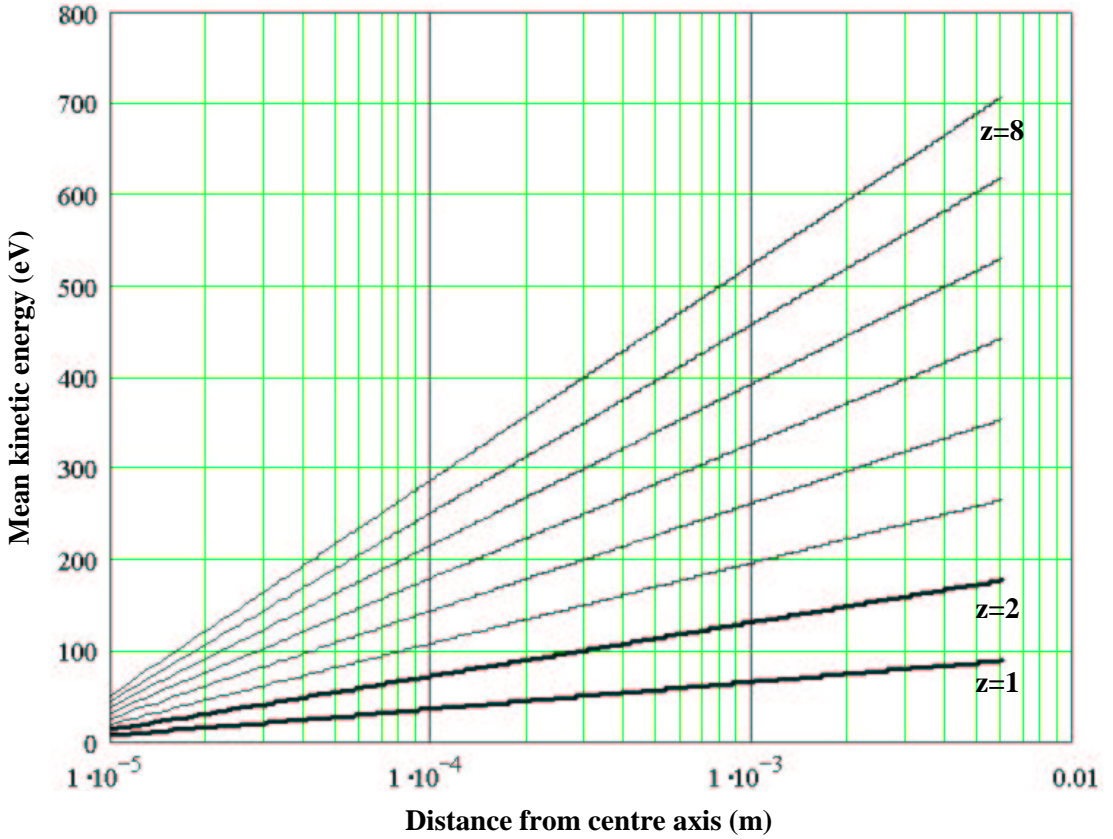
Figure A.1: Average kinetic energy of ions due to Coulomb repulsion of a space charge volume calculated in a simple electrostatic model. The individual ion charge states are given next to each trace. The average charge state of ions in the space charge volume is $\bar{z} = 1$. Details see text.

which is the radius a of the space charge volume. At a distance of 6 mm, which is

p_0	stagnation pressure	$4.3\,\mathrm{bar}$
T	gas temperature	$293\,\mathrm{K}$
d_{eq}	equivalent nozzle diameter	$268\,\mu\mathrm{m}$
x_f	distance nozzle-focus	$80\,\mathrm{mm}$
a	space charge: radius	$10\,\mu\mathrm{m}$
l	space charge: length	$1\,\mathrm{mm}$
K	condensation parameter	5554
R_s	skimmer radius	$0.5\,\mathrm{mm}$
C_6	van der Waals constant	$5.094{\times}10^{-77}\,\mathrm{Jm}^6$
n_s	density at skimmer	$n_s = \frac{p_0}{kT}\left(\frac{0.802\frac{d_{eq}}{2}}{z}\right) = 3.2 \times 10^{21}\,\mathrm{atoms/m}^3$
z	nozzle-skimmer distance	$5\,\mathrm{mm}$

Table A.1: Parameters for calculation of space charge influence.

the distance of the ion entrance aperture of the TOF mass spectrometer to the centre axis of the space charge volume, the average kinetic energy for a singly charged ion is about $90\,\mathrm{eV}$ and the results for higher charge states scale proportionally with z. The experimentally observed value for Xe^+ resulting from ionisation of Xe_{2500} clusters is $\sim 93\,\mathrm{eV}$, see Table 3.3. This means, that the influence of space charge can be quite strong.

The intention of the electrostatic space charge model was to estimate the influence of space charge on ion kinetic energies, resulting from the ionisation of the cluster gas in an extended interaction volume. Its results describe the maximum average kinetic energies due to space charge. On the other hand, the model certainly overestimates the influence of space charge for several reasons:

- The average energy is calculated for ions starting nearly at the centre of the space charge volume. This neglects that ions start distributed over the whole space charge volume.

- The total charge Q in the space charge volume depends heavily on the skimmer transmission. The value used for the skimmer transmission is the uppermost limit.

- In detail the dynamic properties of a charge cloud consisting of highly charged disassembling clusters are very complicated. Therefore modelling of the influence was restricted to a static model. As a consequence the model neglects all dynamical properties such as the expansion of the space charge itself.

It can be therefore concluded, that the simple electrostatic model overestimates the influence of space charge on ions, but its results show that the effect of space charge is not negligible. However, the ionisation of xenon and argon clusters show very similar results [75], although the skimmer transmission of argon is reduced by a factor of about 30 compared with xenon and thus space charge is almost negligible in the case of argon. Furthermore, the kinetic energy of ions due to space charge depends linearly on the ion charge state, but Figure 3.10 in section 3.3.5 shows a clear quadratic dependence. Therefore it can be concluded, that space charge effects possibly have to be taken into account, but their contribution is not substantial.

Appendix B

Alignment and adjustment of the cluster ion TOF

In the following, measurements are described which describe the alignment and the adjustment of the cluster ion TOF spectrometer. In Figure B.1 TOF mass spectra resulting from the ionisation of nitrogen molecules (N_2) at different power densities of the FEL are given. In each of the two parts in Figure B.1 the power density decreases from the top to the bottom. The way in which the power density was reduced is different in the two sets of measurements.

In the left part of Figure B.1 all spectra are taken in the focal plane and the power density is varied because of decreasing radiation pulse energies. The stray-light intensity as a measure of the energy of the FEL radiation pulse is given in volts next to each trace on the left. Thus, the power density is reduced because the number of photons delivered by the FEL decreases. The spot size remains the same and therefore also the interaction area.

In the right part of Figure B.1 the radiation pulse energy is the same for all TOF spectra but the interaction area is enlarged by moving it out of the focal plane.[1] The distance to the focal plane is given in mm next to each trace. Thus the power density is reduced by increasing the radiation spot size, but the number of photons remains unchanged.

In both parts various ion charge states of N_2 molecules or N atoms are visible. In the context of an alignment test the signal from N_2^+ is especially interesting, because N_2^+ is produced with zero kinetic energy.

It is remarkable, that in the left part of Figure B.1 at low pulse energy no N_2^+ is detected. On the other hand, reducing the power density by moving out of the focal plane, as in the right part, N_2^+ was detected at a distance of 1 mm to the focal plane

---

[1]The optical path of the focused radiation resembles the outline of an hourglass with the focal plane as the waist. Moving out of the focal plane thus increases the radiation spot size.

and steadily growing with increasing distance to the focal plane.

If one compares spectra with comparable N^+, N_2^{2+}-signal from both parts, the absence of N_2^+ in the focal plane might lead to the suggestion, that ions initially at rest are suppressed in the focal plane.

A possible explanation in this context would be, that the radiation spot in the focal plane is situated not directly underneath the ion entrance aperture, but is shifted slightly sideways. In this case ions at rest would be guided by the pull-in voltage onto the plate and not through the aperture. This would prevent their detection. But ions with a small kinetic energy and a velocity parallel to the entrance plate and into the direction of the aperture, would reach the aperture and could be detected. By moving out of the focal plane, the radiated area is enlarged and eventually 'overlaps' with the aperture. Thus, also ions at rest could enter the aperture. On the other hand, weak N_2^+-signal can be seen in the second uppermost trace of the left part of Figure B.1. This gives evidence, that ions at rest can be detected if the detector is in the focal plane, but possibly with a reduced sensitivity. In view of the complicated ionisation dynamics, no quantitative number for the transmission can be given.
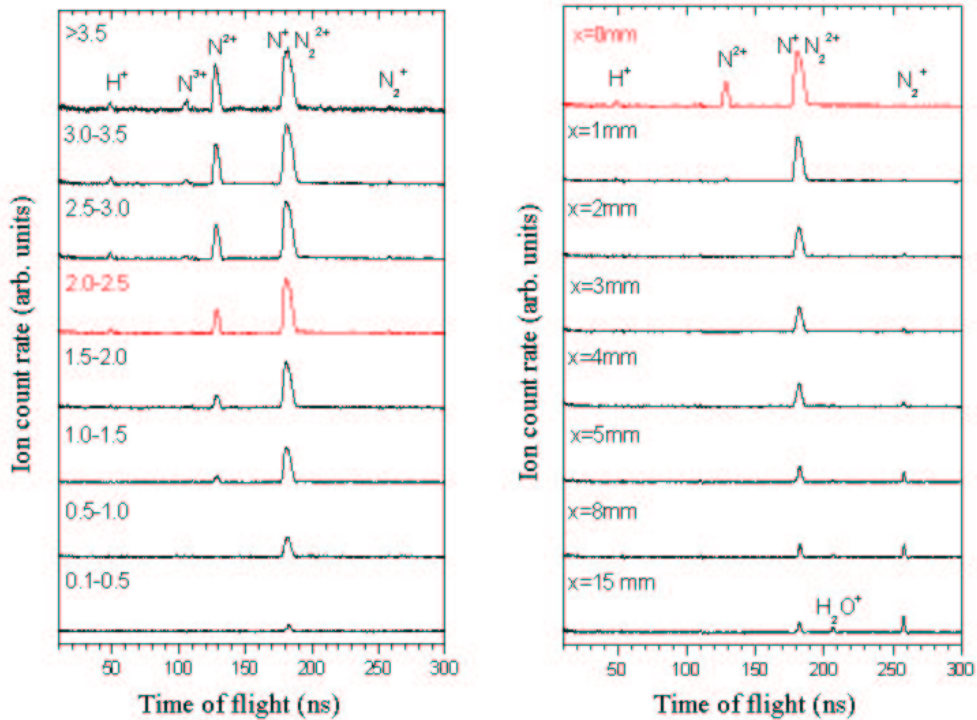
Figure B.1: TOF mass spectra after irradiation of nitrogen molecules. In both parts the corresponding power density decreases from the top to the bottom. In the left part mass spectra are taken in the focal plane and the power density decreases because of reduced radiation pulse energy. In the right part the power density decreases due to an increase of the radiation spot size. Details see text.

Appendix C

Random Ion Generator

```
 IMPLICIT REAL*8 (A-H,O-Z)
 CHARACTER*4  extension,YN
 CHARACTER*1 distrib,ABC
 CHARACTER*50  filename
 CHARACTER*50 fname_ext
 REAL*8 TOB(1000000),CHARGE(1000000),AZ(1000000)
& ,EL(1000000),KE(1000000),CWF(1000000),AZ1(1000000)
& ,EL1(1000000),opo,gasdev
 integer idum1,idum3,idum,idumx
 common /v1/ ske1,fwhm

 integer ii,i0,count(1800)
 real max

  do ii=1,1800
  count(ii)=0
  enddo

 idum=-2
 idum1=-5
 idumx=-1
 PI= 3.141592653589793238D0
  print *,'--------------------------------'
 print *, 'Random Ion Generator'
 print *,'--------------------------------'
 print *,' '
 print *,'* Use default settings ------> 1'
```

```
print *,'* Input variables -----------> 2'
print *,'* Change default settings ---> 3'
print *,' '
print *,'Choose option (1,2 or 3):'
READ *,iopt

if (iopt==2) then
print *,'-------------------------------'
print *,' '
print *,'* Input ion mass [in a.u.]:'
read *, TASS
print *,'* Input ion starting position [in g.u.]:'
print *,'X='
READ *, X
print *,'Y='
READ *, Y
print *,'Z='
READ *, Z
print *,'* Input ion charge state:'
READ *, ChargeS
print *,'* KE=const. ------------------> 1'
print *,'* Gaussian distribution -------> 2'
print *,' '
print *,'Select KE distribution [1 or 2]: '
read *,kedis
if (kedis==1) then
 print *,'* Input ion kinetic energy [in eV]:'
 READ *, SKE
 distrib='c'
endif
if (kedis==2) then
 print *,'* Input mean value [in eV]:'
 READ *, SKE
 print *,'* Input FWHM :'
 read *,FWHM
 distrib='g'
 ske1=ske
endif
print *,'* Input overall number of ions:'
read *,NK
print *,'* Input forward critical angle [in deg]:'
```

```fortran
read *,canglef
print *,'* Input backward critical angle [in deg]:'
read *,cangleb
endif
if (iopt==3) then
 print *,'-------------------------------'
print *,' '
print *,'* Input ion mass [in a.u.]:'
read *, TASS
print *,'* Input ion starting position [in g.u.]:'
print *,'X='
READ *, X
print *,'Y='
READ *, Y
print *,'Z='
READ *, Z
print *,'* Input ion charge state:'
READ *, ChargeS
print *,'* KE=const. ------------------> 1'
print *,'* Gaussian distribution -------> 2'
print *,' '
print *,'Select KE distribution [1 or 2]: '
read *,kedis
if (kedis==1) then
 print *,'* Input ion kinetic energy [in eV]:'
 READ *, SKE
 distrib='c'
 fwhm=0
endif
if (kedis==2) then
 print *,'* Input mean value [in eV]:'
 READ *, SKE
 print *,'* Input FWHM :'
 read *,FWHM
 distrib='g'
 ske1=ske
endif
print *,'* Input overall number of ions:'
read *,NK
print *,'* Input forward critical angle [in deg]:'
read *,canglef
```

```
print *,'* Input backward critical angle [in deg]:'
read *,cangleb
print *,'* Save default settings (Y/N)?'
read *,YN

if ((YN=='y').OR.(YN=='Y')) then
open(62,FILE='settings.dat',ACCESS='SEQUENTIAL')
write(62,*) TASS,X,Y,Z,Charges,distrib,SKE,FWHM,NK,canglef,cangleb
close(62)
print *,'... Settings saved'
endif
endif




if (iopt==1) then
open(62,FILE='settings.dat',ACCESS='SEQUENTIAL')
read(62,*) TASS,X,Y,Z,Charges,distrib,SKe,fwhm,NK
& ,canglef,cangleb
ske1=ske
print *,'... Settings loaded'
print *,' '
close(62)
endif
print *,'--------------------------------'
print *,' '
print *,'Specify output file name [<name.ion>]:'
read *,filename

print *,' '

print *,'... Working '

print *,' '



AZ(1)=0
EL(1)=-90
KE(1)=0
CWF(1)=1
KE(2)=3
```

```
        CWF(2)=4
        COLOR=0
        delAZ=canglef
        delEL=canglef
        delAZb=cangleb
        delELb=cangleb

        l=0

        EL(1)=0
        AZ(1)=0
        do i=1,NK

          EL(2)=180*ran2(idum)-90



          do ii= -900,899



          if(el(2).gt.(0.1*ii).and.el(2).le.(0.1*ii+1))then
          i0=ii+901
          goto 111
          endif
          enddo

111       continue



          max = NK/1800. * cos( pi/180.* (ii*0.1 - 0.05) )

          if (count(i0).le.max)then  !           Anfang Sortierung
          count(i0)=count(i0)+1



          AZ(2)=360*ran2(idum)-180

        if (distrib=='g') then
          ske=gasdev(idumx)
```

```fortran
   endif

   if (((AZ(2).LT.delAZ).AND.(AZ(2).GT.-delAZ)
&    .AND.(EL(2).LT.delEL).AND.(EL(2).GT.-delEL))
&    .OR.(((AZ(2).GT.(180-delAZb))
&    .OR.(AZ(2).LT.(-180+delAZb))).AND.
&    (EL(2).LT.delELb).AND.(EL(2).GT.-delELb))) then
       l=l+1
       AZ1(l)=AZ(2)
       EL1(l)=EL(2)
        KE(l)=ske
    CWF(l)=1
    TOB(l)=0
    CHARGE(l)=charges
     endif
    El(1)=EL(2)
    AZ(1)=AZ(2)

    endif  !  Ende Sortierung
   enddo
   nk=l

   print *,'OK ... ',l,' ions stored in ',filename

   fname_ext=filename
   OPEN (32,FILE=fname_ext,ACCESS='SEQUENTIAL')
   DO I=1,NK
   WRITE(32,'(A,I10)') ';',I
   WRITE(32,'(11(F12.6,A1))')TOB(I),',',TASS,',',CHARGE(I),',',X,','
&  ,Y,',',Z,',',AZ1(I),',',EL1(I),',',KE(I),',',CWF(I),',',COLOR,','
   ENDDO
   CLOSE(32)
   read *,ABC



   END

C  **********************************************************

   FUNCTION ran2(idum)
```

```fortran
      INTEGER idum,IM1,IM2,IMM1,IA1,IA2,IQ1,IQ2,IR1,IR2,NTAB,NDIV
      real*8 ran2,AM,EPS,RNMAX
      PARAMETER (IM1=2147483563,IM2=2147483399,AM=1.D0/IM1,IMM1=IM1-1,
     *    IA1=40014,IA2=40692,IQ1=53668,IQ2=52774,IR1=12211,
     *    IR2=3791,NTAB=32,NDIV=1+IMM1/NTAB,EPS=1.2D-7,RNmax=1.D0-EPS)
      INTEGER idum2,j,k,iv(NTAB),iy
      SAVE iv,iy,idum2
      DATA idum2/123456789/, iv/NTAB*0/, iy/0/

      if (idum.le.0) then
       idum=max(-idum,1)
       idum2=idum
       do j=NTAB+8,1,-1
        k=idum/IQ1
        idum=IA1*(idum-k*IQ1)-k*IR1
        if (idum.lt.0) idum=idum+IM1
        if (j.le.NTAB) iv(j)=idum
       enddo
       iy=iv(1)
      endif

      k=idum/IQ1
      idum=IA1*(idum-k*IQ1)-k*IR1
      if (idum.lt.0) idum=idum+IM1
      k=idum2/IQ2
      idum2=IA2*(idum2-k*IQ2)-k*IR2
      if (idum2.lt.0) idum2=idum2+IM2
      j=1+iy/NDIV
      iy=iv(j)-idum2
      iv(j)=idum
      if (iy.lt.1) iy=iy+IMM1
      ran2=min(AM*iy,RNMaX)

      return
      END

      FUNCTION ran0(idumx)
      INTEGER idumx,IA,IM,IQ,IR,MASK
      REAL*8 ran0,AM
      PARAMETER (IA=16807, IM=2147483647,AM=1.D0/IM,
     *  IQ=127773, IR=2836, MASK=123459867)
```

```
      INTEGER k
      idumx=ieor(idumx,MASK)
      k=idumx/IQ
      idumx=IA*(idumx-k*IQ)-IR*k
      if (idumx.lt.0) idumx=idumx+IM
      ran0=AM*idumx
      idumx=ieor(idumx,MASK)
      return
      END


      function gasdev(idumx)
       IMPLICIT REAL*8 (A-H,O-Z)
      INTEGER idumx
      INTEGER iset
      common /v1/ ske1,fwhm
      REAL*8 fac,rsq,x1,x2,yc,ran0,gset,si,PI
      save iset,gset
      data iset/0/
      yc=ske1
      si=fwhm/2.355D0
      PI= 3.141592653589793238D0
      if (idumx.lt.0) iset=0
      if (iset.eq.0) then

 1    x1=2*ran0(idumx)-1
      x2=2*ran0(idumx)-1
      rsq=x1**2+x2**2
      if (rsq.ge.1..or.rsq.eq.0) goto 1
      fac=sqrt(-2.D0*log(rsq)/rsq)
      gset=yc+si*(x1*fac)
      gasdev=yc+(x2*fac)*si
      iset=1
      else
      gasdev=gset
      iset=0
      endif
      return
      END
```

Appendix D

Find Ions

```
Program findions

IMPLICIT REAL*8 (A-H,O-Z)
CHARACTER*50  filename,filename1,filename2,filename3,SA(12)
CHARACTER*50 fname_ext,ytyty
REAL*8 TOB(1000000,3),TOB1(1000000,3),rez(1000000,3)

NMAX=1000000

do i=1,NMAX
 do j=1,2
 TOB(i,j)=-1
 enddo
enddo
print *,'--------------------------------'
print *,'FIND_IONS'
print *,'--------------------------------'
print *,' '
print *,'* Specify input file name:'
read *, filename
print *,'* Specify original .ion file:'
read *, filename3
print *,'* Input position of the detector [in mm]:'
read *,posi
print *,' '
print *,'* Basic spectrum file ------------> 1'
print *,'* .ION file of detected ions ------> 2'
print *,'* 1+2 ---------------------------> 3'
```

```
print *,'* No output file -----------------> 4'


print *,' '
print *,'Select option [1,2,3 or 4]:'
read *,option
if ((option==1).or.(option==3)) then
 print *,' '
 print *,'Specify output file name for spectrum:'
 read *, filename1
endif

if ((option==2).or.(option==3)) then
 print *,' '
 print *,'Specify output file name for .ION file:'
 read *, filename2
endif

print *,' '
print *,' ... Working'


fname_ext=filename
OPEN (32,FILE=fname_ext,ACCESS='SEQUENTIAL')
read(32,'(A)')fname_ext
read(32,'((F9.0,F12.6,F12.6))',END=99)((TOB(i,j),j=1,3),i=1,NMAX)


99 j=0
   do i=1,NMAX
   if (TOB(i,1)/=-1) then
   j=j+1
   endif
   ENDDo

   close(32)


   num=0
   do i=1,j

   if ((TOB(i,3).Ge.posi-0.1).AND.(TOB(i,3).Le.posi+0.1)) then
```

```fortran
      num=num+1
      rez(num,1)=TOB(i,1)
      rez(num,2)=TOB(i,2)
      rez(num,3)=TOB(i,3)
      endif
      enddo

      print *,' '
      print *,num,' ions hit the detector'

      if ((option==1).OR.(option==3)) then
      open(33,FILE=filename1,ACCESS='SEQUENTIAL')
      write(33,'(F12.6)')((rez(i,2),l=1,1),i=1,num)
      close(33)
      endif


      fname_ext=filename3
      OPEN (32,FILE=fname_ext,ACCESS='SEQUENTIAL')
      if ((option==2).or.(option==3)) then
      OPEN (33,FILE=filename2,ACCESS='SEQUENTIAL')
      endif
      ELmax=0
      AZmax=0
      ELmax1=0
      AZmax1=180

      ELmin=0

       ij=0
       ij1=0
      DO I=1,NMAX
      READ(32,'(A,F10.0)',END=88) SA(1),PE
      READ(32,'(11(F12.6,A1))') TOB0,SA(1),TASS,SA(2)
     & ,CHARGE,SA(3),X,SA(4)
     & ,Y,SA(5),Z,SA(6),AZ,SA(7),EL,SA(8),KE,SA(9),CWF
     & ,SA(10),COLOR,SA(11)
```

```
      TOBO=0.d0
      do ii=1,num
      IF (i==rez(ii,1)) then
      if ((ELmax.LT.EL).AND.(AZ.LT.90.d0)) then
      ELmax=EL
      endif

      if ((ELmin.GT.EL).AND.(AZ.LT.90.d0)) then
      ELmin=EL
      endif

      if ((AZmax.LT.AZ).AND.(AZ.LT.90.d0)) then
      AZmax=AZ
      endif

      if ((AZmax1.GT.AZ).AND.(AZ.GT.90.d0).AND.(AZ.GT.0)) then
      AZmax1=AZ
      endif
     if ((ELmax1.LT.EL).AND.(AZ.GT.90.d0)) then
      ELmax1=EL
      endif
        if ((AZ.1T.90).AND.(AZ.GT.-90)) then
       ij=ij+1
       endif
       if ((option==2).or.(option==3)) then
       ij1=ij1+1
       write(33,'(A,I10)') ';',ij1
       write(33,'(11(F12.6,A1))')TOBO,',',TASS,',',CHARGE,',',X,','
    & ,Y,',',Z,',',AZ,',',EL,',',KE,',',CWF,',',COLOR,' '
       endif
      endif
       enddo
     ENDDO
 88  CLOSE(32)
     CLOSE(33)

     print *,' '
     print *,ij,' forward and ',num-ij,' backward ions'
     read *,ytyty

     end
```

List of Figures

List of Tables

Bibliography

[1] M. Göppert-Mayer. Über Elementarakte mit zwei Quantensprüngen. *Ann. d. Phys.*, 9:273–294, 1931.

[2] T.H. Mainmann. Stimulated optical radiation in ruby. *Nature*, 187:493, 1960.

[3] W. Kaiser and C.G.B. Garret. Two-photon excitation in CaF_2:Eu. *Phys. Rev. Lett.*, 7:229–231, 1961.

[4] V. Ayvazyan et al. Generation of GW radiation pulses from a VUV free-electron laseroperating in the femtosecond regime. *PRL*, 88:10482, 2002.

[5] V. Ayvazyan et al. A new powerful source for coherent VUV radiation: Demonstration of experimental growth and saturation at the TTF free-electron laser. *Eur. Phys. J. D*, 20:149–156, 2002.

[6] H. Merdji. High harmonics generation and applications to plasma physics. Research courses on nex X-ray sciences: Plasma physics with X-rays, held at DESY Hamburg, march 2003.

[7] G. Materlik and Th. Tschentscher, editors. *Tesla Technical Design Report Part V: The X-ray free electron laser*, 2001.

[8] K. Wille. The physics of particle accelerators. *Oxford University Press*, page 233ff., 2000.

[9] E.L. Saldin, E.A. Schneidmiller, and M.V. Yurkov. *The physics of free-electron lasers*. Springer-Verlag Berlin Heidelber New York, 2000.

[10] K. Tiedtke. private communications.

[11] B. Faatz et al. Use of a micro-channel plate for nondestructive measurement of VUV radiation from the SASE FEL at the TESLA Test Facility. *DESY Print TESLA-FEL 2001-09*, pages 62–67, 2001.

[12] R. Bonifacio, L. De Salvo, P. Pierini, N. Piovella, and C. Pellegrini. Spectrum, temporal structure and in a high-gain free-electron laser starting from noise. *Phys. Rev. Lett.*, 73:70, 1994.

[13] E.L. Saldin, E.A. Schneidmiller, and M.V. Yurkov. Statistical properties of radiation from VUV and X-ray free electron laser. *Opt. Commun.*, 148:383–403, 1998.

[14] V. Ayvazyan et al. Study of the statistical properties of the radiation from a VUV SASE FEL operating in the femtosecond regime. *to be published in Nucl. Instrum. and Meth. A*, 2003.

[15] R. Ischebek. *Measurement of the transverse coherence at the TTF free-electron laser.* PhD thesis, University of Hamburg, 2003.

[16] D. Attwood. *Soft X-rays and extreme ultraviolet radiation: Principles and applications.* Cambridge University Press, 1999.

[17] E.L. Saldin. private communications.

[18] J. Stapelfeldt. *CLULU: Ein neues Experiment fr Fluoreszenzuntersuchungen an Edelgas-Clustern vom Dimer bis zum Mikrokristall.* PhD thesis, Universität Hamburg, 1990.

[19] F. Federmann. Innerschalenspektroskopie an freien Argon- und Neonclustern. *Phd-thesis, University of Hamburg*, 1994.

[20] G. Scoles, editor. *Atomic and molecular beam methods 1.* Oxford University Press, 1988.

[21] O.F. Hagena and W. Obert. Cluster formation in expanding supersonic jets: Effect of pressure, temperature, nozzle size and test gas. *Journal of Chemical Physics*, 56:1793–1802, 1972.

[22] O.F. Hagena. Nucleation and growth of clusters in expanding nozzle flows. *Surface Science*, 106:101–116, 1981.

[23] U. Buck and R. Krohne. Cluster size determination from diffractive He atom scattering. *J. Chem. Phys.*, 105:5408–5415, 1996.

[24] Hamamatsu, http://www.hamamatsu.de/. *MCP assembly F4655-13.*

[25] Idaho National Engineering and Environmental Laboratory, Idaho Falls, ID 83415. *SIMION 7.0*, 2000.

[26] J.L. Wiza. Microchannel plate detectors. *Nucl. Instr. and Meth.*, 162:587–601, 1979.

[27] G.W. Fraser. The ion detection efficiency of microchannel plates (MCPs). *Int. J. Mass. Spect.*, 215:13–30, 2002.

[28] J. Oberheide, P. Wilhelms, and M. Zimmer. New results on the absolute ion detection efficciencies of a microchannel plate. *Meas. Sci. Technol*, 8:351–354, 1997.

[29] M.Tassotto and P.R. Watson. Detection efficiency of a channel electron multiplier for low energy incident noble gas ions. *Rev. Sci. Instrum.*, 71:2704–2709, 2000.

[30] Galileo Corporation, http://www.burle.com/cgi-bin/byteserver.pl/pdf/TP201.pdf. *Bi-polar time-of-flight detector*.

[31] WATEC. *Black and white CCD-camera WAT-902*.

[32] W.C. Wiley and I.H. McLaren. Time-of-flight mass spectrometer with improved resolution. *Rev. Sci. Instr.*, 26:1150, 1955.

[33] J.L. Chaloupka, J. Rudati, R. Lafon, P. Agostini, K.C. Kulander, and L.F. Di-Mauro. Observation of a transition in the dynamics of strong-field double ionization. *Phys. Rev. Lett.*, 90:033002–1, 2003.

[34] M. Hentschel et al. Attosecond metrology. *Nature*, 414:509–513, 2001.

[35] M. Drescher et al. Time-resolved atomic inner-shell spectroscopy. *Nature*, 419:803–807, 2002.

[36] J.F. Hergott et al. Extreme-ultraviolet high-order harmonic pulses in the micro-joule range. *Phys. Rev. A*, 66:021801(R), 2002.

[37] N.B. Delone and V.P. Krainov. *Multiphoton processes in atoms*. Springer, 2000.

[38] L.V. Keldysh. Ionization in the field of a strong electromagnetic wave. *JETP*, 20:1307–1314, 1965.

[39] M. Protopapas, C.H. Keitel, and P.H. Knight. Atomic physics with super-high intensity lasers. *Rep. Prog. Phys.*, 60:389–486, 1997.

[40] P. Lambropoulos and X. Tang. Multiple excitation and ionization of atoms by strong lasers. *J. Opt. Soc. Am. B.*, 4:821–832, 1987.

[41] M. Richter, G. Ulm, Chr. Gerth, K. Tiedtke, J. Feldhaus, A.A. Sorokin, L.A. Shmaenok, and S.V. Bobashev. Photoionization cross sections of Kr and Xe from threshold up to 1000 eV. *in preparation*, 2003.

[42] E.A. Schneidmiller. private communications.

[43] T.S. Luk, H. Pummer, K. Boyer, M. Shahidi, H. Egger, and C.K. Rhodes. Anomalous collision-free multiple ionization of atoms with intense picosecond ultraviolet radiation. *Phys. Rev. Lett.*, 51:110–113, 1983.

[44] A. Saenz and P. Lambropoulos. Theoretical two-, three- and four-photon ionization cross sections of helium in the XUV range. *J. Phys. B.*, 32:5629–5637, 1999.

[45] E.W. Becker, K. Bier, and W. Henkes. Strahlen aus kondensierten Atomen und Molekeln im Hochvakuum. *Z. Phys.*, 146:333, 1956.

[46] T. Laarmann, A. Kanaev, K. von Haeften, H. Wabnitz, R. Pietrowski, and T. Möller. Evolution of the charge localization process in xenon cluster ions: From tetramer to dimer cores as a function of cluster size. *J. Chem. Phys.*, 116:7558–7563, 2002.

[47] D. Strickland and G. Mourou. Compression of amplified chirped optical pulses. *Opt. Commun.*, 56:219, 1985.

[48] J. Purnell, E. M. Snyder, S. Wei, and Jr. A. W. Castleman. Ultrafast laser-induced Coulomb explosion of clusters with high charge states. *Chem. Phys. Lett.*, 229:333–339, 1994.

[49] T. Ditmire, T. Donelly, A.M. Rubenchik, R.W. Falcone, and M.D. Perry. Interaction of intense laser pulses with atomic clusters. *Phys. Rev. A*, 53:3379–3402, 1996.

[50] T. Ditmire et al. High-energy ions produced in explosions of superheated atomic clusters. *Nature*, 386:54–56, 1997.

[51] T. Ditmire, R.A. Smith, J.W.G Tisch, and M.H.R. Hutchinson. High intensity laser absorption by gases of atomic clusters. *Phys. Rev. Lett.*, 78:3121–3124, 1997.

[52] A. McPherson, B. Thompson, A.B. Borisov, K. Boyer, and C.K. Rhodes. Multiphoton-induced X-ray emission at 4-5 keV from Xe atoms with multiple core vacancies. *Nature*, 370:631–634, 1994.

[53] T. Ditmire, R.A. Smith, R.S. Marjoribanks, G. Kulcsar, and M.H.R. Hutchinson. X-ray yields from Xe clusters heated by short pulse high intensity lasers. *Appl. Phys. Lett.*, 71:166–168, 1997.

[54] T. Ditmire, J. Zweiback, V.P. Yanovsky, T.E. Cowan, G. Hays, and K.B. Wharton. Nuclear fusion from explosions of femto-second laser-heated deuterium clusters. *Nature*, 398:489–492, 1999.

[55] M. Lezius, S. Dobosz, D. Normand, and M. Schmidt. Explosion dynamics of rare gas clusters in strong laser fields. *Phys. Rev. Lett.*, 80:261–264, 1997.

[56] K. Ishikawa and T. Blenski. Explosion dynamics of rare gas clusters in an intense laser field. *Phys. Rev. A*, 62(063204), 2000.

[57] T. Fennel. private communications.

[58] C. Rose-Petruck, K.J. Schafer, K.R. Wilson, and C.P.J. Barty. Ultrafast electron dynamics and innershell ionization in laser driven clusters. *Phys. Rev. A*, 55:1182–1190, 1997.

[59] I. Last and J. Jortner. Quasiresonance ionization of large multicharged clusters in a strong laser field. *Phys. Rev. A*, 60:2215–2221, 1999.

[60] I. Last and J. Jortner. Dynamics of the Coulomb explosion of large clusters in a strong laser field. *Phys. Rev. A*, 62, 2000.

[61] M. Brewczyk et al. Stepwise explosion of atomic clusters induced by a strong laser field. *Phys. Rev. Lett.*, 80:1857–1860, 1998.

[62] V.P. Krainov and A.S. Roshupkin. Dynamics of Coulomb explosion of large clusters irradiated by a super-intense ultra-short laser pulse. *J. Phys. B*, 32:297–303, 2001.

[63] V.P. Krainov and M.B. Smirnov. Cluster beams in the super-intense femtosecond laser pulse. *Physics reports*, 370:237–331, 2002.

[64] C. Siedschlag and J.M. Rost. Enhanced ionization in small rare-gas clusters. *Phys. Rev. A*, 67:013404, 2003.

[65] T. Zuo and A. Bandrauk. Charge-resonance-enhanced of diatomic molecular ions by intense lasers. *Phys. Rev. A*, 52:R2511–R2514, 1995.

[66] T. Seideman, M. Yvanov, and P. Corkum. Role of electron localization in intense-field molecular ionization. *Phys. Rev. Lett.*, 75:2819–2822, 1995.

[67] M. Brewczyk and K. Rzazewski. Over-the-barrier ionization of multi-electron atoms by intense VUV free-electron-laser. *J. Phys. B*, 32:L1–L3, 1999.

[68] J. Schulz, H. Wabnitz, T. Laarmann, P. Gürtler, W. Laasch, A. Swiderski, T. Möller, and A.R.B. de Castro. Energy absorption of free rare gas clusters irradiated by intense VUV pulses of a free electron laser. *Nucl. Instrum. Methods Phys. Res. Sect. A*, accepted for publication, 2003.

[69] V.P. Silin. *JETP*, 20:1510, 1965.

[70] W.L. Kruer. *The physics of laser plasma interactions*. Addison-Wesley Publishing Company, 1988.

[71] S. Pollack, C.R.C. Wang, and M.M. Kappes. On the optical response of Na_{20} and its relation to computational prediction. *J. Chem. Phys.*, 94:2496–2501, 1991.

[72] H. Hövel, S. Fritz, A. Hilger, U. Kreibig, and M. Vollmer. Width of cluster plasmon resonances: Bulk dieletric functions and chemical interface damping. *Phys. Rev. B*, 48:18178–18188, 1993.

[73] G. Bader, G. Perluzzo, L.G. Caron, and L. Sanche. In *Tenth Molecular Crystal Symposium, Quebec, Canada*, page 14, 1982.

[74] N. Schwentner, E.E. Koch, and J.Jortner. *Electronic excitations in condensed rare gases*, volume 107 of *Springer tracts in modern physics*. Springer Verlag Berlin Heidelberg New York Tokyo, 1985.

[75] T. Laarmann, H. Wabnitz, J. Schulz, A.R.B. de Castro, P. Gürtler, W. Laasch, A. Swiderski, and T. Möller. Interaction of argon clusters with soft X-rays from a free-electron laser: The role of the electronic structure in the energy absorption process. *in preparation*, 2003.

[76] I.Y. Kostyukov. Inverse-bremsstrahlung absorption of an intense laser field in cluster plasma. *JETP Lett.*, 73:393–397, 2001.

[77] A. Brantov, W. Rozmus, R. Sydora, C.E. Capjack, V. Yu. Bychenkov, and V.T. Tikhonchuk. Enhanced inverse bremsstrahlung heating rates in a strong laser field. *submitted to Plasm. Phys.*, 2003.

[78] Y.L. Shao, T. Ditmire, J.W.G. Tisch, E. Springate, J.P. Marangos, and M.H.R. Hutchinson. Multi-keV electron generation in the interaction of intense laser pulses with Xe clusters. *Phys. Rev. Lett.*, 77:3343–3346, 1996.

[79] F. Fössing. Innerschalen Photoelektronenspektroskopie an freien Clustern. Diplomarbeit,Universität Hamburg, 1994.

[80] U. Saalmann and J.M. Rost. Ionization of clusters in strong X-ray laser pulses. *Phys. Rev. Lett.*, 89:143401, 2002.

[81] Beijerinck et al. Campargue-type supersonic beam sources: Absolute intensities, skimmer transmission and scaling laws for mono-atomic gases He, Ne and Ar. *Chem. Phys.*, 96:153–173, 1985.

Danksagung

Ich habe während meiner Zeit als Doktorand viel freundliche Unterstützung erfahren und dafür möchte ich mich bedanken.

Am offensichtlichsten hat zweifellos Thomas Möller zu dem Gelingen dieser Arbeit beigetragen. Er hat mir diese Arbeit ermöglicht und seine Begeisterung, sein Einsatz und seine Betreuung haben mich über die ganze Zeit hinweg unterstützt. Genau diese Begeisterung und Hilfsbereitschaft ist auch Tim Laarmann und Joachim Schulz zueigen. Ich kann mich glücklich schätzen, mit diesen dreien zusammengearbeitet zu haben.

Am Aufbau und Betrieb des Clusterexperiments haben zusätzlich Anja Swiderski und Ralph Döhrmann, Wiebke Laasch und Peter Gürtler, Klaus von Haeften und Antonio Rubens Britto de Castro mitgewirkt und zu dem Erfolg des Experiments haben alle entscheidend beigetragen.

Meinen besonderen Dank spreche ich den Mitgliedern des TTF-Teams aus. Ich habe nur einen kleinen Einblick in die Unwägbarkeiten und Schwierigkeiten bekommen, die der Betrieb dieser neu- und bisher einzigartigen Lichtquelle mit sich brachte. Sie haben die Herausforderung gemeistert und damit meine Experimente möglich gemacht.

Die ganze Zeit über verband mich enge Zusammenarbeit und ständige Diskussion mit den Mitgliedern der Photonen-Diagnostik am HASYLAB. In Gesprächen mit Barbara Steeg, Elke Plönjes, Christopher Geert, Rolf Treusch, Josef Feldhaus und Kai Tiedtke haben sich viele neue Ideen und Verbesserungen ergeben.

Darüberhinaus hat mir Kai mit einer Fülle willkommener Anregungen und Bemerkungen zu dieser Arbeit weiter geholfen.

Bei Vladimir Jovanovic möchte ich mich für die Programmierung von zwei wichtigen Auswerteprogrammen bedanken.

Viele haben zu einer angenehmen Arbeitsatmosphäre beigetragen. Zusätzlich zu den bereits genannten waren dies innerhalb der Cluster-Arbeitsgruppe Manfred Riedler, Colm McGinley, Sorin Adam und Arun Lobo.

Besonders hat mir Colm mit der sprachlichen Korrektur meiner Arbeit und seiner unnachahmlich erfrischenden Art unter die Arme gegriffen.

Abgesehen von allem anderen danke ich Markus für seine Freundschaft.

Meine Eltern Hannelore und Rudolf und meinen Geschwistern Sabine und Michael gebührt der innigste Dank.